

**Novel Devices Employing Epitaxial Wide Bandgap
Semiconductors: Physics, Electronics and
Materials Characterization**

Thesis by

Zvonimir Z. Bandić

In Partial Fulfillment of the Requirements
for the Degree of
Doctor of Philosophy

California Institute of Technology
Pasadena, California

2000

(Submitted May 26, 1999)

© 2000

Zvonimir Z. Bandić

All Rights Reserved

To my wife Snežana, for all her love and support.

Acknowledgements

I spent considerable time thinking how to express and acknowledge help and encouragement I received from many people and institutions throughout my life, which brought me to the finale of my academic pursuit. I believe I was blessed by God who placed all these people close to me to advise me and guide me to the right direction.

I will forever be grateful for the five years I spent at Caltech, and especially for being member of the McGill group. Professor Tom carefully crafted a unique environment, where academic and scientific freedom and amount of associated financial support are probably unmatched anywhere in the academic and industrial research world. He leads the group with his incredible instinct for uncovering exciting research direction, vast knowledge of physics, and amazing capacity to learn new science just by getting to the close proximity of the book describing the subject. It would be unfair to Prof. Tom not to mention his important influence on me in many other ways beside Applied Physics. Prof. Tom's understanding of different cultures and different worlds is amazing, and I am sure it takes a great physicist, great mind and great traveler to do such a thing. I am proud to say that his advice and guidance made me a better colleague and better man.

Prof. Tom has brought a great number of senior researchers together for the benefit of the students and group activities. I should especially acknowledge continuous help and support from Prof. Jim McCaldin, in almost all the topics in this thesis. His involvement was especially notable in the ZnS thin film recrystallization project, where his guidance was crucial. I have also learned a lot from Ogden Marsh, Gerry Picus, and David Ting. The GaN projects benefited a lot from cooperation with Prof. Tom Kuech from University of Wisconsin and Joan Redwing from ATMI Epitronics who generously supplied GaN samples. I must say that it took only one afternoon of working on GaN piezoeffects proposal with Prof. Tom Kuech to learn a lot on how to be a good and useful team member, "a good soldier" as he put it.

Research would be much harder if I did not have a support provided by McGill's group administrative assistants. Marcia Hudson and Gloria Pendlay were great help. I am forever thankful to Tim Harris for his efficient dealings with journal correspondence, conference registrations, airline tickets and numerous discussions on Caltech's and US politics issues.

McGill's group seems to be an infinite source of great researchers and rich characters. Experimental experience is carefully transferred to junior students, and I am proud and lucky to be part of the chain. I am thankful to Johannes Swenberg who taught me how to luminescence experiments, Michael Wang who helped me start working on X-ray machine, and Erik Daniel who showed me the ways in and around Sputter-Etch system. My office-mate Per-Olov Pettersen and Chris Springfield also helped in many other ways. I am sure my career at Caltech would be much less interesting without Eric Piquette and Paul Bridger, who are certainly the smartest fellows I have ever met. I had many mutually fruitful and exciting discussions about many scientific topics with both of them, some of them related to Caltech's research, some not. We worked together on most of projects presented in this thesis, and two of them taught me a lot about experimental physics.

Caltech is a great place to do research and learn new things. I greatly benefited from my interactions with Prof. Kerry Vahala, Harry Atwater and Noel Corngold. Prof. William Johnson helped me a lot by explaining the origin of hexagonal pits in recrystallized ZnS films.

I am also thankful to Office of Naval Research, Defense Advanced Research Project Agency and Electric Power Research Institute for funding the projects described in this thesis. In particular, I would like to thank to contract monitors Larry Cooper, Jerry Melcher and John Zolper for their support and encouragements.

Before coming to Caltech and I had great luck and a privilege to get my education from the Yugoslav education system. It is not possible to explain in detail how much help I got over the years. At least I can say that I am thankful to: Prof. Srdjan Ognjanović, Prof. Bojana Nikić and Nataša Caluković from Mathematical High School in Belgrade, Vigor Majić and many other lecturers from Research Center

“Petnica” in Valjevo, and the late Prof. Mihailo Marković, Prof. Zoran Ikonić, Prof. Slavoljub Marjanović, Prof. Jovan Radunović and Prof. Srbijanka Turajlić from School of Electrical Engineering at the University of Belgrade.

My family also provided me with a lot of help and support, and it is again hard to thank everyone, simply because there were so many of them. I would not be sitting here writing acknowledgment section of my PhD thesis if it were not for my late grandfather Col. Dušan Janković. He had unbelievable patience and tutored me in a mathematics course from arithmetic to calculus in just a couple of years. He also tried to explain to me long ago that engineers and scientists (in all the excitement) were not aware that arms and weapons were used to kill people. My father Zvonimir I. and mother Dragana continuously supported me in any activity I was pursuing, from building time-travel machines, to playing violin and basketball, to studying mathematics, physics and electronics. They provided me with all the love, care and wisdom a child can wish for. I hope I will be capable of being like them one day. I will never forget discussions with my father and with my late uncle Prof. Miloš I. Bandić which helped me to grow from a boy to man. I am also thankful to my uncle Prof. Bogdan Beleslin and my aunt Prof. Jelisaveta Baranac who opened the doors of their labs and let me peek in, when I really needed to know what the lab was. I am thankful to my sister Ivana for all her love. I would have never made it without my family.

I am thankful to my bestmen Dragoslav Mitrinović and Ivan Eraković for their friendship. We started as fellow high-schoolboys and stayed friends for almost 15 years.

And above all, I am thankful to my wife Snezana, who helped me stay sane throughout the five years of my doctoral career, and who pointed out many times the beauties and challenges of the world outside the lab, which I frequently forgot. I am very much thankful for her patience while I was working late nights in the lab. For her love, support and everything she did for me and instead of me, I am and will be forever thankful.

Zvonimir Z. Bandić

List of Publications

Work related to this thesis has been or will be published under the following titles:

The values of minority carrier diffusion lengths and lifetimes and their implications for bipolar devices,

Z. Z. Bandić, P. M. Bridger, E. C. Piquette, and T. C. McGill, to be published in special issue of Solid State Electronics.

Design of GaN/AlGaN high power devices,

Z. Z. Bandić, E. C. Piquette, P. M. Bridger, and T. C. McGill, Electrochemical Society Proceedings **98**, 39 (1998).

Nitride based high power devices,

Z. Z. Bandić, E. C. Piquette, P. M. Bridger, R. A. Beach, and T. C. McGill, Solid State Electron. **42**, 2289 (1998).

High voltage (450 V) GaN Schottky rectifiers,

Z. Z. Bandić, P. M. Bridger, T. C. McGill, R.P. Vaudo, V.M. Phanse, and J.M. Redwing, Appl. Phys. Lett. **74**, 1266 (1999).

Electron diffusion length and lifetime in p-type GaN,

Z. Z. Bandić, P. M. Bridger, E. C. Piquette, and T. C. McGill, Appl. Phys. Lett. **73**, 3276 (1998).

Minority carrier diffusion length and lifetime in GaN,

Z. Z. Bandić, P. M. Bridger, E. C. Piquette, and T. C. McGill, Appl. Phys. Lett. **72**, 3166 (1998).

Correlation between the surface defect distribution and minority carrier transport properties in GaN,

P. M. Bridger, Z. Z. Bandić, E. C. Piquette, and T. C. McGill, Appl. Phys. Lett. **73**, 3438 (1998).

Design and Fabrication of Nitride Based High Power Devices,

Z. Z. Bandić, E. C. Piquette, P. M. Bridger, T. F. Kuech, and T. C. McGill, *Mat. Res. Soc. Symp. Proc.* **483**, 399 (1998).

Nitride Based High Power Devices: Transport Properties, Linear Defects and Goals,

Z. Z. Bandić, P. M. Bridger, E. C. Piquette, T. F. Kuech, and T. C. McGill, *Mat. Res. Soc. Symp. Proc.* **512**, 27 (1998).

Experimental study of sputter deposited contacts to Gallium Nitride,

E. C. Piquette, Z. Z. Bandić, and T. C. McGill, *Mat. Res. Soc. Symp. Proc.* **482**, 1089 (1998).

Growth of III-nitrides by RF-assisted molecular beam epitaxy,

E. C. Piquette, P. M. Bridger, Z. Z. Bandić, and T. C. McGill, *Mat. Res. Soc. Symp. Proc.* **512**, 387 (1998).

Solid phase recrystallization of ZnS thin films on sapphire,

Z. Z. Bandić, E. C. Piquette, J. O. McCaldin, and T. C. McGill, *Appl. Phys. Lett.* **72**, 2862 (1998).

MBE Growth and Characterization of ZnS/GaN Heterostructures,

E. C. Piquette, Z. Z. Bandić, J. O. McCaldin, and T. C. McGill, *Mat. Res. Soc. Symp. Proc.* **449**, 385 (1997).

Growth and Characterization of Light Emitting ZnS/GaN Heterostructures,

E. C. Piquette, Z. Z. Bandić, J. O. McCaldin, and T. C. McGill, *J. Vac. Sci. Technol. B* **15**, 1148 (1997).

Kinetic modeling of microscopic processes during electron cyclotron resonance microwave plasma assisted molecular beam epitaxial growth of GaN/GaAs based heterostructures,

Z. Z. Bandić, R. J. Hauenstein, M.L. O'Steen, and T. C. McGill, *Appl. Phys. Lett.* **68**, 1510 (1996).

Microscopic processes during electron cyclotron resonance microwave nitrogen plasma assisted molecular beam epitaxial growth of GaN/GaNAs heterostructures: experiments and kinetic modeling,

Z. Z. Bandić, R. J. Hauenstein, M.L. O'Steen, and T. C. McGill, *J. Vac. Sci. Technol.* **14**, 2948 (1996).

Kinetics of nitrogen in GaAsN layers during GaAs overgrowth,

Z. Z. Bandić, R. J. Hauenstein, M.L. O'Steen, and T. C. McGill, *Mat. Res. Soc. Symp. Proc.* **449**, 209 (1997).

Anion Exchange Reactions and Initial GaN Epitaxial Layer Formation under Nitrogen Plasma Exposure of a GaAs Surface,

R. J. Hauenstein, D. A. Collins, M.L. O'Steen, Z. Z. Bandić, S.J. Hwang, and T. C. McGill, *Mat. Res. Soc. Symp. Proc.* **388**, 259 (1995).

The following papers represent the work which was not covered in this thesis:

Halide Vapor Phase Epitaxy of Gallium Nitride films on Sapphire and Silicon Substrates,

N.R. Perkins, M.N. Horton, Z. Z. Bandić, T. C. McGill, and T. F. Kuech, *Mat. Res. Soc. Symp. Proc.* **395**, 243 (1996).

Electronic Structure of GaN stacking faults,

Z. Z. Bandić, T. C. McGill, and Z. Ikonić, *Phys. Rev. B* **56**, 3564 (1997).

Modification of induced surface charges in GaN by light and strain as observed by electric force microscopy,

P. M. Bridger, Z. Z. Bandić, E. C. Piquette, and T. C. McGill, to be published in *J. Vac. Sci. Technol. B*.

Measurement of induced surface charge, contact potentials and surface states in GaN by electric force microscopy,

P. M. Bridger, Z. Z. Bandić, E. C. Piquette, and T. C. McGill, to be published *Appl. Phys. Lett.*

Morphology, polarity, and lateral molecular beam epitaxy growth of GaN on sapphire,

E. C. Piquette, P. M. Bridger, Z. Z. Bandić, and T. C. McGill, to be published in J. Vac. Sci. Technol. B.

Abstract

This thesis describes the developments of novel semiconductor devices based on epitaxial wide bandgap semiconductors GaN and ZnS. The number of interesting and exciting results in physics, electronics and materials science of these systems were found in studies motivated by these devices. This thesis consists of three major topics, structural characterization and kinetic growth modeling of the GaNAs/GaAs superlattices, structural and optical characterization and solid phase recrystallization of ZnS thin films grown on GaN and sapphire substrates, and design and fabrication of GaN high power devices as well as measurement of fundamental electronic properties of GaN, such as minority carrier diffusion lengths and lifetimes and critical field for electric breakdown.

The set of GaNAs/GaAs superlattices grown by molecular beam epitaxy was analyzed by high resolution X-ray diffraction and cross-sectional transmission electron microscopy. The nitrogen incorporation and GaNAs/GaAs interface sharpness were experimentally found to strongly depend on growth temperature. The activation energies for nitrogen desorption and nitrogen to arsenic segregation were found through simple kinetic model, which is in fine agreement with experimentally obtained results. These fundamental studies provide important insights into growth of GaN on GaAs substrates, which is of significant practical importance for all electronic GaN devices.

Zinc sulfide/Gallium nitride heterostructures are potentially interesting system for light emitters in blue and green part of visible spectrum, with DC low power consumption electroluminescent displays being one attractive application of these diodes. Zinc sulfide thin films grown on GaN (0001), GaAs (001) and sapphire (0001) substrates by MBE were characterized by variable temperature photoluminescence and high resolution X-ray diffraction. The structural properties of the films suffered from the large lattice mismatch between ZnS and various substrates which were used. The optical properties of the ZnS films were found to be in direct correlation with

structural properties of the films. The ZnS films doped with Al and Ag grown on n and p-type GaN, and sapphire were characterized by low temperature photoluminescence and displayed bright blue luminescence. Fabricated N-ZnS/p-GaN heterostructures were characterized by current-voltage and electroluminescence. Electroluminescence was found to be centered around 390 nm, corresponding to high energy silver band, and it shifted to higher energies with increase in device voltage. Since as grown films suffered from crystalline imperfections, the ZnS thin films on sapphire were recrystallized, by annealing at temperatures above 900 °C at sulfur overpressure of 10 atm. The structural properties of samples significantly improved, indicating more than 10-fold reduction in tilting and excellent crystallinity. The role of sulfur was discussed, and it was found that sulfur is important in preventing film evaporation, increasing boundary migration and providing compliancy to sapphire substrate.

The minority carrier diffusion lengths and lifetimes were measured for electrons and holes in unintentionally doped, n and p-type GaN samples grown by several different growth techniques. The experimentally observed diffusion lengths were in the 0.2 – 0.3 μm range for Metal-Organic Chemical Vapor Deposition (MOCVD) and Molecular Beam Epitaxy (MBE) grown samples, and 1 – 2 μm in the case of Halide Vapor Phase Epitaxy (HVPE) grown sample. In the case of MOCVD grown samples, the hole lifetime was estimated to approximately 7 ns, and electron lifetime to approximately 0.1 ns. The same samples were structurally characterized by AFM, and the size of the defect-free regions surrounded by linear dislocations is found to be of the order of measured diffusion length, in qualitative agreement with minority carrier recombination at linear dislocations. A simple model is presented which explains an increase in minority carrier lifetime and diffusion length with a decrease in the dislocation density or increase in the size of defect-free grains. A model which explains why linear dislocations might act as recombination sites is also presented.

The important advantage of nitrides and other wide band gap materials for high power devices is a smaller standoff layer thickness for the same standoff voltage, giving smaller ON-state voltage and resistance, smaller power dissipation and larger maximum current density, allowing physically smaller devices for the same power rating.

The design rules for nitride based Schottky rectifiers and thyristors are presented. The critical field for electric breakdown and minority carrier recombination lifetimes are found to be important design parameters. Using modeling parameters which are well in the range currently available with GaN, and measured from fabricated devices, design results indicate the possibility of $18\ \mu\text{m}$ thick GaN Schottky rectifiers and $12\ \mu\text{m}$ thick AlGaN thyristors supporting 5 kV standoff voltage. The critical field for electric breakdown was found to be 5 MV/cm from the theoretical studies. The maximum current density for 5 kV thyristors is in the $200 - 400\ \text{A}/\text{cm}^2$ range depending on the hole lifetime, and is limited by thermal breakdown. The maximum operating frequency of 5 kV thyristors is in the 1-2 MHz range and also depends on the hole lifetime.

Two-terminal GaN Schottky rectifiers were fabricated. The Schottky rectifiers were fabricated on thick GaN layers grown by HVPE and had a standoff voltages in the 450 V to 750 V range, depending on the thickness of the GaN film and contact geometry. Best devices were characterized with reverse current density of $10^{-5}\ \text{A}/\text{cm}^2$ at reverse bias of 100 V, and 4.2 V ON-state voltage at a forward current density of $100\ \text{A}/\text{cm}^2$. Various contact geometries were investigated. It was found that mesa geometry improves ON-state voltage, but causes increase in reverse current density, while that metal field plate geometry significantly reduces reverse current density. The measured critical field for electric breakdown in GaN was found to be $(2.5 \pm 0.5)\ \text{MV}/\text{cm}$ and it approaches the theoretical estimate of 5 MV/cm. The measured values of critical field are only a lower limit since the reverse breakdown voltage was limited by premature corner and edge breakdown.

Contents

Acknowledgements	iv
List of Publications	vii
Abstract	xi
Glossary of Acronyms	xxiii
1 Introduction	1
1.1 Major contributions	1
1.1.1 Comment on collaborative work	3
1.2 Historical overview	4
1.3 Motivation	6
1.4 Thesis outline	7
References	9
2 Structural characterization and growth modeling of GaNAs/GaAs superlattices	10
2.1 Introduction	10
2.2 Experimental details	11
2.2.1 Electron cyclotron resonance microwave nitrogen plasma-assisted molecular beam epitaxial growth of GaNAs/GaAs superlattices	11
2.2.2 High resolution X-ray diffraction	12
2.3 Kinetic modeling	18
2.3.1 Nitridation	18
2.3.2 GaAs Overgrowth - N segregation	21
2.3.3 Determination of nitrogen segregation activation energy	23

2.4	Nitrogen profile smearing - segregation length	23
2.4.1	Cross-sectional transmission electron microscopy	24
2.5	Conclusion	26
	References	27
3	ZnS thin films: optical and structural characterization, light emitters and solid phase recrystallization	29
3.1	Introduction	29
3.2	Principles of operation of p-GaN/ZnS light emitting diodes	30
3.3	Molecular beam epitaxy growth of ZnS	34
3.4	Optical and structural characterization of ZnS thin films	36
3.4.1	Correlation between structural and optical properties of ZnS	36
3.4.2	Low temperature PL study of ZnS grown on GaN substrates	41
3.5	Electroluminescence of ZnS/GaN LED's	41
3.5.1	Device fabrication	41
3.6	High pressure solid phase recrystallization of ZnS thin films	46
3.6.1	Experimental details	47
3.6.2	Structural characterization	47
3.6.3	The role of sulfur	56
3.7	Conclusion	57
	References	59
4	The values of minority carrier diffusion lengths and lifetimes in GaN and their correlation with structural properties	62
4.1	Introduction	62
4.2	Experimental setup	63
4.2.1	Device preparation	63
4.2.2	Electron beam induced current measurements setup	65
4.2.3	Optimization of electron beam current and voltage	68
4.3	Measurements of minority carrier diffusion lengths and lifetimes	71
4.4	Correlation of minority carrier lifetimes with structural defects	76

4.4.1	Experimental observations by Atomic Force Microscopy	76
4.4.2	Simple models for minority carrier lifetime as a function of structural properties: dislocation density or grain size	77
4.4.3	Why would linear dislocations act as recombination centers?	80
4.5	Conclusion	83
	References	84
5	GaN based high power devices: design and fabrication	86
5.1	Design of GaN based high power devices	86
5.1.1	Introduction	86
5.1.2	Nitride based Schottky rectifiers and thyristor switches	87
5.1.3	Thickness and doping of the standoff layer	87
5.1.4	Forward voltage drop for thyristor	92
5.1.5	Power dissipation and maximum current density for thyristor	93
5.1.6	Maximum operating frequency for thyristor	97
5.2	GaN/AlGaN heterostructures	98
5.3	Fabrication of 450 V GaN based Schottky rectifiers	98
5.3.1	Introduction	98
5.3.2	Fabrication procedures	99
5.3.3	Current-voltage measurements	100
5.3.4	Experimental determination of the critical field for electric break- down	111
5.4	Fabrication of 750 V GaN Schottky rectifiers	113
5.4.1	Fabrication procedures	113
5.4.2	Current-voltage characterization	114
5.5	Fabrication of Schottky diodes on p-type GaN	115
5.5.1	Fabrication procedures	115
5.5.2	Current-voltage characterization of p-type GaN Schottky diodes	117
5.6	Conclusion	119
	References	122

Appendix	125
A Simple model for electron beam induced current near Schottky diode in planar geometry	125
References	129
B Influence of infinite recombination on linear dislocations on minority carrier lifetime	130
B.1 Hexagonal array of linear dislocations	130
B.2 Dislocations occupying grain boundaries	132
References	134
C Charged linear dislocations: potential and Debye screening length	135

List of Figures

1.1	The number of paper published per year covering topics related to GaN, GaAs, Si and all science topics.	5
2.1	Schematic of the cross section of the $\text{GaN}_y\text{As}_{1-y}/\text{GaAs}$ superlattice .	12
2.2	Schematic of a commercial Philips PW 1830 diffractometer	13
2.3	The $\omega/2\theta$ rocking curves of the GaAsN/GaAs superlattices	14
2.4	The reciprocal area scan for the superlattice grown at 550°C	15
2.5	Typical agreement between experimental rocking curve and HRS simulated rocking curve.	16
2.6	Arrhenius plot of the nitrogen content y observed in ECR-MBE grown GaAsN/GaAs superlattices	17
2.7	The FWHM's of the -1 and -2 superlattice peaks as a function of temperature	19
2.8	Nitrogen segregation length	24
2.9	TEM micrographs of GaAsN/GaAs superlattices	25
3.1	Schematics of liquid crystal displays	31
3.2	Cross section of AC electroluminescent device	32
3.3	Energy band diagram of the p^+ -GaN/n-ZnS LED	33
3.4	PL and EL setup	37
3.5	Room temperature PL and HR-XRD scans of ZnS films grown on sapphire	39
3.6	The mosaic structure of the films	40
3.7	Integrated room temperature PL as a function of FWHM of X-ray rocking curves	40
3.8	Low temperature ($T = 5\text{ K}$) PL scans of n-type ZnS doped with Al and Ag	42

3.9	Schematic of the fabricated ZnS/p-GaN LED	43
3.10	Current-voltage characteristics of ZnS:(Al,Ag)/p-GaN diode	44
3.11	Room temperature EL of the n-ZnS/p-GaN LED.	45
3.12	Schematics of the experimental setup for sealing quartz ampoules	48
3.13	Summary of X-ray Ω -scans for different recrystallization temperatures of sample II391	49
3.14	Summary of FWHM's of X-ray Ω -scans for different recrystallization temperatures of sample II391	50
3.15	The $\Omega/2\Theta$ -scan of the sample II391 after recrystallization process	51
3.16	The Ω and $\Omega/2\Theta$ -scan X-ray curves of the sample II366 before and after recrystallization process	53
3.17	Explanation of electron channeling	54
3.18	Electron channeling pattern of the sample II366	55
3.19	Surface of the sample II391 recrystallized at 922 °C	56
4.1	Schematic of the Schottky devices processed on the GaN substrates	64
4.2	Scanning electron micrograph of fabricated device used for EBIC mea- surements.	64
4.3	Schematic of the experimental setup for EBIC measurements	66
4.4	Experimental setup for EBIC measurements of minority carrier diffu- sion lengths using Schottky diodes	67
4.5	Generation volume of electrons approximated by sphere of radius R	69
4.6	Generation radius and EBIC signal as a function of electron beam voltage	70
4.7	EBIC line scan profiles and AFM scans of n- and p-type MOCVD GaN	72
4.8	Typical data used to extract diffusion length	74
4.9	AFM scan of the surface of HVPE-grown GaN sample	76
4.10	Hole lifetime and diffusion length as a function of dislocation density	79
4.11	Hole lifetime and diffusion length as a function of average grain size	81
4.12	One-dimensional model of GaN with negatively charged linear disloca- tions	82

5.1	Schematic of nitride based Schottky rectifier and thyristor	87
5.2	Avalanche breakdown and punchthrough condition as a function of doping for GaN and AlGaN	90
5.3	Critical field for electric breakdown as a function of energy bandgap .	91
5.4	ON-state voltage for a thyristor as a function of reverse breakdown voltage and temperature	94
5.5	The equivalent circuit for thermal dissipation calculation	95
5.6	Maximum current density and maximum operating frequency of the thyristor	96
5.7	Schematic of the Schottky rectifiers processed on the GaN	101
5.8	Different device geometries for GaN Schottky rectifiers	102
5.9	The etch rate and SEM micrograph of the profile of the CAIBE etched MOCVD GaN	103
5.10	The SEM micrograph of the $5\ \mu\text{m}$ mesa device.	104
5.11	I-V curve for the high voltage rectifier displaying large standoff voltage	105
5.12	I-V curves of three processed devices showing typical variation in breakdown voltage across the chip.	106
5.13	I-V curves for the three device geometries	107
5.14	Schottky barrier height of gold (Au) on GaN shown as a function of ideality of the contact.	108
5.15	Forward bias I-V characteristics of devices with different geometries and comparison between current flows in lateral and mesa devices . .	109
5.16	SEM photo of the Schottky contact of a diode after breakdown	110
5.17	Breakdown voltage as a function of doping concentration with and without “punch-through” condition.	112
5.18	Schematic of the MOCVD grown $3\ \mu\text{m}$ thick GaN layer grown on HVPE GaN layer.	114
5.19	Current voltage characteristics of the 750 V Schottky rectifiers.	116
5.20	Current voltage characteristics of the Schottky diode on p-type GaN.	118
5.21	Band diagram of the Schottky diode fabricated on p-type GaN. . . .	120

A.1 Schematic of the Schottky diode in the planar geometry 126

List of Tables

4.1	Summary of the EBIC measurements	73
4.2	Summary of the measured, estimated and calculated diffusion lengths and lifetimes from the published literature.	75

Glossary of Acronyms

AC	alternate current
AFM	atomic force microscopy
CAIBE	chemically assisted ion beam etching
CL	cathodoluminescence
DC	direct current
EBIC	electron beam induced current
ECR	electron cyclotron resonance
EL	electroluminescence
FET	field effect transistor
FWHM	full width at half maximum
HEMT	high electron mobility transistor
HFET	heterostructure field effect transistor
HVPE	hydride (or halide) vapor phase epitaxy
HRXRD	high resolution X-ray diffraction
LED	light-emitting diode
MBE	molecular-beam epitaxy
MB	megabyte
MOCVD	metalorganic chemical vapor deposition
PL	photoluminescence
PMT	photomultiplier tube
PN	p-type doped/n-type doped semiconductor junction
RF	radio frequency
RHEED	reflection high energy electron diffraction
SEM	scanning electron microscopy
SIMS	secondary ion mass spectroscopy

SL	superlattice
SPR	solid phase recrystallization
STM	scanning tunneling microscopy
TEM	transmission electron microscopy
UHV	ultra-high vacuum
UID	unintentionally doped
UV	ultraviolet
XPS	X-ray photoemission spectroscopy
XTEM	cross sectional transmission electron microscopy
ZB	zinblende
WZ	wurtzite
WBG	wide bandgap

Chapter 1 Introduction

This thesis describes the design and development of novel devices employing epitaxial wide bandgap semiconductors GaN and ZnS. New findings in physics, electronics and materials properties of the novel materials used for these devices is also presented, and they contribute to the significant portion of this thesis. The thesis consists of three major topics, structural characterization and kinetic growth modeling of the GaN/GaAs superlattices, structural and optical characterization and solid phase recrystallization of ZnS thin films grown on GaN, GaAs and sapphire substrates, and design and fabrication of GaN high power devices as well as measurement of fundamental electronic properties of GaN, such as minority carrier diffusion lengths and lifetimes and critical field for electric breakdown. These three topics are covered in four chapters and three appendices.

1.1 Major contributions

I may say that the development of the novel electronic devices presented in this thesis was the *spiritus movens* for the number of investigations into details of electronic and structural properties of materials used to build these devices. The major results contributed by the author of this thesis are:

- i) **Structural characterization of GaN/GaAs superlattices by high resolution X-ray diffraction and cross-sectional transmission electron microscopy.** This work is important since GaAs can be used as substrate for growth of many GaN-based devices. The structural analysis of these superlattices contributed to understanding of initial growth phases of GaN at GaAs substrates, and mechanisms of nitrogen desorption and segregation. The kinetic model developed to describe these growth mechanisms was found to be in good

agreement with experimental data, and was used to extract quantitative values for nitrogen desorption and segregation activation energies.

- ii) **Structural and optical characterization and solid phase recrystallization of ZnS thin films grown on GaN and sapphire substrates.** The light emitting diodes based on ZnS/GaN heterostructures are potentially very interesting for DC based electroluminescent displays. The structural and optical properties of ZnS thin films were analyzed through high resolution X-ray diffraction and photoluminescence experiments. Fabricated ZnS/GaN heterostructures were analyzed by electroluminescence for light emission. The connection between structural and optical properties of ZnS films was experimentally determined, clearly indicating importance of high crystalline quality. Thin ZnS films grown on sapphire were annealed at high temperatures under high sulfur overpressure and structurally characterized by X-ray diffraction and electron channeling. It was found that crystalline properties improved as much as 10-15 times.
- iii) **Design and fabrication of GaN high power devices and measurements of minority carrier transport properties and critical field for electric breakdown.** GaN with its potentially high critical field for electric breakdown and possibility of GaN/AlGaIn heterostructures has significant potential for high power devices. The design rules for GaN-based Schottky rectifiers and thyristors are given and it was found that critical field for electric breakdown and hole diffusion length and lifetime are important design parameters. Both electron and hole diffusion length and lifetime were measured by electron beam induced current experiments implemented in scanning electron microscope. The measured diffusion lengths were correlated with structural properties of GaN measured by atomic force microscopy. Simple analytical models were developed to quantitatively explain this connection. It was found that the recombination of minority carrier at linear dislocations in GaN limits diffusion length and lifetime in the experimentally observed range. Finally, high voltage Schottky

rectifiers were fabricated with the standoff voltages in the 450 – 750 V range, and critical field for electric breakdown was found to be in good agreement with the high, theoretically predicted values.

1.1.1 Comment on collaborative work

Most of the results in this thesis were obtained through collaborative work. It is therefore important to properly distinguish between the work done by the author of this thesis, and the work of his collaborators:

- i) GaN/GaAs superlattices described in Chapter 1 were grown by Dr. M.L. O’Steen and Prof. R.J. Hauenstein from Oklahoma State University.
- ii) ZnS samples in Chapter 3 were grown by Dr. E.C. Piquette from Caltech. Fabrication and I-V characteristic of ZnS/GaN devices described in Fig. 3.9 and 3.10 were also done by Dr. E.C. Piquette, but it was considered necessary to include those results in this thesis in context of electroluminescence characterization and motivation for structural and optical characterization of ZnS thin films.
- iii) GaN samples in Chapters 4 and 5 were either obtained from ATMI Epitronics (through Dr. J.M. Redwing, Dr. V. Phanse or Dr. R. Vaudo) or Emcore, or were grown at Caltech by E.C. Piquette, or were supplied by Dr. T.F. Kuech from University of Wisconsin. AFM images shown in Fig. 4.7 and 4.9 were done by Dr. P.M. Bridger from Caltech. The calculation of the breakdown voltage of GaN devices based on theoretically obtained impact-ionization coefficients given in Chapter 5 and presented by Eq. 5.1 to Eq. 5.3 was done in collaboration with Dr. E.C. Piquette.
- iv) All other data and calculations presented in this thesis, excluding items (i)-(iii), were done by the author. The author of this thesis allowed various data presented in Chapters 3, 4, and 5 to be used by his collaborators Dr. E.C. Piquette and Dr. P.M. Bridger in their doctoral dissertation theses.

1.2 Historical overview

The wide bandgap refractory semiconductor, GaN, related alloys, and heterostructures have come under active investigation in past few years due to their significant technological promise as useful semiconductor materials for optoelectronics, microwave electronics and high power electronics. Figure 1.1 shows number of GaN-related papers published per year in the period from 1991 to 1998. If we assume that number of scientific papers published in a given year is a measure of the new acquired knowledge and the interest in a given subject (although some might be of the opposite opinion), we can observe a significant trend in this decade. The author of this thesis was lucky enough to work in the period from 1994-1999, when the “interest” growth was 65%/year. If number of GaAs papers is any useful measure (since it is approximately constant or slowly decreasing), it could be expected that the GaN interest will start saturating in the first half of the year 2000, when it is projected that GaAs level will be reached. In some way, it is natural, because a number of GaN products have been successfully commercialized, and a number of the other is under serious consideration. Some might even argue that GaN will find more applications than GaAs, which is also possible. If this trend is continued over the next three years, the number of GaN papers might reach the number of Si-related papers in year 2002. Although it is not expected that GaN can replace Si, Fig. 1.1 clearly indicates that GaN is becoming mature and established material system.

Initial interest in nitrides was generated by successful demonstration and commercialization of blue light emitting diodes [1, 2] by Nichia Chemicals. This initial success was followed by the demonstration (> 10000 hrs) of a blue semiconductor laser [3, 4] and commercialization which was announced in January 1999.[5] The Japanese success in nitride light emitting devices prompted researchers in United States and Europe (as well as their funding agencies) toward other applications of this material, which in approach resembled GaAs efforts in the late 70’s and early 80’s. The initial non-light emitter devices relied on wide bandgap of nitrides to produce solar-blind ultra-violet (UV) photodetectors, which have a wide range of civilian and military applications.

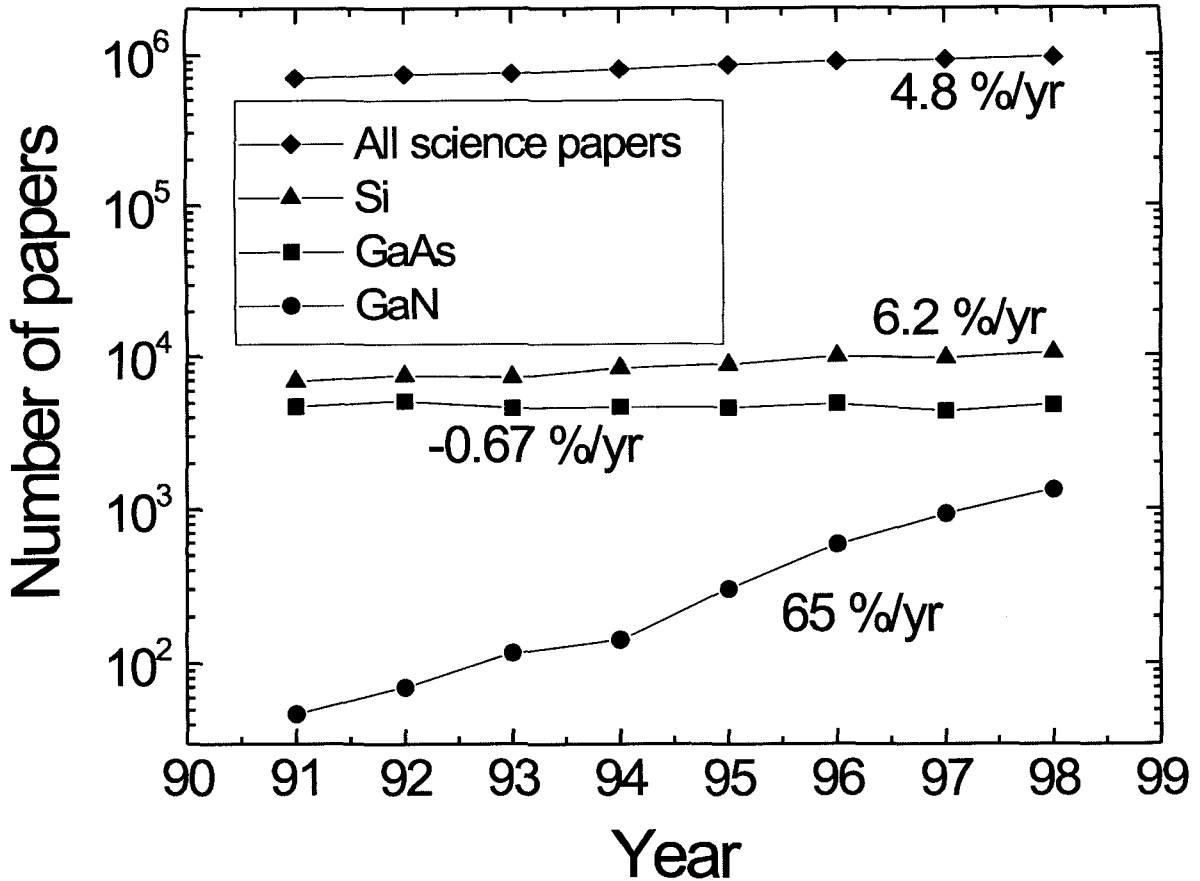


Figure 1.1: The numbers were obtained using SciSearch database. If it is assumed that number of papers published per year corresponds to the new acquired knowledge about particular materials system and the generated interest, the GaN related interest will reach GaAs related interest in the first half of year 2000, and it will reach Si related interest in the year 2002. The compounded growth of 65%/yr. for GaN related subjects indicates significant interest generated for this material system.

Following UV detectors, large critical field for electric breakdown, potentially high operation temperature, high operation frequency and possibility for application of GaN/AlGaN heterojunctions prompted research of high temperature, high frequency and high power electronic devices based on this exciting and novel material system. Some of the devices considered were field effect transistors for high temperature and high power applications, such as Metal Semiconductor Field Effect Transistors (MESFET's), GaN/AlGaN Heterostructure Field Effect Transistors (HFET's) and High Electron Mobility Transistors (HEMT's).[6] The current main-stream research

effort in US and Europe is focused on fabrication of high frequency (>10 GHz) devices and circuits for mobile communications, as well as improvements in the nitrides materials quality. One of the largest and most important obstacles is still the lack of GaN substrate.

The work on Caltech related to GaN was primarily focused on novel applications of GaN. The issue of substrates was investigated through analysis of growth mechanisms of GaN at GaAs substrates, presented in Chapter 1. Visible light emitters based on GaN as efficient minority carrier injector into ZnS was motivation for studies presented in Chapter 3. Finally, measurements of electronic properties of GaN and novel high power devices based on GaN were presented in Chapters 4 and 5.

1.3 Motivation

Numerous reasons motivating the research presented in this thesis were given in more details at the beginning of each chapter. We repeat some of the main reasons here for completeness.

The lack of proper substrate for growth of GaN films is primary motivation for research done on GaN/GaAs superlattices. The goal of this work was to investigate initial growth phases of GaN on GaAs substrates. In the process of this work, GaN/GaAs superlattices were grown, so that processes important for overgrowth of GaAs on GaN were also discussed.

While the majority of GaN related research was focused on light emitting diodes and lasers, the research on Caltech was motivated by possibility of DC electroluminescent (EL) displays. Unlike their counterpart, AC EL displays, they offer significantly lower power dissipation and operate at lower voltages which makes them more suitable for head mounted displays and other portable devices which require usage of small size displays. One possible realization of low power consumption DC electroluminescent displays can be implemented using ZnS/GaN heterostructure light emitting diodes. In this heterostructure, p-type doped GaN is used as an efficient hole injector into n-type doped ZnS, where the hole transfer is favored by the band alignment between

GaN and ZnS.

Beyond visible light emitters, large critical field for electric breakdown, good thermal conductivity and possibility of GaN/AlGaIn heterojunctions open possibility for high power devices for applications in electric utility, motor control, and electric propulsion. There is a number of limitations reached by commercial silicon-based devices, which are related to the critical field of electric breakdown. The thickness of the standoff region required to support given breakdown voltage is inversely proportional to the critical field for electric breakdown. Therefore, the resistance or the ON-state voltage of the device, which is proportional to the thickness, will be also inversely proportional to the critical field, favorizing wide bandgap devices. Finally, the power dissipation is proportional to the device resistance or ON-state voltage. Since the critical breakdown field for GaN is almost twenty times larger than for Si, the performance of GaN devices is expected to be dramatically better in terms of power dissipation. The reduction in power dissipation can lead to significant reduction or complete elimination of bulky cooling packages. However, there are still significant problems to be solved, such as lack of suitable substrates for growth and improvements in material quality which are necessary to achieve larger minority carrier diffusion lengths and lifetimes.

1.4 Thesis outline

The remainder of the thesis is arranged as follows: Chapter 2 describes structural characterization and growth modeling of GaNAs/GaAs superlattices. The high resolution X-ray diffraction, cross-sectional transmission electron microscopy and kinetic modeling of the growth are presented. Important growth parameters are deduced from the modeling.

Chapter 3 describes optical and structural characterization, and solid phase recrystallization ZnS thin films as well as electroluminescence characterization of visible light emitters based on ZnS/GaN heterostructures. After description of basic principles of this device, the connection between structural and optical properties of ZnS

thin films grown on various substrates is established. The structural and optical properties of the films are obtained through high resolution X-ray diffraction and photoluminescence experiments. Electroluminescence of fabricated devices is also presented. Solid phase recrystallization experiments of ZnS thin films are also presented. Crystalline properties of ZnS were found to improve as much as 10-15 times, after recrystallization process.

Chapter 4 describes measurements of the values of minority carrier diffusion lengths and lifetimes in GaN and their correlation with structural properties. Minority carrier diffusion lengths and lifetimes for both electrons and holes are measured in GaN grown by variety of growth techniques. It is found that diffusion lengths and lifetimes are correlated with structural properties, namely with dislocation density and defect-free grain size. The simple analytical models are developed and presented which explain the experimentally observed trends.

Chapter 5 describes design and fabrication of GaN based high power devices. The design rules are given for GaN based Schottky rectifiers and thyristors. It is found that most important modeling parameters are minority carrier lifetime and critical field for electric breakdown. The fabrication of high voltage devices is described, as well as different device geometries. The measurement of critical field for electric breakdown is also presented.

Appendices A, B, and C give analytical calculations required to support material in Chapter 4.

Bibliography

- [1] S. Nakamura, M. Senoh, N. Iwasa, and S. Nagahama, *Appl. Phys. Lett.* **67**, 1868 (1995).
- [2] S. Nakamura, M. Senoh, S. Nagahama, N. Iwasa, T. Yamada, T. Matsushita, H. Kiyoku, and Y. Sugimoto, *Jpn. J. Appl. Phys.* **35** (1996).
- [3] S. Nakamura, M. Senoh, S. Nagahama, N. Iwasa, T. Yamada, T. Matsushita, H. Kiyoku, Y. Sugimoto, T. Kozaki, H. Umemoto, M. Sano, and K. Chocho, *Appl. Phys. Lett.* **72**, 2014 (1998).
- [4] S. Nakamura, M. Senoh, S. Nagahama, N. Iwasa, T. Yamada, T. Matsushita, H. Kiyoku, Y. Sugimoto, T. Kozaki, H. Umemoto, M. Sano, and K. Chocho, *Jpn. J. Appl. Phys. 2 Lett.* **37**, L309 (1998).
- [5] "Nichia announces laser commercialization," *MRS Internet J. N. S. R.* **3**, at <http://nsr.mij.mrs.org/> (Added Wednesday, January 13, 1999).
- [6] S.M. Mohammad and H. Morkoc, *Prog. Quantum. Elecron.* **20**, 361 (1996).

Chapter 2 Structural characterization and growth modeling of GaNAs/GaAs superlattices

2.1 Introduction

Fabrication of GaN films of high crystalline quality, with low defect density, high carrier mobility, and with flat surfaces is essential for practical performance of electronic devices based on GaN, related alloys and heterostructures. The structural qualities in GaN films significantly improved in the past few years, and continue to improve, despite the lack of suitable GaN substrates. The typical defect density in GaN film reduced from 10^{11} cm^{-3} in 1994, to less than 10^7 cm^{-3} which is presently possible by using lateral epitaxial overgrowth techniques. [1, 2] Despite the vast amount of research and the considerable improvement in material quality that has been achieved using techniques such as metalorganic vapor phase epitaxy (MOVPE), hydride vapor phase epitaxy (HVPE), and molecular beam epitaxy (MBE), it remains clear that we are still far from fully understanding all the details and mechanisms of the growth of GaN, particularly by MBE. Many difficulties arise in the growth of GaN epitaxial layers because of the use of a highly mismatched substrate, such as sapphire or silicon carbide. Silicon carbide has many advantages over sapphire for GaN growth, including smaller mismatch in lattice parameter and a distinct crystal polarity, but c-plane sapphire is more often used for reasons of cost.

One of the potentially interesting substrates for GaN, GaAs, attracted some attention in the last few years, [3, 4, 5] mainly to circumvent some of the existing problems with Al_2O_3 and SiC. Besides its use as a substrate, GaAs is also interesting for mixed anion nitride/arsenide systems, such as GaAsN alloys and heterostructures.[6 – 12]

Although limited by a small solubility [13], even small amounts of N in GaAs can cause large band gap bowing into the infrared [13, 14]. There are several important microscopic processes which have to be understood in order to achieve control of the structural and chemical properties of the GaNAs/GaAs interface. Nitridation, or N for As exchange is usually the first step in growing GaN on GaAs substrates, [4, 5, 7] which is analogous to the growth of AlN buffer on Al₂O₃. [15] Another important phenomenon, nitrogen surface segregation, occurs during GaAs overgrowth of the GaAsN layer. [8, 9, 10] It was recently shown [7, 8, 10] that it is possible to produce high quality strained layer GaN_yAs_{1-y}/GaAs superlattices, grown on (001) GaAs substrates. The initial high resolution X-ray diffraction (HRXRD) and reflection high energy electron diffraction (RHEED) characterization revealed the existence of several microscopic, thermally activated processes. In this chapter we describe our assessment of these microscopic processes, and their influence on the interface properties of GaNAs/GaAs superlattices.

2.2 Experimental details

In this section we describe epitaxial growth procedure for GaN_yAs_{1-y}/GaAs superlattices, and their subsequent characterization by high resolution X-ray diffraction.

2.2.1 Electron cyclotron resonance microwave nitrogen plasma-assisted molecular beam epitaxial growth of GaNAs/GaAs superlattices

A set of 36-period GaN_yAs_{1-y}/GaAs superlattices, with a superlattice period consisting of one GaN_yAs_{1-y} monolayer (ML) and 75 GaAs monolayers, was grown on GaAs (100) substrates as a function of temperature (540–580 °C) in an electron cyclotron resonance microwave nitrogen plasma-assisted molecular beam epitaxial (ECR-MBE) system. GaN_yAs_{1-y} monolayers were produced by a brief (4 sec.) N₂ plasma exposure (nitridation) of an As-stabilized GaAs surface. Nitridation was immediately followed

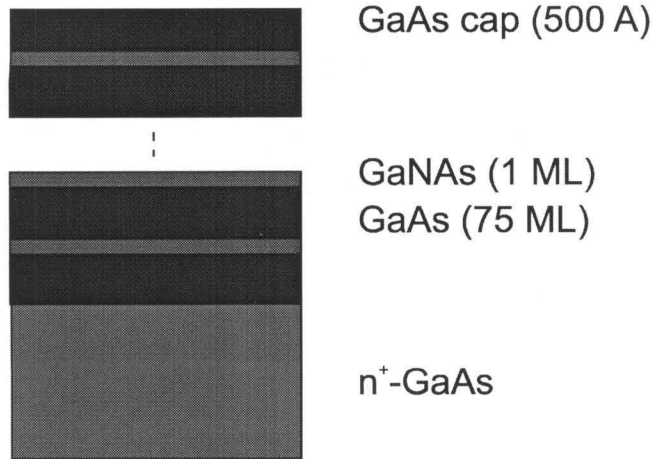


Figure 2.1: Schematic of the cross section of the $\text{GaN}_y\text{As}_{1-y}/\text{GaAs}$ superlattice.

by GaAs overgrowth at a fixed growth rate of 0.75 ML/s for 100 sec. The surface of GaAs is then As-stabilized by exposure to As_2 flux for 30 sec. (As-soak). In addition, one superlattice was grown with 6 sec. nitridation at 550 °C. A schematic of the $\text{GaN}_y\text{As}_{1-y}/\text{GaAs}$ superlattice cross section is shown in Fig. 2.1. Additional details about growth system and procedures can be found elsewhere. [5, 7]

2.2.2 High resolution X-ray diffraction

To determine strain and concentration profiles, the entire sample set is then characterized by *ex-situ* high resolution X-ray diffraction (HRXRD), with the use of a Philips Materials Research Diffractometer (MRD) (see Fig. 2.2). The standard $\omega/2\theta$ scans are performed in the Ge (220) 4-crystal mode around the substrate (004) reflections. The resultant $\omega/2\theta$ rocking curves for 4 sec. nitridation superlattices are presented in Fig. 2.3 (the 550 °C and 570 °C scans have been omitted for clarity). These results reveal a strong dependence on the growth temperature T and indicate the presence of thermally activated microscopic processes.

The reciprocal space scans (area scans) around the substrate (115) reflections are done in the same 4-crystal mode, with the addition of a Bonse-Hart collimator in front of the detector. An area scan of the sample grown at 550 °C is shown in Fig. 2.4. It shows that the superlattice is coherently strained and is of good structural quality.

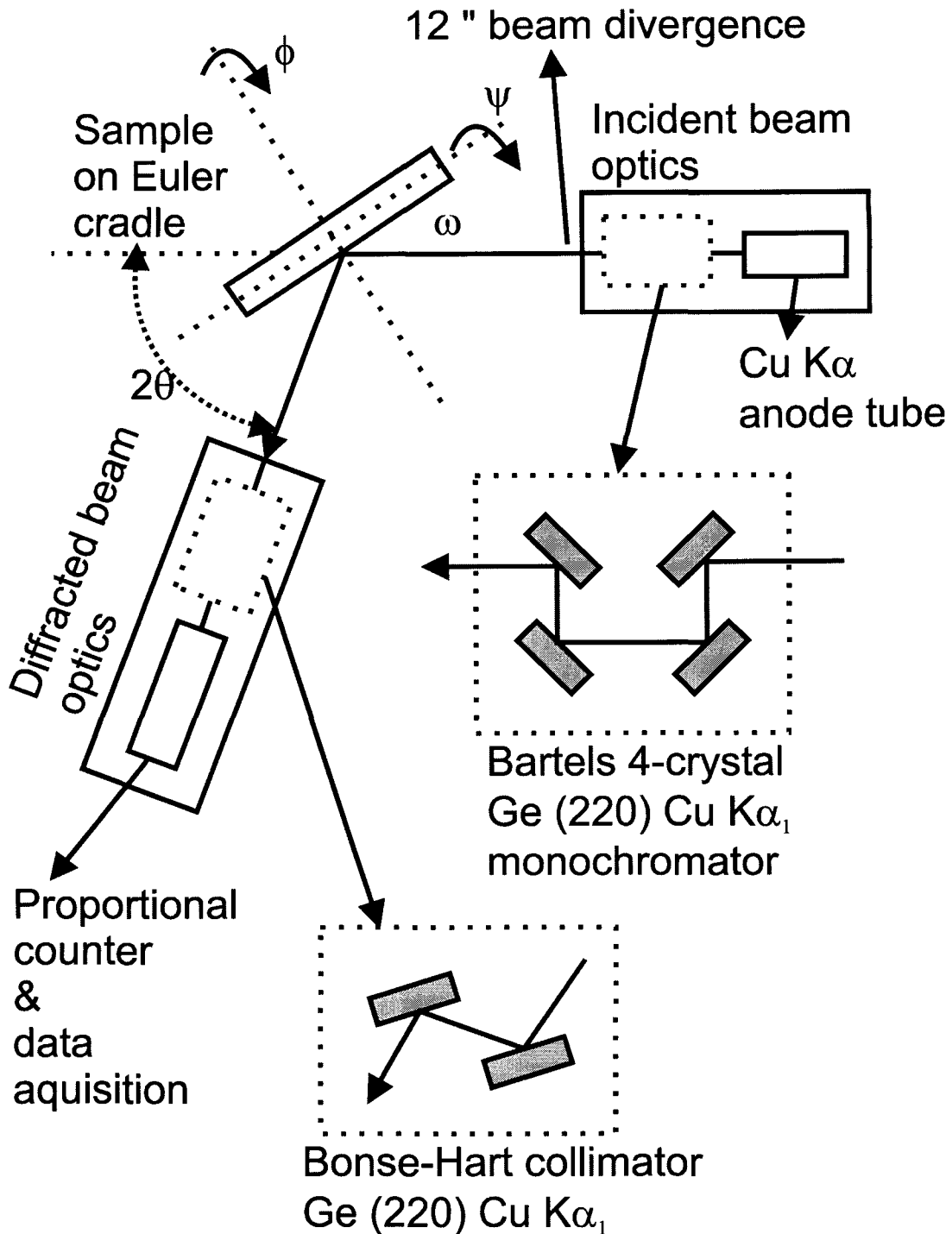


Figure 2.2: Schematic of a commercial Philips PW 1830 diffractometer. Incident beam optics generates X-ray using Copper anode tube. X-rays are collimated using Bartels configuration 4 Ge(220) crystals. The divergence of the beam is approximately 12 arc sec. Sample is attached on Euler cradle which permits rotation around three Euler axes defined by (ω, ψ, ϕ) . The reflected X-ray beam is analyzed by proportional counter. In addition to proportional counter Bense-Hart collimator consisting of two Ge (220) crystals was used in triple axis reciprocal space (area scan) measurements.

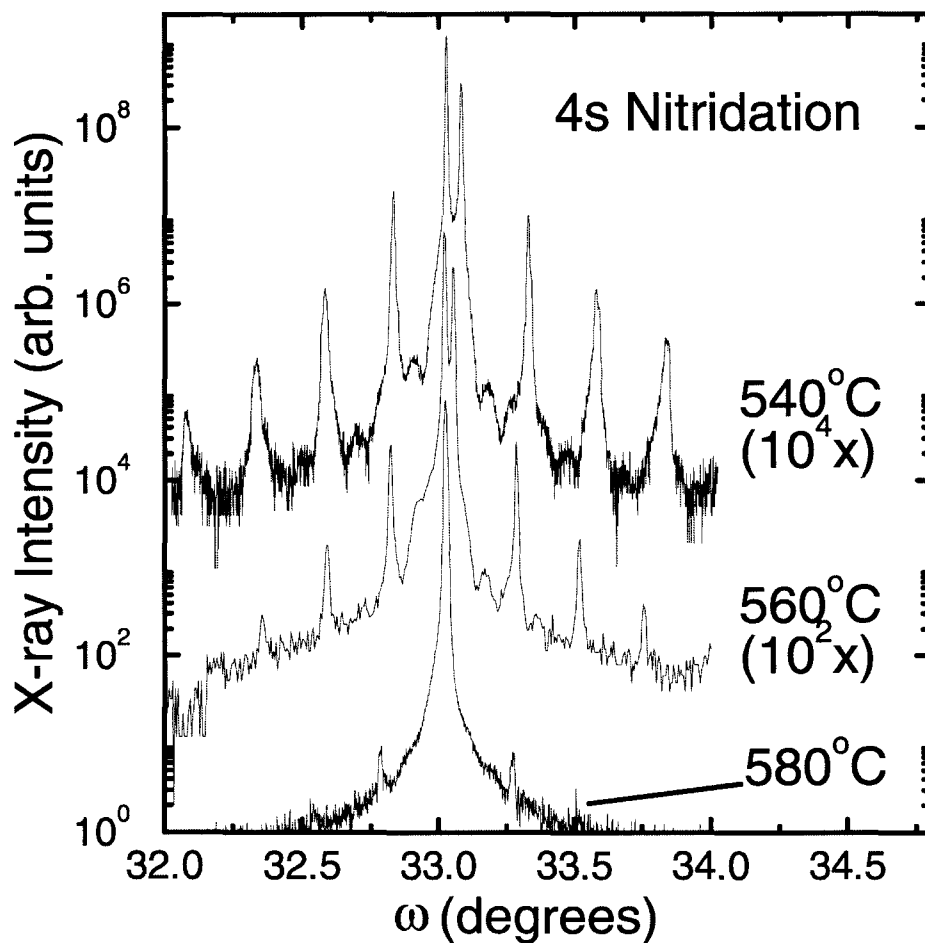


Figure 2.3: The $\omega/2\theta$ rocking curves of the GaAsN/GaAs superlattices grown at temperatures between 540°C and 580°C , with 4 sec. nitrogen exposure time. The strong degradation of the superlattice X-ray diffraction peaks at elevated temperatures can be observed.

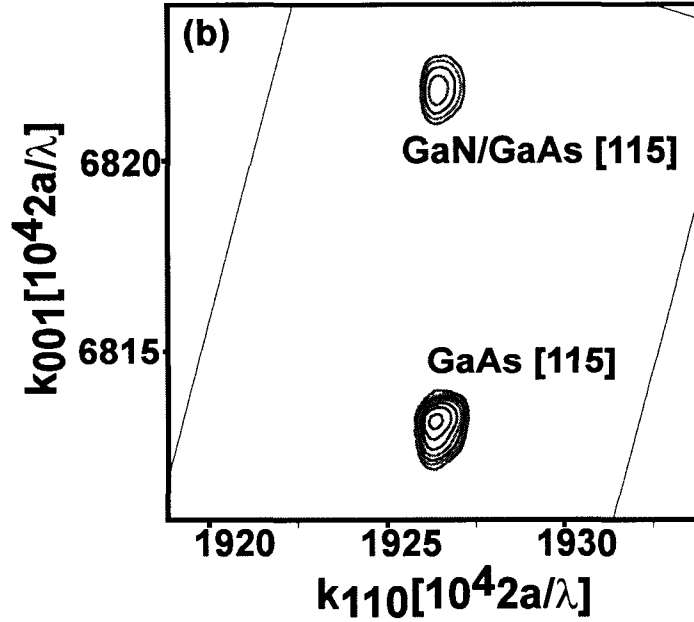


Figure 2.4: The reciprocal area scan for the superlattice grown at 550 °C. The superlattice is coherently strained and is of good structural quality, as observed from the round shape of reciprocal space points. The contours are lines of equal intensities, which increase exponentially with base 2.

The width of the reciprocal space peaks parallel to the layer is small, indicating that tilting of the lattice layers is not present. Two-dimensional equivalent alloy compositions (y) are determined from peak positions and are confirmed through dynamical simulations using the Philips High Resolution Simulation (HRS) software package. The degree of agreement typically obtained between experimental rocking curve and the simulation is presented in Fig. 2.5, on the example of the superlattice grown at 550 °C. Figure 2.6 shows an Arrhenius plot of the resultant compositional dependence on the growth temperature, $y(T)$, for the 4 sec. (circles) and 6 sec. (diamond) nitridations. The experimental uncertainties in temperature, which represent reproducibility from run to run within the sample set, are also indicated. These results suggest the existence of two regimes: (i) A dose-limited regime at low temperatures; (ii) A kinetically limited regime at high temperatures, with an unexpectedly strong fall-off in y at increased growth temperatures.

The interface structural quality is assessed through the temperature dependence of the FWHM's and intensities of superlattice peaks, both of which are shown schemat-

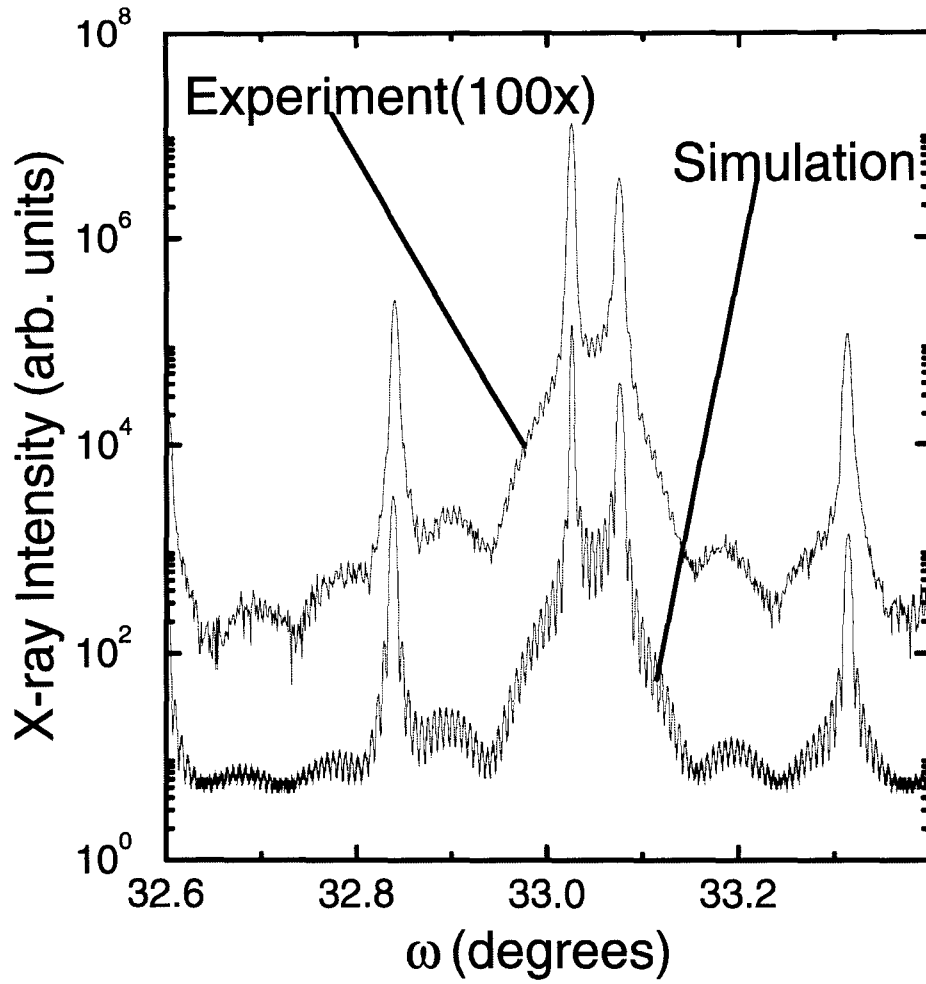


Figure 2.5: Typical agreement between experimental rocking curve and HRS simulated rocking curve.

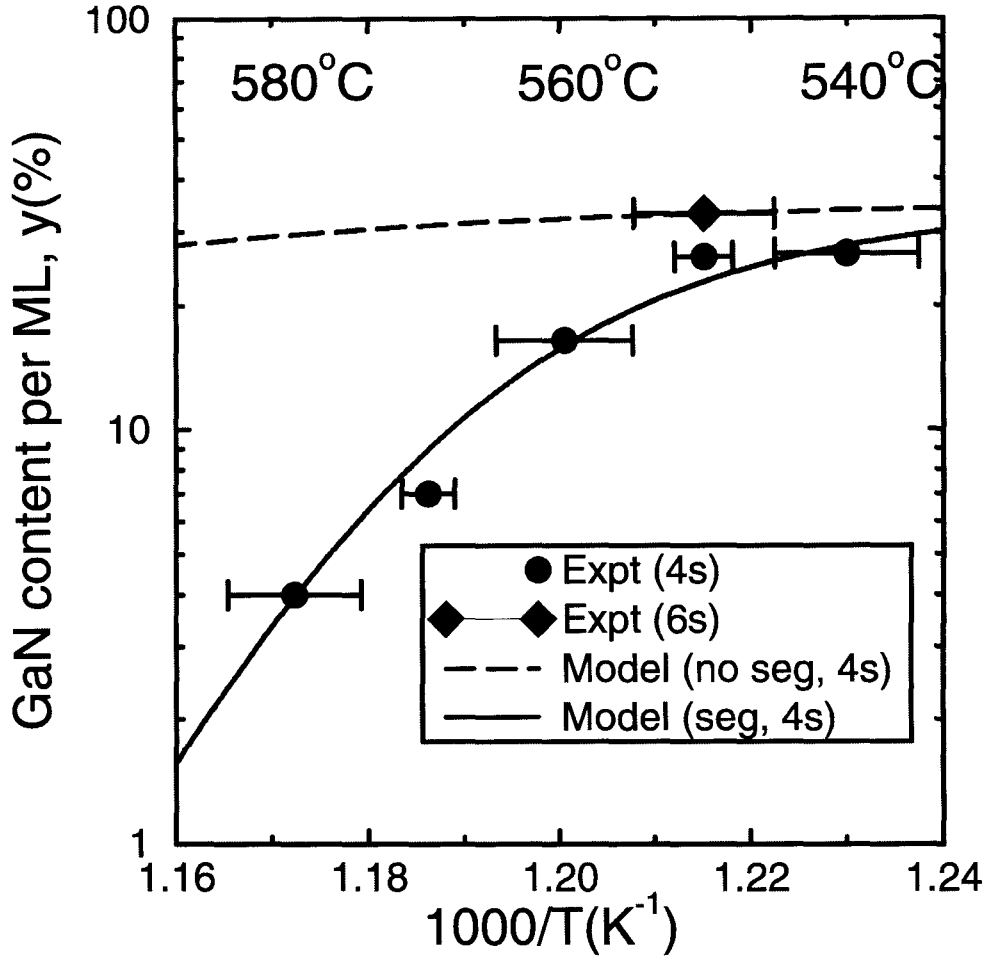


Figure 2.6: Arrhenius plot of the nitrogen content y observed in ECR-MBE grown GaAsN/GaAs superlattices. Experimental data points are obtained through HRXRD measurements for 4 sec. nitridations (circles) and 6 sec. (diamond) nitridations. Growth-kinetics models which explain the strong $y(T)$ dependence observed for ECR-MBE grown δ -GaN $_y$ As $_{1-y}$ /GaAs strained-layer superlattices are also shown. Dashed curve represents the model neglecting N surface segregation [Eq. (2.2) in text], while the solid curve represent the model including segregation effects [Eq. (2.8) in text].

ically in Fig. 2.7. FWHM's of the -1 and -2 superlattice peaks as a function of temperature are shown in the Fig. 2.7 using the left vertical scale. The rise of FWHM's at 540°C is attributed to a growth temperature too low for GaAs growth. The dependence of the superlattice peak intensities from the peak order is a measure of the sharpness of the interface. Sharp interfaces give rise to the superlattice rocking curves with many peaks and slow peak decay with peak order, while superlattices with diffuse interfaces have few peaks which quickly become indistinguishable in the higher order, with the best example being alloys which only have a crystalline lattice peak. The intensity of the superlattice peaks as a function of the order of peak is fitted to the Lorentzian curve $Aw/(n^2 + w^2)$, where n is an order of the superlattice peak, w is the width of the Lorentzian curve and A the multiplicative constant. The Lorentzian curve is chosen to provide a parameter which could describe peak intensity as a function of peak order. The parameter w thus represents the quantitative measure of the smearing of the interface, and is plotted in Fig. 2.7 as a function of temperature, using the right vertical scale. From Figs. 2.6 and 2.7 we can notice rapid changes with temperature, where, at elevated temperatures N content is quite reduced, while interface quality is deteriorated.

2.3 Kinetic modeling

For the purpose of understanding the physical origin of this $y(T)$ dependence, we have developed a first-order kinetic model which explicitly incorporates the three phases of our particular superlattice growth sequence: *(i)* nitridation; *(ii)* overgrowth and *(iii)* As-soak, as described in section 2.2.

2.3.1 Nitridation

The net rate of surface nitridation is determined by two physical processes which have been previously identified. [5] They are: *(i)* N-for-As surface anion exchange (N gain), and *(ii)* surface N desorption (N loss). These processes can be analytically modeled,

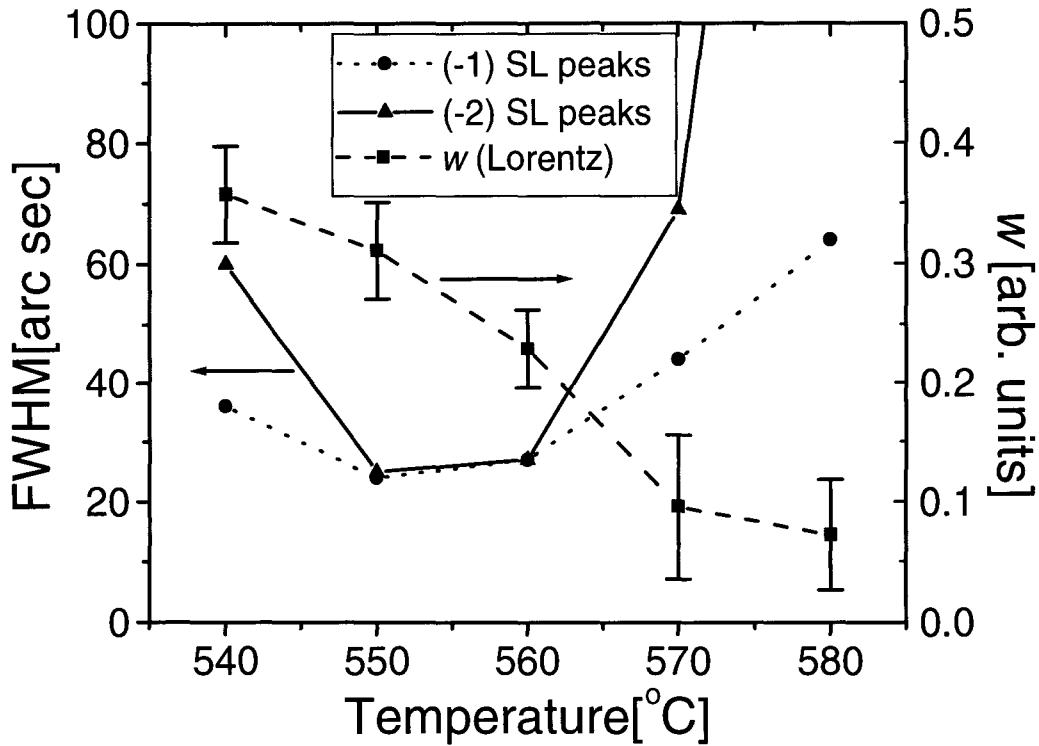


Figure 2.7: The FWHM's of the -1 and -2 superlattice peaks (left vertical axis) as a function of temperature. The Lorentzian fit $Aw/(n^2 + w^2)$ of the dependence of the superlattice peak intensities as a function of the order n of superlattice diffraction gives parameter w (right vertical axis). They both show deterioration of structural properties and interface sharpness at high temperatures.

to the first order in N surface composition, y , as:

$$\frac{dy}{dt} = s\Phi(1 - y) - \frac{y}{\tau_d} \quad . \quad (2.1)$$

The first term on the right-hand side of Eq. (2.1) corresponds to the N gain on the As-stabilized GaAs surface due to the energetically favorable anion exchange. This process is modeled as being proportional, in the first order, to the flux Φ of incident physically activated N; to the fraction of available As surface sites to be exchanged with N, and to an overall efficiency factor s (units of area), which in general might depend on surface chemistry, strain and temperature, but is approximated as constant over the temperature and composition range of interest, for the purpose of our simplified model. The second term in this equation, $-y/\tau_d$, represents the N loss due to surface desorption. It can be modeled in terms of a thermally activated rate constant, $\tau_d^{-1} = \tau_{0d}^{-1} \exp(-E_d/kT)$, with activation energy E_d . Such a process has been directly observed in RHEED measurements of nitrided GaAs surfaces, and estimates for E_d (~ 2.1 eV) have been previously reported. [5, 7]

If we define an “effective dosing rate” $r \equiv s\Phi$, the solution to Eq. (2.1) for an initially N-free (As-stabilized) surface can be written as:

$$y(t_{\text{exp}}) = y_{\text{ss}}[1 - \exp(-t_{\text{exp}}/\tau)] \quad , \quad (2.2)$$

where $y_{\text{ss}} \equiv r\tau$ and $\tau \equiv (\tau_d^{-1} + r)^{-1}$, and t_{exp} is the nitrogen plasma exposure time. If Eq. (2.2) is considered in the limit of low temperatures, so that desorption rate τ_d^{-1} is negligible, then $y \rightarrow 1$ would be obtained. This reflects the assumption that As atoms from the As-enriched (100) GaAs surface, when exposed to N plasma, will be completely exchanged for N atoms in the steady state, since an N terminated surface has a lower surface free energy due to a much stronger Ga-N bond compared to a Ga-As bond (heats of formation 6.81 eV and 5.55 eV, respectively [16]). Although the essential nitridation kinetics is well described by Eq. (2.2) without unnecessary mathematical complexity, it ignores the subsequent stages of growth of our superlattices, and therefore cannot be used to directly model our experimental results. This

can be seen in Fig. 2.6, where the dashed curve represents the plot of Eq. (2.2) taking $t_{\text{exp}} = 4$ sec. and using our RHEED based experimental desorption parameters, $E_d = 2.1$ eV, and $\tau_d = 7$ sec. at 592 °C. [5, 7] In addition, the dosing rate r is estimated to be approximately 0.1 Hz from experimental values of y at 550 °C for 4 sec. and 6 sec. nitridations, such that Eq. (2.2) properly describes the dose-limited (low temperature) regime of growth.

2.3.2 GaAs Overgrowth - N segregation

Inspection of Fig. 2.6 clearly reveals that the processes of anion exchange and N surface desorption *alone* result in the weak fall-off of the model (dashed) curve, and thus cannot account for the strong $y(T)$ dependence in the kinetically limited growth regime. Also, even N surface desorption during the short monolayer deposition time (t_{ML}) required to bury (and freeze-in) the nitrided $\text{GaN}_y\text{As}_{1-y}$ layer cannot result in significant N loss. To overcome this, we hypothesize that a thermally activated N surface segregation process, described with rate constant $\tau_s^{-1} = \tau_{0s}^{-1} \exp(-E_s/kT)$, is occurring concurrently with N desorption, during GaAs overgrowth. [7] This assumption is supported qualitatively by our experimental observation that a GaN-related (3×3) surface reconstruction proceeds faster to a GaAs (2×4) reconstruction at lower substrate temperature during GaAs overgrowth which is consistent with freeze-out of a thermally activated N segregation process.

Let us assume that: (1) segregation occurs from the first subsurface layer upward to the current surface layer; (2) desorption occurs from all currently exposed surfaces, i.e., the current growth surface and the current partially exposed first sub-surface layers; and (3) the segregation and desorption processes are statistically independent, and are occurring concurrently. Also, let S_n represent a relative GaN mole fraction in monolayer n . Under these assumptions, we can relate the N content of monolayers n and $n + 1$ through:

$$S_{n+1}(0) = [S_n(0) - S_n(t_{\text{ML}})] \frac{\tau_s^{-1}}{\tau_s^{-1} + \tau_d^{-1}} \quad (2.3)$$

Equation (2.3) describes the fraction of lost N $[S_n(0) - S_n(t_{\text{ML}})]$ which segregates rather than desorbs, and becomes the nitrogen content of the next surface layer. Since layer n loses its N content due to both N desorption and segregation, during the time interval $0 \leq t \leq t_{\text{ML}}$, $S_n(t)$ decays exponentially as $S_n(0) \exp(-t/\tau_{\parallel})$, where $\tau_{\parallel}^{-1} \equiv (\tau_s^{-1} + \tau_d^{-1})$. Using this expression in Eq. (2.3) lead us to:

$$S_{n+1}(0) = S_n(0) [1 - \exp(-t_{\text{ML}}/\tau_{\parallel})] \frac{\tau_d}{\tau_{\text{tot}}} \quad , \quad (2.4)$$

where $\tau_{\text{tot}} \equiv \tau_s + \tau_d$. It is obvious from Eq. (2.4) that $S_n(0)$ represents a geometrical progression. Now, similarly to Eq. (2.3), we can define δ_n as the amount of initial material lost through desorption from layer n :

$$\delta_n \equiv [S_n(0) - S_n(t_{\text{ML}})] \frac{\tau_s}{\tau_{\text{tot}}} \quad . \quad (2.5)$$

Therefore, the total loss of nitrogen from one superlattice period during overgrowth would be:

$$L = \sum_{n=0} \delta_n \quad , \quad (2.6)$$

which is simply a sum of a geometric progression. Finally, the total amount of the original GaN content retained within one period of a superlattice is $R = 1 - L$, or straightforwardly

$$R = \frac{\tau_{\text{tot}}}{\tau_d + \tau_s e^{t_{\text{ML}}/\tau_{\parallel}}} \quad . \quad (2.7)$$

It is important to note that the expression for R given in Eq. (2.7) gives the correct limiting behavior in describing the loss of N during the GaAs overgrowth in the limits of no segregation, or no desorption. If there is desorption, but no segregation, then the only opportunity for N loss would be before the nitrided layer is completely buried in GaAs: i.e., $R = \exp(-t_{\text{ML}}/\tau_d)$, which is obtained directly from Eq. (2.7) in the limit $\tau_s \rightarrow \infty$. Similarly, if there is segregation, but no desorption, then R must be unity, since the only possible mechanism for N loss is desorption process. In that case, where $\tau_d \rightarrow \infty$, one would obtain $R \rightarrow 1$, as it should be.

2.3.3 Determination of nitrogen segregation activation energy

Using the “segregation correction factor” from Eq. (2.7), it is clear that in order to consistently incorporate N surface segregation into our model, Eq. (2.2) must be replaced by

$$y(t_{\text{exp}}) = y_{\text{ss}}[1 - \exp(-t_{\text{exp}}/\tau)] \times \left[\frac{\tau_{\text{tot}}}{\tau_d + \tau_s e^{t_{\text{ML}}/\tau_{\parallel}}} \right]. \quad (2.8)$$

Thus, Eq. (2.8) represents the final result of our model and quantitatively describes the growth sequence (nitridation/overgrowth/soak) of our $\text{GaN}_y\text{As}_{1-y}/\text{GaAs}$ superlattices, taking into account microscopic processes of anion exchange, desorption and segregation. It is plotted as the solid curve in Fig. 2.6. This curve is calculated using identical dosing (r) and desorption (E_d and τ_{0d}) parameter values which were used in Eq. (2.2) to obtain dashed curve, while adjusting at the same time two segregation parameters, E_s and τ_{0s} . A nonlinear least-squares fit to the experimental data points for 4 sec. nitridations finally results in the estimate for N surface segregation energy of $0.9 \text{ eV} \pm 30\%$. Obviously, from Fig. 2.6, it is seen that the corrected Eq. (2.8) is in very good agreement with experimental data, and confirms our N surface segregation hypothesis.

2.4 Nitrogen profile smearing - segregation length

One of the important applications of the described kinetic model is the N profile smearing. Nitrogen profile smearing follows from the geometrical progression S_n . By assuming a continuous function $S_n(z)$ for the N profile, it is easy to show using Eq. (2.4) that $S_n(z) = S_n(0) \exp(-z/l)$ where l is the segregation length:

$$l = -\frac{a}{2 \ln\left\{ \left[1 - \exp(-t_{\text{ML}}/\tau_{\parallel}) \right] \frac{\tau_d}{\tau_{\text{tot}}} \right\}}. \quad (2.9)$$

The segregation length represents the decay length of the N profile and is therefore a useful parameter which quantitatively defines the interface quality. A plot of Eq. (2.9)

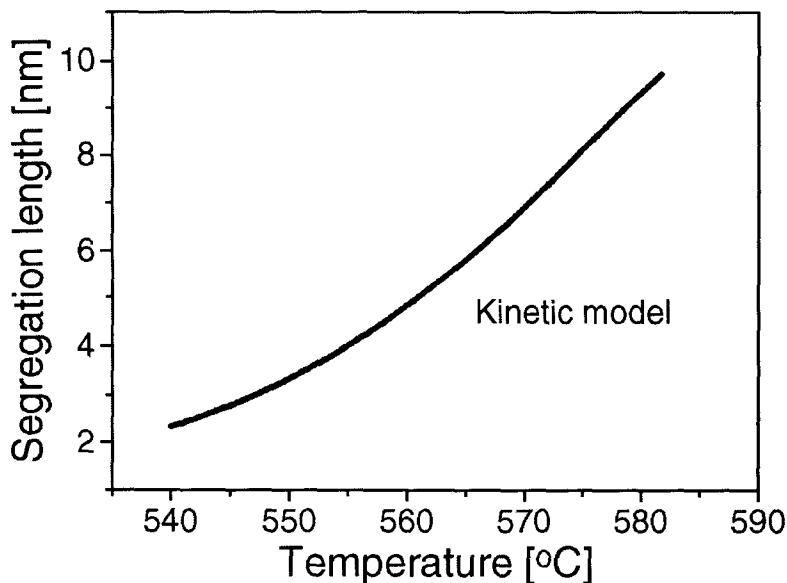


Figure 2.8: Nitrogen segregation length derived from the kinetic model [Eq. (2.9)]. It shows that the model predicts increase of nitrogen segregation length as temperature increases.

for 4 sec. N exposures is given in Fig. 2.8, from which it can be seen that segregation length increases with temperature. Unfortunately, profile smearing limits the abruptness of the GaN/GaAs interface. However, it is possible that smearing effects might be controlled through some of the MBE techniques which have been successfully used in the problem of dopant-profile smearing in MBE-grown Si. [17] Also, direct imaging techniques such as cross-sectional Transmission Electron Microscopy (TEM) or Scanning Tunneling Microscopy (STM) might provide another way to determine E_s , since our model predicts distribution of nitrogen in the superlattice period ($S_n(0)$), as a function of N surface activation energy E_s and growth temperature T .

2.4.1 Cross-sectional transmission electron microscopy

To experimentally confirm our hypothesis about nitrogen segregation we made cross-sectional TEM observations of our $\text{GaN}_y\text{As}_{1-y}/\text{GaAs}$ superlattices. It is expected that nitrogen segregation should be directly observable at cross-sectional images of

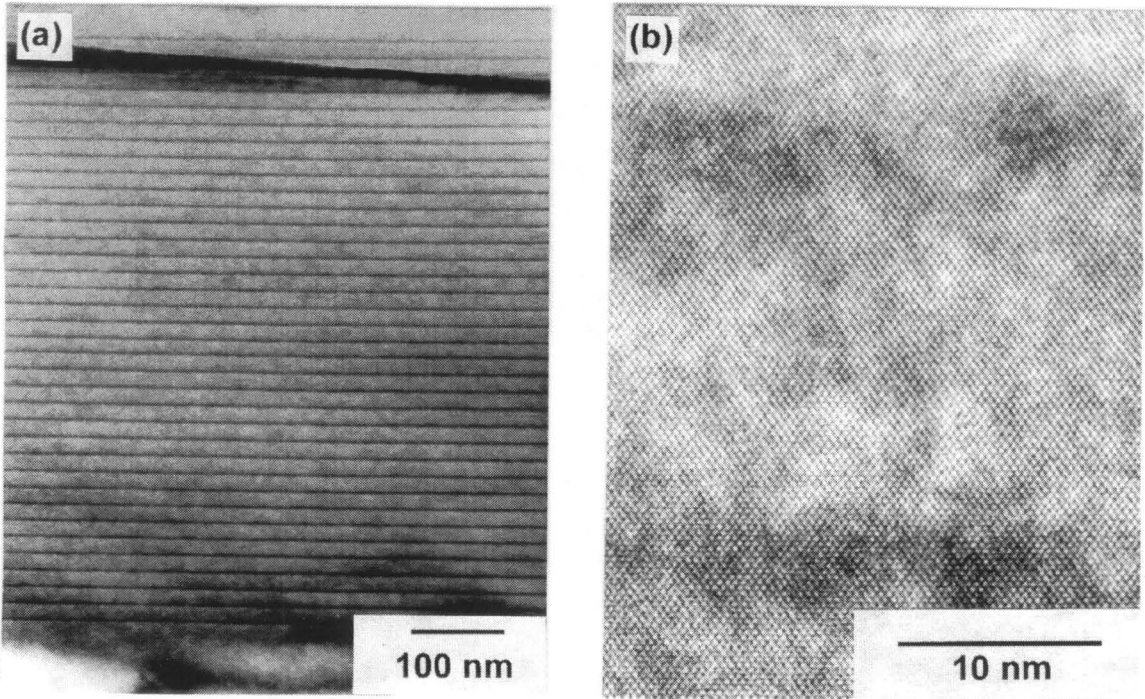


Figure 2.9: (a) Bright field TEM micrograph of the (110) cross section of the GaAsN/GaAs superlattice grown at 550 °C. The entire superlattice can be observed. The measured thickness of GaAsN layers is around 3nm, in good agreement with the model [Fig. 2.8] (b) The (110)high resolution micrograph of the GaAsN/GaAs superlattice. There are no GaN clusters observed.

the superlattices, provided that appropriate resolution is achieved in the image. Since our modeling results suggest nitrogen segregation length of the order of 2 – 10 nm, it is necessary to achieve atomic resolution in TEM. Cross sections of the superlattices were prepared by polishing, dimpling and Ar ion-beam milling. Transmission electron microscopy images were acquired in Philips EM430 electron microscope. Figure 2.9(a) shows a bright field TEM micrograph of the cross section of the $\text{GaN}_y\text{As}_{1-y}/\text{GaAs}$ superlattice grown at 550 °C, near the [110] zone axis, but normal to the surface. The (110) high resolution image of the superlattice is shown in Fig. 2.9(b). We did not observe GaN clustering, contrary to the results of a cross sectional STM study done on a similar structure. [11, 12] Both of the micrographs in Fig. 2.9 indicate that the extent of the N profile smearing is indeed of the order of 3nm, in excellent agreement with the calculations obtained from the model.

2.5 Conclusion

A set of $\text{GaN}_y\text{As}_{1-y}/\text{GaAs}$ superlattices grown by ECR-MBE have been characterized *ex-situ* by HRXRD and cross-sectional TEM. It was experimentally found that nitrogen content ($y(T)$) and interface sharpness depend strongly on growth temperature. A simple, but plausible kinetic model has been developed to conclusively establish and quantitatively explain some of the microscopic processes observed in $\text{GaN}_y\text{As}_{1-y}/\text{GaAs}$ strained layer superlattices. Particularly, the strong $y(T)$ dependence, obtained through *ex-situ* HRXRD of our superlattices, is fully understood in terms of energetically favorable surface anion exchange and combined, thermally activated N surface-segregation/surface-desorption. Also, the model predicts for the first time numerical estimates of the kinetic parameter associated with N surface-segregation process, $E_s \cong 0.9 \text{ eV} \pm 30\%$, which appear to be significant under typical GaN/GaAs ECR-MBE growth conditions. Finally, the model predicts nitrogen profile smearing at the optimal growth temperatures of 550°C to be on the order of 3nm. Nitrogen profile smearing has been verified experimentally by cross-sectional TEM, and experimental observations were found to be in excellent agreement with the kinetic model.

Bibliography

- [1] C. Sasaoka, H. Sunakawa, A. Kimura, M. Nido, A. Usui, and A. Sakai, *J. Cryst. Growth* **190**, 61 (1998).
- [2] D. Kapolnek, S. Keller, R. Vetry, R.D. Underwood, P. Kozodoy, S. P. Den Baars, and U. K. Mishra, *Appl. Phys. Lett.* **71**, 1204 (1997).
- [3] O. Brandt, H. Yang, A. Trampert, and K.H. Ploog, *Mat. Res. Soc. Symp. Proc.* **395**, 27 (1995).
- [4] M. Sato, *J. Appl. Phys.* **78**, 2123 (1995).
- [5] R.J. Hauenstein, D.A. Collins, X.P. Cai, M.L. O'Steen, and T.C. McGill, *Appl. Phys. Lett.* **66**, 2861 (1995).
- [6] M. Sato, *Mat. Res. Soc. Symp. Proc.*, **395**, 285 (1995).
- [7] R.J. Hauenstein, D.A. Collins, M.L. O'Steen, Z.Z. Bandić, and T.C. McGill, *Mat. Res. Soc. Symp. Proc.*, **388**, 259 (1995).
- [8] Z.Z. Bandić, R.J. Hauenstein, M.L. O'Steen, and T.C. McGill, *Appl. Phys. Lett.* **68**, 1510 (1996).
- [9] Z.Z. Bandić, T.C. McGill, R.J. Hauenstein, and M.L. O'Steen, *J. Vac. Sci. Technol. B* **14**, 2948 (1996).
- [10] Z.Z. Bandić, R.J. Hauenstein, M.L. O'Steen, and T.C. McGill, *Mat. Res. Soc. Symp. Proc.*, **449**, 209 (1997).
- [11] R.S. Goldman, R.M. Feenstra, B.G. Briner, M.L. O'Steen, and R.J. Hauenstein, *Appl. Phys. Lett.* **69**, 3698 (1996).

- [12] R.S. Goldman, R.M. Feenstra, B.G. Briner, M.L. O'Steen, and R.J. Hauenstein, J. Electr. Mater. **26**, 1342 (1997).
- [13] J. Neugebauer and C.G. Van de Walle, Phys. Rev. B **51**, 10568 (1995).
- [14] S. Sakai, Y. Ueta, and Y. Terauchi, Jpn. J. Appl. Phys. **32**, 4413 (1993).
- [15] N. Grandjean, J. Massies, and M. Leroux, Appl. Phys. Lett. **69**, 2071 (1996).
- [16] CRC Handbook of Chemistry and Physics, edited by R. C. West (CRC, Boca Raton, FL, 1987), P. E102.
- [17] H. Jorke, Surf. Sci. **193**, 569 (1988).

Chapter 3 ZnS thin films: optical and structural characterization, light emitters and solid phase recrystallization

3.1 Introduction

Zinc sulfide, with its wide band gap (~ 3.8 eV) and excellent luminescence, which can be obtained in almost the whole visible range with suitable dopants, is a very attractive material for light emitting diodes (LED's), [1, 2] lasers, [3] and flat-panel electroluminescent (EL) displays. [4, 5] However, difficulties in producing high quality p-type doped material have reduced the utility of the sulfide system.

The enormous interest generated by GaN-based light emitters made p-type GaN material available. [6, 7, 8] Since the GaN valence band edge is below that of ZnS, [9] it has been proposed that p-type GaN may be an efficient hole injector into ZnS, CdS and other light emitting semiconductors. [10] GaN/Zn(Cd)S heterostructures are attractive for both discrete diodes in blue and green region of visible spectrum and integrated direct current (DC) EL displays. Discrete diodes also have significant potential in traffic lights and large sized (> 10 m) color displays, where emission over whole visible spectrum is required. Integrated DC EL displays seem extremely attractive for head mounted ($\approx 2 - 5$ cm in size) displays which are interesting for military and mobile computing applications and for color displays ($\sim 10 - 20$ cm) in laptop computers. Rapid developments in the internet and communications industry, as well as trends in electronics and storage miniaturization (such as 1 inch 340 MB hard disks [11]) should spawn a variety of mobile, palm-top size electronics devices, and each one of them will need to have medium sized color display. The crucial advantage of DC EL displays, compared to other technologies such as passive

and active matrix liquid crystal displays, [12] and alternate current (AC) EL displays, [12, 13] is a reduction in power consumption. Liquid crystal displays generate color pixels employing red, green or blue filters and pair of polarizers which determine light transmission from back-panel light source (see Fig. 3.1 [12]). In this way a considerable amount of energy is wasted, by continuous back lighting, and only small part of generated light is transmitted. AC EL displays require high voltages of approximately $\sim 100 - 150$ V to generate light by impact excitation of light emitting centers, typically in ZnS powder, by high energy electrons (see Fig.3.2 [13]). Although AC EL displays share a similar material system (ZnS), the high voltages required to generate light and overall power consumption are far from satisfactory, especially for portable and mobile computing applications. In the case of DC EL displays based on ZnS, voltages required to turn-on individual diodes are approximately 3 – 5 V, while at the same time current densities are comparable to AC EL devices. This reduction in voltage and current results in almost two orders of magnitude lower power consumption.

In this chapter, materials studies of ZnS thin films motivated by LED's based on p-GaN/n-ZnS heterostructure are described. The structural and optical characterization of ZnS layers, electroluminescence characterization of fabricated devices, and finally high pressure ZnS thin film solid phase recrystallization are discussed.

3.2 Principles of operation of p-GaN/ZnS light emitting diodes

Since ZnS has not been yet successfully doped p-type, it is not possible to produce an EL device with p/n homojunction system. One alternative to p-ZnS is to use other wide band gap materials which can be doped p-type and have favorable band offsets compared to ZnS. One example is p^+ -GaN/n-ZnS diode. The principle of operation is shown on the band energy diagram in Fig. 3.3. The top of the valence band of GaN lies approximately $E_v \approx 1$ eV below the top of the valence band of

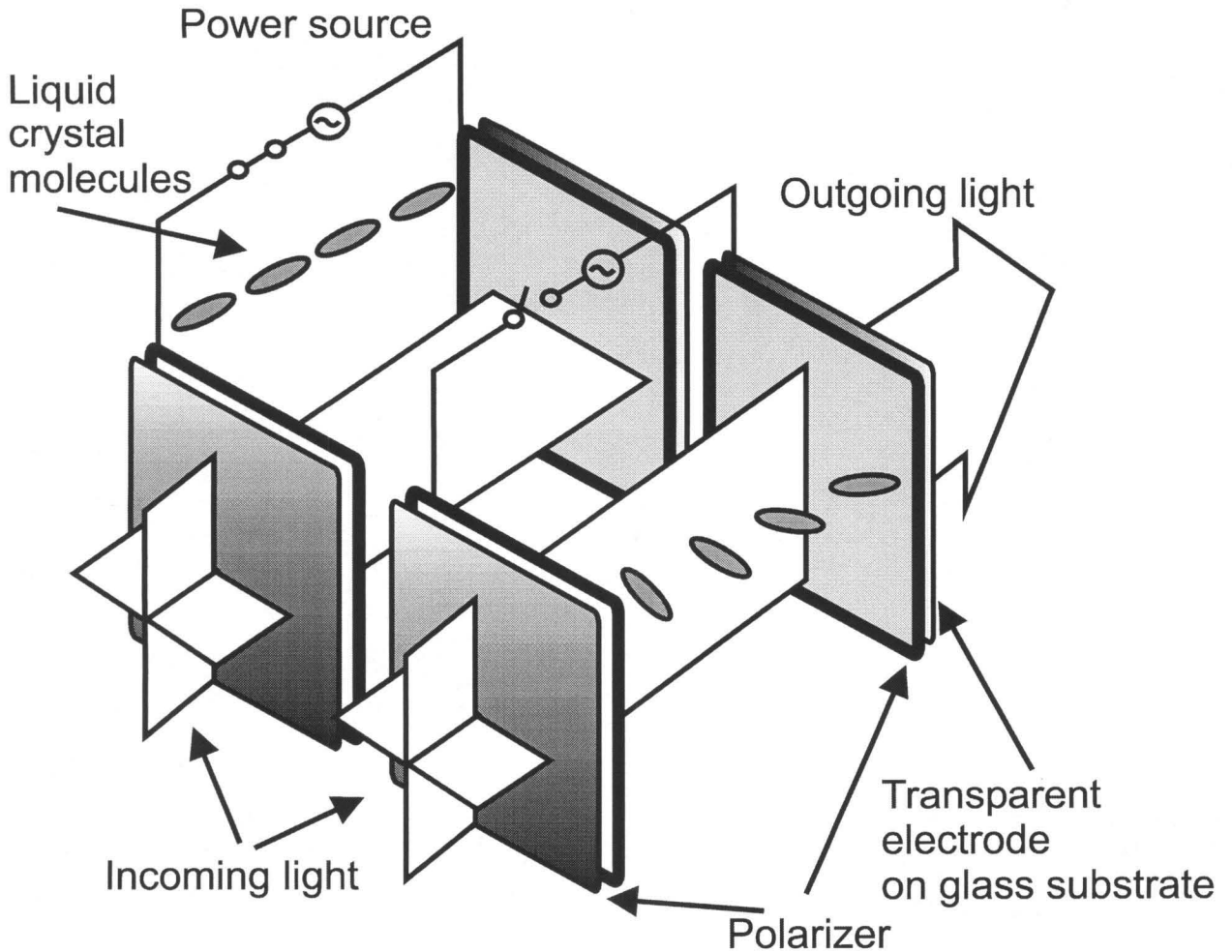


Figure 3.1: Schematics of liquid crystal displays. The orientation of liquid crystal molecules is very sensitive to the externally applied electric field. Each single pixel is formed by optically tunable shutter that is controlled by a locally applied electric field and is sandwiched between a pair of polarizers. Light image is produced by addressing top and bottom line electrodes of the cell.

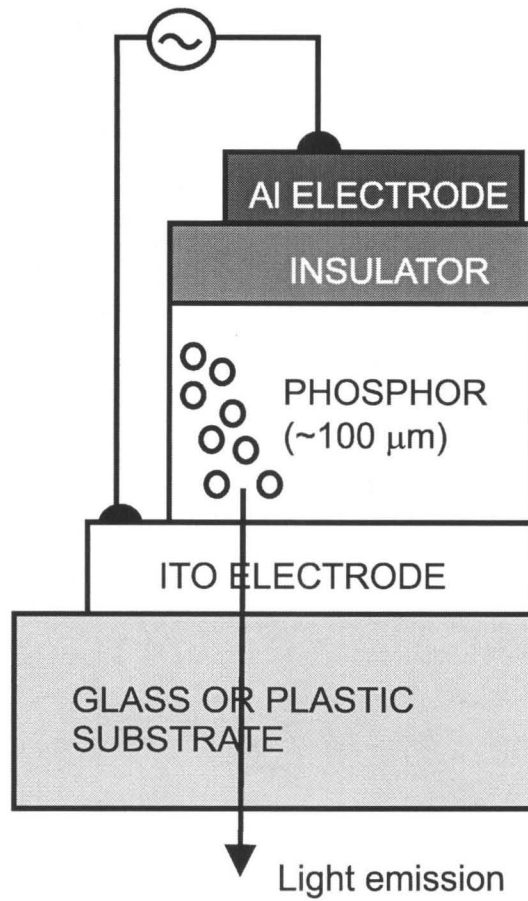


Figure 3.2: Cross section of AC electroluminescent device. Large AC voltage causes variation in electric field which cause impact excitation of light emitting centers. For example, Cu and Cl act as blue or green luminescence centers depending on relative amount of Cl.

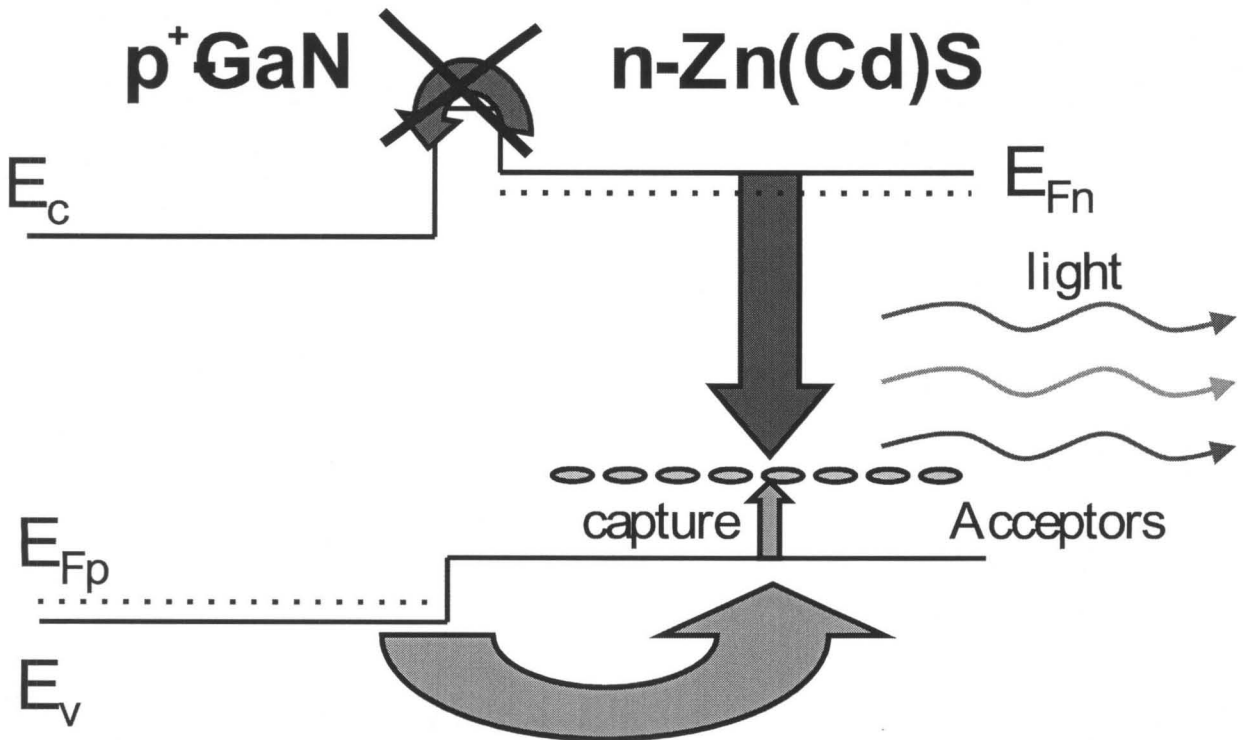


Figure 3.3: Energy band diagram of the p^+ -GaN/n-ZnS LED. Valence band edge of the GaN lies below that of ZnS, therefore allowing efficient injection of holes from p-GaN into n-ZnS, given that device is biased. It is important to have GaN layer strongly doped p-type when compared to n-type doping on ZnS, to achieve that most of the recombination occurs in the n-ZnS layer. In addition, electron blocking layer at the interface can be used to confine electrons in the ZnS layers. If Zn(Cd)S layer is appropriately doped, blue, green and red colors can be obtained.

ZnS. Therefore, the hole transfer across the p^+ -GaN/ZnS interface will be facilitated by this energy difference. The injection efficiency will be approximately improved by a factor of $\exp(E_v/kT)$. Stronger p-type doping of GaN layer when compared to n-type doping of ZnS layer is important, so that most of the recombination occurs in ZnS. Holes injected into ZnS layer will recombine with electrons radiatively and produce luminescence. The wavelength of the emitted light depends on energy levels of intentional impurities in ZnS. However, since the band gap of ZnS is 3.8 eV, that implies difference in conduction band bottoms of $E_c \approx 1.4$ eV in favor of ZnS. This implies loss of electrons from ZnS to GaN layer, and would reduce luminescence intensity. It would be therefore beneficial to diode operation, in addition to the doping requirement, to confine electrons in ZnS layer. This can be accomplished by growing thin layer of ZnMgS at the interface between GaN and ZnS. This layer would act as electron blocker, since large conduction band bottom would confine electrons in ZnS film. More details about simulation of p^+ -GaN/Zn(Cd)S diode can be found in Ref. [10].

3.3 Molecular beam epitaxy growth of ZnS

There have been many reports in the literature of ZnS grown by Molecular Beam Epitaxy (MBE) on a variety of near lattice matched substrates such as Si, [14, 15] GaP [16, 17, 18] and GaAs. [19, 20, 21] The ZnS thin films were grown (by Dr. E.C. Piquette) on GaAs (001), sapphire (0001) and GaN (0001), in an attempt to gain insight into this potentially interesting heterojunctions, and to understand growth on highly mismatched substrates in general. The interfaces between these materials are interesting because of the large lattice mismatch. First, ZnS epilayer will not grow coherently strained for more than one monolayer. During the initial phases of growth, the enormous strain energy related to lattice mismatch will relax and result in formation of numerous dislocations, tilting and 3D relaxation. [22] Second, despite large number of defects, GaN and ZnS are known to be good light emitters. Hence, even though GaN/ZnS interface is expected to be heavily defected, it should provide

us with a potentially useful junction.

More details about ZnS growth procedures can be found in Ref. [23] and [24]. We repeat some details about MBE growth and ultra high vacuum (UHV) *in situ* characterization pertinent for the discussion of optical and structural characterization of these films. ZnS epilayers were grown in a modified Perkin-Elmer 430 Molecular Beam Epitaxy system. This MBE system was equipped with a valved cracking source for sulfur, radio frequency plasma source for nitrogen and Knudsen cell sources for elemental Zn, Al and Ag. The base pressure in a growth chamber during growth was 3×10^{-10} torr. *In situ* reflection high energy electron diffraction (RHEED) operating at 10 keV electron energy was used to structurally characterize samples during growth. Some ZnS films were doped with Ag and Al. Doping with Ag and Al produces films which luminesce in blue region of visible spectrum.

The GaN substrates were 3 μm thick epilayers grown by metalorganic chemical vapor deposition (MOCVD) on c-plane sapphire. Hall measurements performed on these layers indicated a carrier concentration of $\sim 2 \times 10^{17} \text{cm}^{-3}$, and a mobility of $7 \text{ cm}^2/(\text{V}\cdot\text{s})$. Sapphire (0001) substrates were obtained from Union Carbide Crystal Products. GaAs (001) substrates were sourced from American Crystal Technology. Prior to loading into the MBE vacuum system, all substrates were degreased with organic solvents. *In situ* XPS analysis prior to epilayer growth revealed surface contamination by carbon. The carbon contamination could not be completely eliminated by thermal cleaning. However, it was found that it could be removed by exposing the sample to an RF nitrogen soak operating at 200 W at a substrate temperature of 500 °C for approximately 20 minutes. RHEED patterns of the GaN also improved significantly after this treatment. The sapphire substrates were thermally treated at 500 °C for 30 minutes prior to growth, after which sharp streaks in RHEED images were obtained. Etching of substrates did not produce noticeable differences.

Prior to MBE growth, all substrates showed sharp RHEED streaks. After starting the growth of ZnS, the RHEED pattern quickly became spotty for most films, and persisted throughout the growth. The spotty pattern indicates that growth proceeds in the 3D (Volmer-Weber) [25] mode. Crystalline structure of the films corresponded

to surface crystalline structure of the substrate. The ZnS films grown on hexagonal GaN (0001) and sapphire (0001) substrates were of zincblende crystalline structure with (111) orientation, while films grown on GaAs (001) substrates were zincblende with (001) orientation. Most films exhibited mosaic crystallinity with individual crystallites oriented along the (111) axis, but slightly misoriented in the plane of the film. Beside mosaic crystallinity, RHEED studies also indicated that most films grown on sapphire and GaN displayed twinning in the (111) growth plane which is expected for growth on a (111) oriented substrate surface [21]. Films grown at the higher temperature of 400 °C showed no visible twinning and excellent surface morphology, although they suffered from unpractically low growth rates. [23, 24]

3.4 Optical and structural characterization of ZnS thin films

3.4.1 Correlation between structural and optical properties of ZnS

We studied correlation between the structural and optical properties of ZnS films grown on sapphire (0001), GaN (0001) and GaAs (001) substrates. ZnS films were characterized by high resolution X-ray diffraction (HRXRD) and photoluminescence (PL). Details of the HRXRD setup were discussed in Chapter 2. Variable temperature PL data was collected in the home-built setup using a Liconix He-Cd laser, a Janis liquid Helium dewar and a SPEX 1269 spectrometer (see Fig. 3.4). Samples were placed in the Janis dewar where the temperature can be controlled in the range between 4K and room temperature. Sample luminescence was generated by optical excitation using 325 nm line of the He-Cd laser. Luminescence was focused on the entrance slit of the spectrometer, and the dispersed light was collected with Hamamatsu R943 photomultiplier tube (PMT) placed in thermoelectrically cooled PMT housing by Products for Research. A SPEX CD-2B compudrive and PC were used

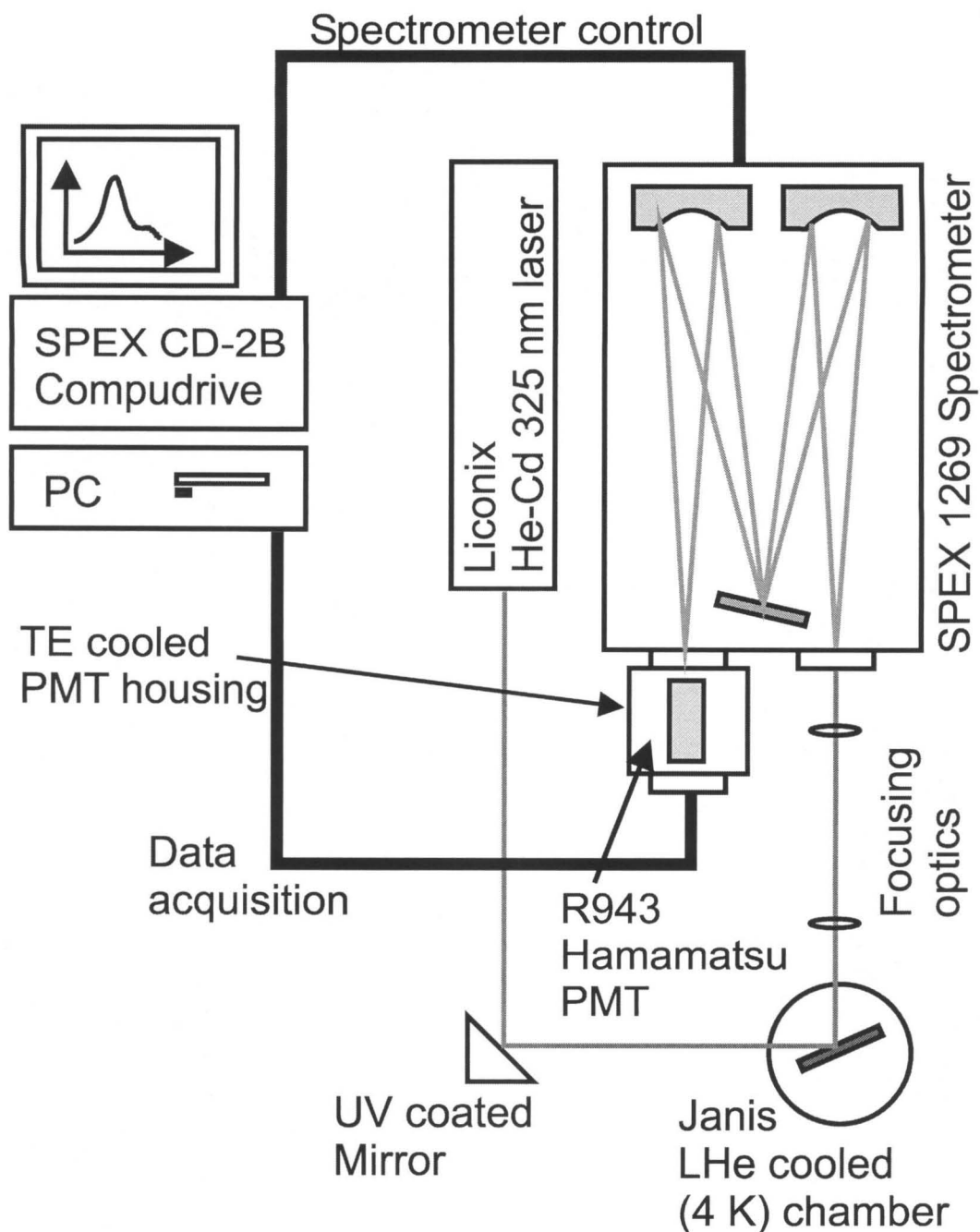


Figure 3.4: PL and EL setup. Sample to be characterized is placed in Janis liquid Helium dewar which can be cooled down to 4 K. In case of PL, samples were excited by Liconix He-Cd laser operating at wavelength of 325 nm. Luminescence is focused to entrance spectrometer slit of SPEX 1269 spectrometer, and output light is analyzed by Hamamatsu R943 photomultiplier tube, placed in Products for Research thermoelectrically (TE) cooled PMT housing. SPEX CD-2B compudrive and PC were used for spectrometer position control and data acquisition. In case of EL, biased samples were placed in front of the entrance slit, and all EL experiments were done at room temperature.

for controlling the spectrometer position and data acquisition.

Room temperature PL scans of ZnS films grown on sapphire (0001), GaAs (001) and GaN (0001) substrates are shown in Fig. 3.5a. Samples were doped with Al and Ag and grown under identical conditions in the same growth run (II411), but different substrates were used. All samples produced bright blue luminescence centered around 450 nm, which is the line characteristic for silver “activator” low (440-450 nm) emission band. [26] The laser excitation power density was estimated as 2.5 mW/cm² from the focused spot size and the measured output power of the laser beam. We can notice from Fig. 3.5a that ZnS grown on GaN has the smallest luminescence intensity. The optical quality of the films clearly corresponded to the structural quality, as can be observed from Fig. 3.5b, which shows X-ray rocking curves for the same set of samples. ZnS film grown on GaN, which had the smallest luminescence, displayed the smallest peak intensity and the largest full width at the half maximum (FWHM) of the X-ray rocking curve, indicating highest degree of the misorientation (mosaicity) in the film (see Fig. 3.6). The correlation between optical and structural properties can perhaps be best observed from Fig. 3.7, which directly compares integrated photoluminescence (over the measured wavelength range) and FWHM’s of the X-ray rocking curves. Clearly, films with wider FWHM of the X-ray rocking curve, and therefore larger mosaicity and lower structural quality, also had smaller integrated luminescence. It is interesting to observe that although the absolute values of lattice mismatch for GaN and sapphire substrates are similar ($\approx 20\%$), the ZnS films grown on sapphire have better optical and structural properties. Unlike the GaN surface, where possible obstruction of the ZnS film growth by chemical reaction between Ga and S might occur (and therefore growth of GaS_x), the surface of sapphire is very chemically stable. At the time of this study, effects of the polarity of the GaN surfaces (Ga- versus N-face) were not well known and studied, and only MOCVD-grown films were used. [27] It is possible that MBE grown GaN (which typically has opposite polarity than MOCVD grown GaN) would be more susceptible for the ZnS growth. It is important to notice that the luminescence of the ZnS film grown on GaN substrate, although smaller when compared to films grown on GaAs and sapphire, is still bright

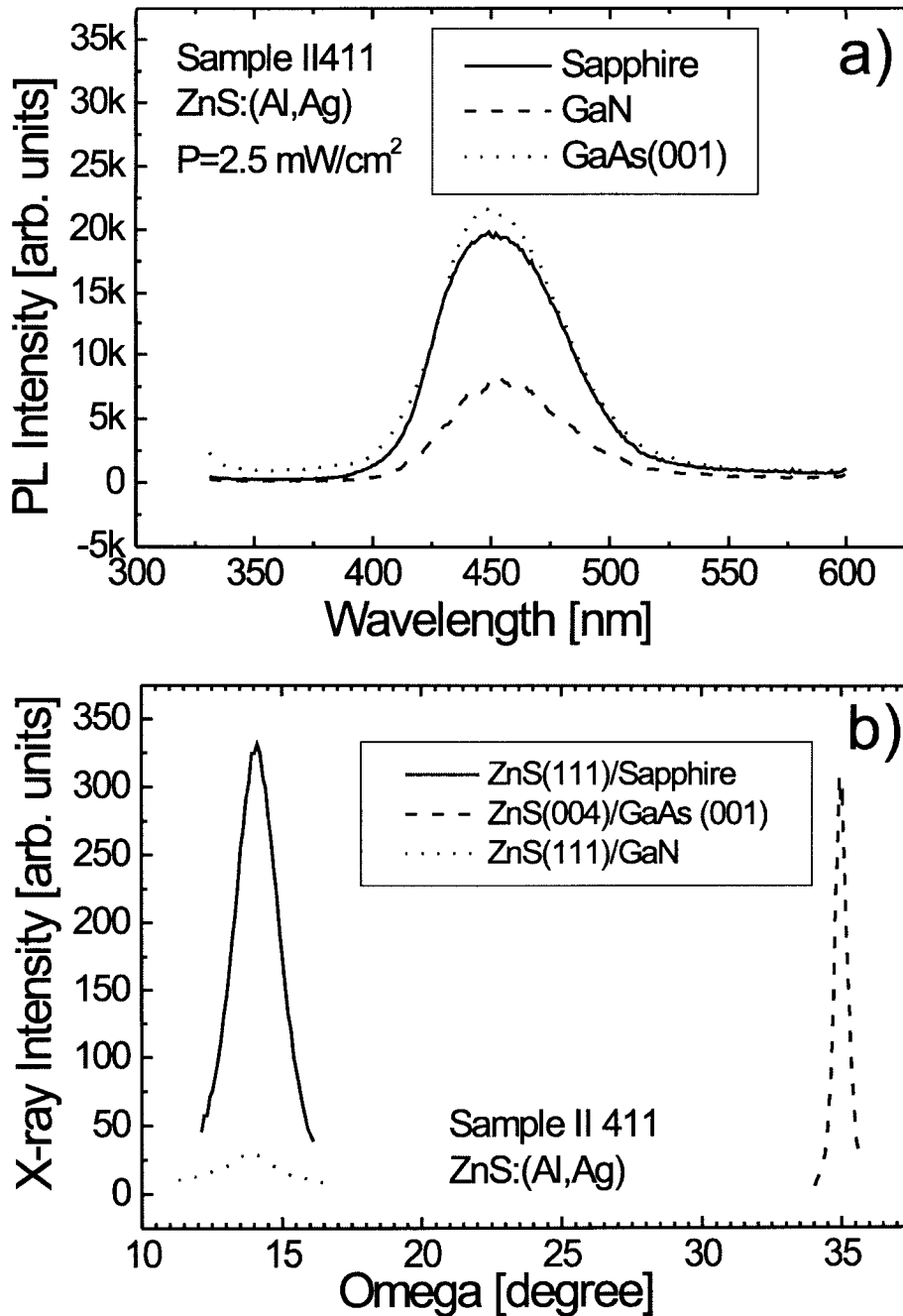


Figure 3.5: a) Room temperature PL scan of ZnS film (sample series II 411) grown on sapphire, GaAs and GaN substrates. All samples are doped with Al and Ag and grown under nominally identical conditions. All PL peaks are centered around 450 nm, but of different intensity, indicating varying optical quality. b) HR-XRD scans of same sample series. The intensity and FWHM of X-ray curves is related to the crystalline quality of the films.

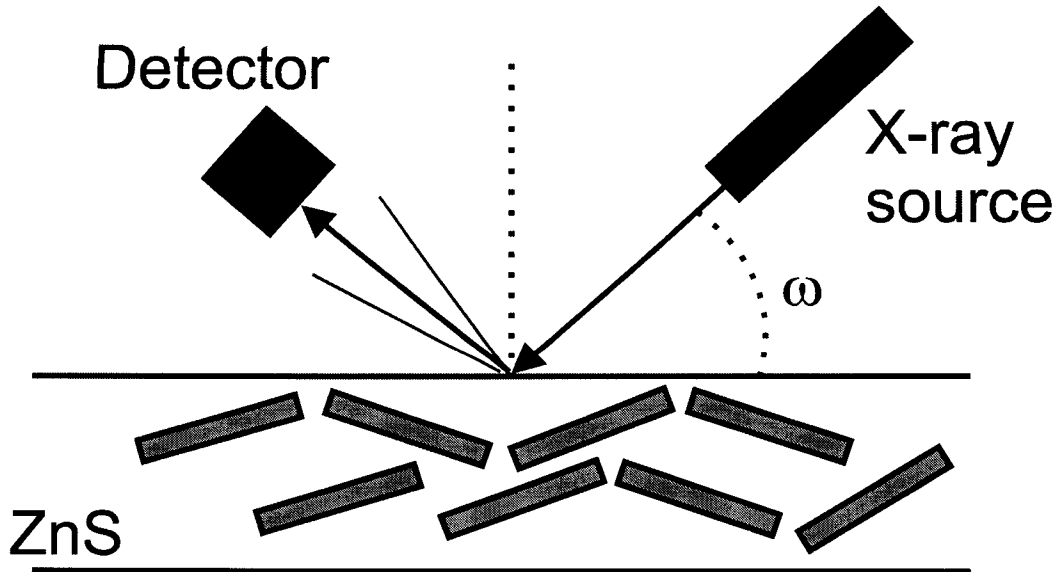


Figure 3.6: The mosaic structure of the films is caused by relaxation of strain energy in the initial phases of growth. The mosaicity, or the level of the crystallite misorientation in the film can be characterized by the broadening (FWHM) of the Ω X-ray rocking curve.

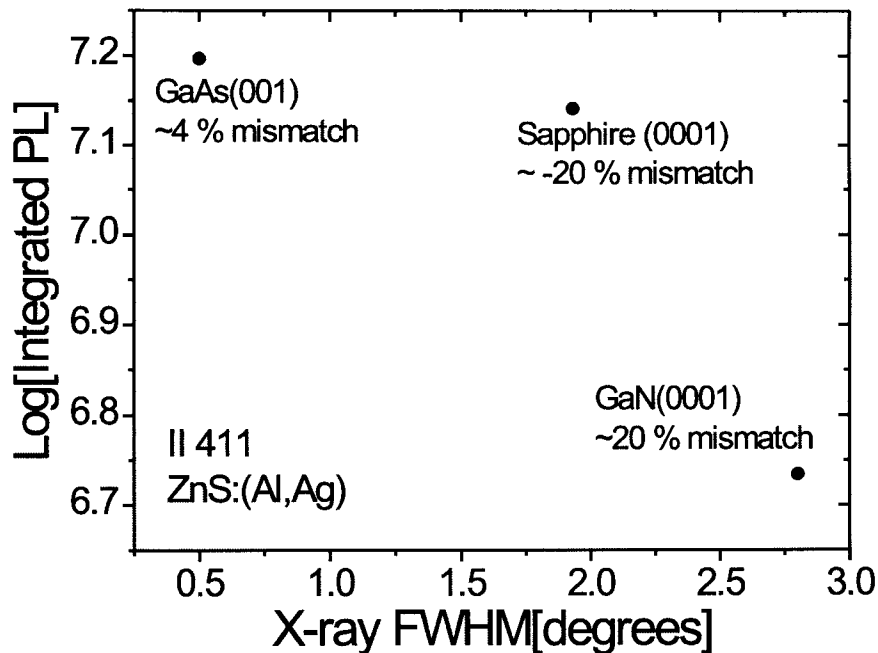


Figure 3.7: Integrated room temperature PL as a function of FWHM of X-ray rocking curves for ZnS thin films grown on GaAs, sapphire and GaN. Optical quality of the samples (defined as integrated PL) directly depends on structural quality (defined by FWHM of X-ray rocking curve). Although sapphire and GaN have similar absolute value of lattice mismatch, properties of ZnS films grown on sapphire are better.

enough to be easily observable by eye in the laboratory with the light on.

3.4.2 Low temperature PL study of ZnS grown on GaN substrates

Since ZnS films for practical LED's have to be grown on GaN substrates, we studied low temperature PL of the ZnS grown on GaN substrates and compared them to the ZnS films grown on sapphire. Low temperature (5 K) PL scans of ZnS samples doped with Al and Ag and grown on p-type GaN, n-type GaN and sapphire substrates are shown in Fig. 3.8 a), b) and c) respectively. All samples produced bright blue luminescence. Visible are two characteristic silver activator bands: silver high (390 nm) and silver low (440 nm). [26] The preparation of the sample, especially the relative amounts of Al and Ag, are known to influence relative intensities of these two bands. [26] In the samples studied, both bands are present for the ZnS:(Al,Ag) films grown on sapphire (Fig. 3.8c), while the lower energy band dominates for the films grown on n-type GaN (Fig. 3.8b). Films grown on p-type GaN show emission predominantly near the high energy (390 nm) band (Fig. 3.8a). In the case of ZnS films grown on GaN, it is not possible to avoid GaN substrate luminescence. For example, the p-type GaN has luminescence in blue-violet region which overlaps with the high energy (390 nm) silver band. Also, in the (Fig. 3.8b) we can observe phonon replicas (370-400 nm) of the eA (conduction band to deep acceptor) transition of the GaN.

3.5 Electroluminescence of ZnS/GaN LED's

3.5.1 Device fabrication

Standard photolithographic procedures were used to fabricate p-GaN/n-ZnS:(Al,Ag) LED devices. The schematic of the structure is shown in Fig. 3.9. Since sapphire is a non-conductive substrate, all contacts were deposited on the top of the structure (see Fig. 3.9). Following cleaning, aluminum contacts were sputtered on top ZnS:(Al,Ag)

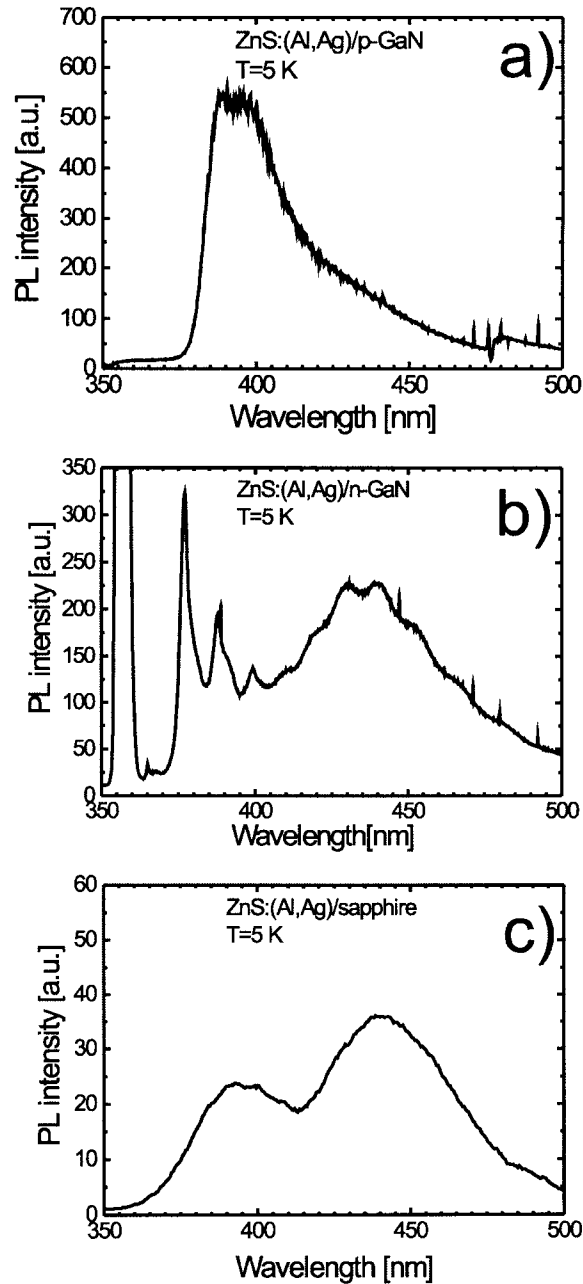


Figure 3.8: Low temperature ($T = 5$ K) PL scans of n-type ZnS doped with Al and Ag on a) p-type GaN substrate, b) unintentionally doped n-type GaN substrate, and c) sapphire substrate.

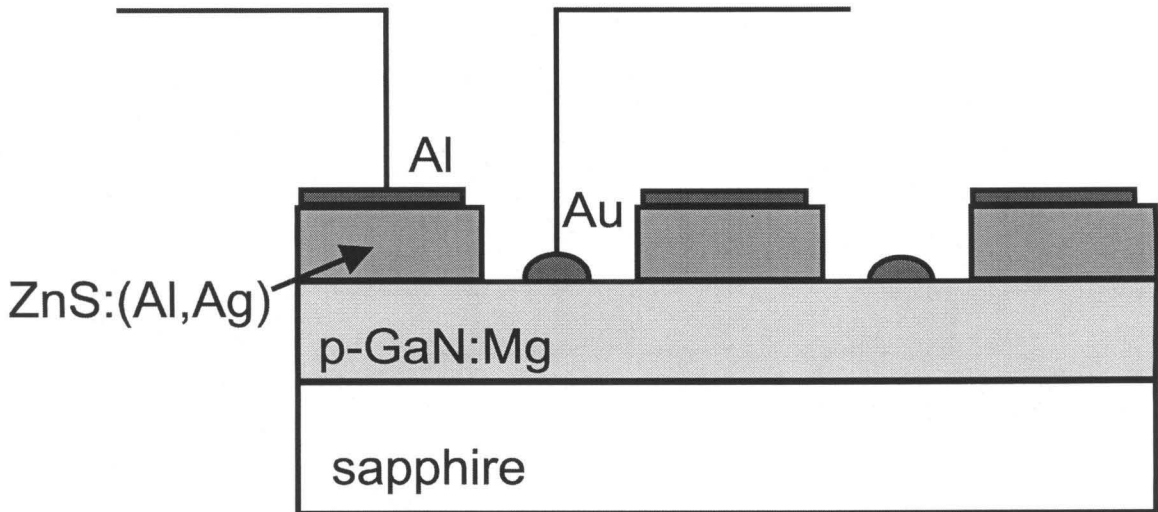


Figure 3.9: Schematic of the fabricated ZnS/p-GaN LED. Aluminum and gold were used as ohmic contacts for n-ZnS and p-GaN layers respectively.

layers in a chamber with a background pressure of $2 \cdot 10^{-8}$ Torr. Aluminum contacts were thin enough to allow light transmission. Ideally, the back-side of the sapphire (if polished) could also be used for light extraction. Following sputtering, Al/ZnS mesas were produced by etching in Br:HBr:H₂O (1:100:100) solution, which does not react chemically with the GaN surface. Gold contacts were then sputtered, patterned by lift-off, and annealed at 780 °C to reduce the rectifying nature of contacts. Contacts were found to be rectifying as deposited, and ohmic contacts to the ZnS were found to be quite challenging to produce.

The current-voltage characteristic of the resulting n-ZnS/p-GaN LED is shown in Fig. 3.10. It is evident that the turn-on voltage is approximately 3 V, which is expected because it corresponds to the bandgaps of both ZnS and GaN less the interface band offset. The large series resistance of the device is consequence of both the low conductivity of GaN and the lack of conductive substrate to provide a back ohmic contact.

LED devices were mounted on die package and wire bonded. The electroluminescence from biased devices was then focused on the entrance slit of the spectrometer and dispersed using setup described in Fig. 3.4. The EL scan as a function of device bias is shown in Fig. 3.11a. The luminescence was bright enough during room tem-

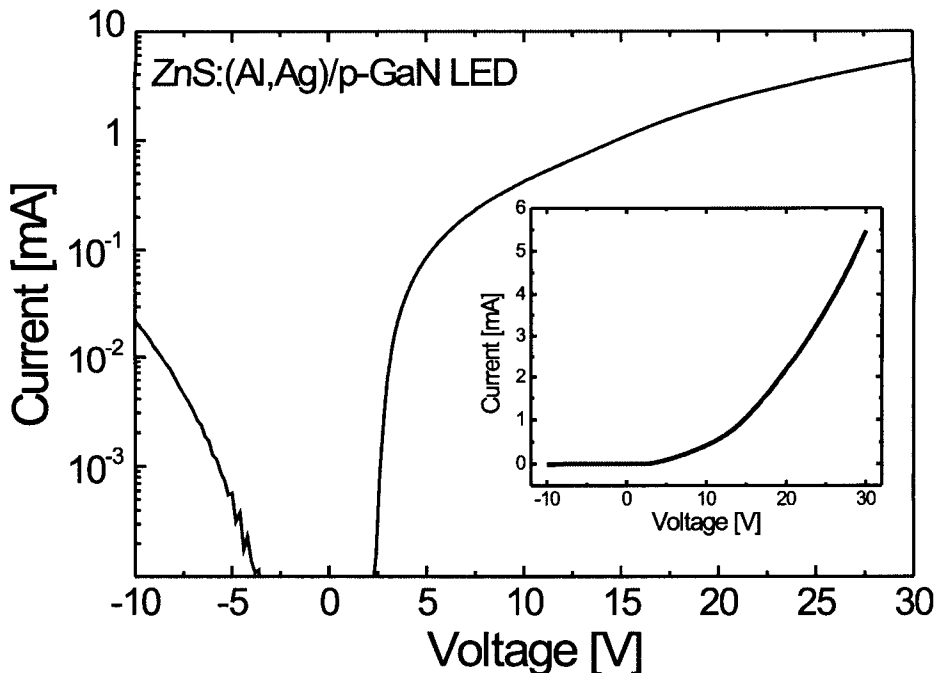


Figure 3.10: Current-voltage characteristics of ZnS:(Al,Ag)/p-GaN diode on the logarithmic-linear scale. The turn-on voltage is approximately ≈ 3 V. Inset shows same characteristics at linear-linear scale.

perature operation to be observable to the eye. At low applied voltages between 3 to 10 V, luminescence is centered around 390-400 nm. At higher voltages between 10 to 25 V the luminescence shifts to higher energies and is centered around 385-390 nm. We have also observed luminescence non-uniformity and “bright-spots,” which might be expected due to current spreading and structural defects.

It is non-trivial to exactly analyze the luminescence mechanism since broad PL spectra of both p-type GaN:Mg and n-ZnS:(Al,Ag) have peaks centered around 390 nm (see Fig. 3.8). Since these preliminary devices did not include an electron blocking layer at the ZnS/GaN interface, it is possible that electrons injected from n-ZnS into p-GaN recombine with holes, and produce luminescence typical for p-GaN. Also, radiative recombination in either layer may be followed by absorption and fluorescence in the other layer. We can also observe from Fig. 3.11 that integrated electroluminescence saturates at large voltage biases above 15 V.

Some of the practical problems in the fabrication of the LED were poor ohmic contacts to n-type ZnS, lack of conductive GaN substrate and relatively unsatisfactory

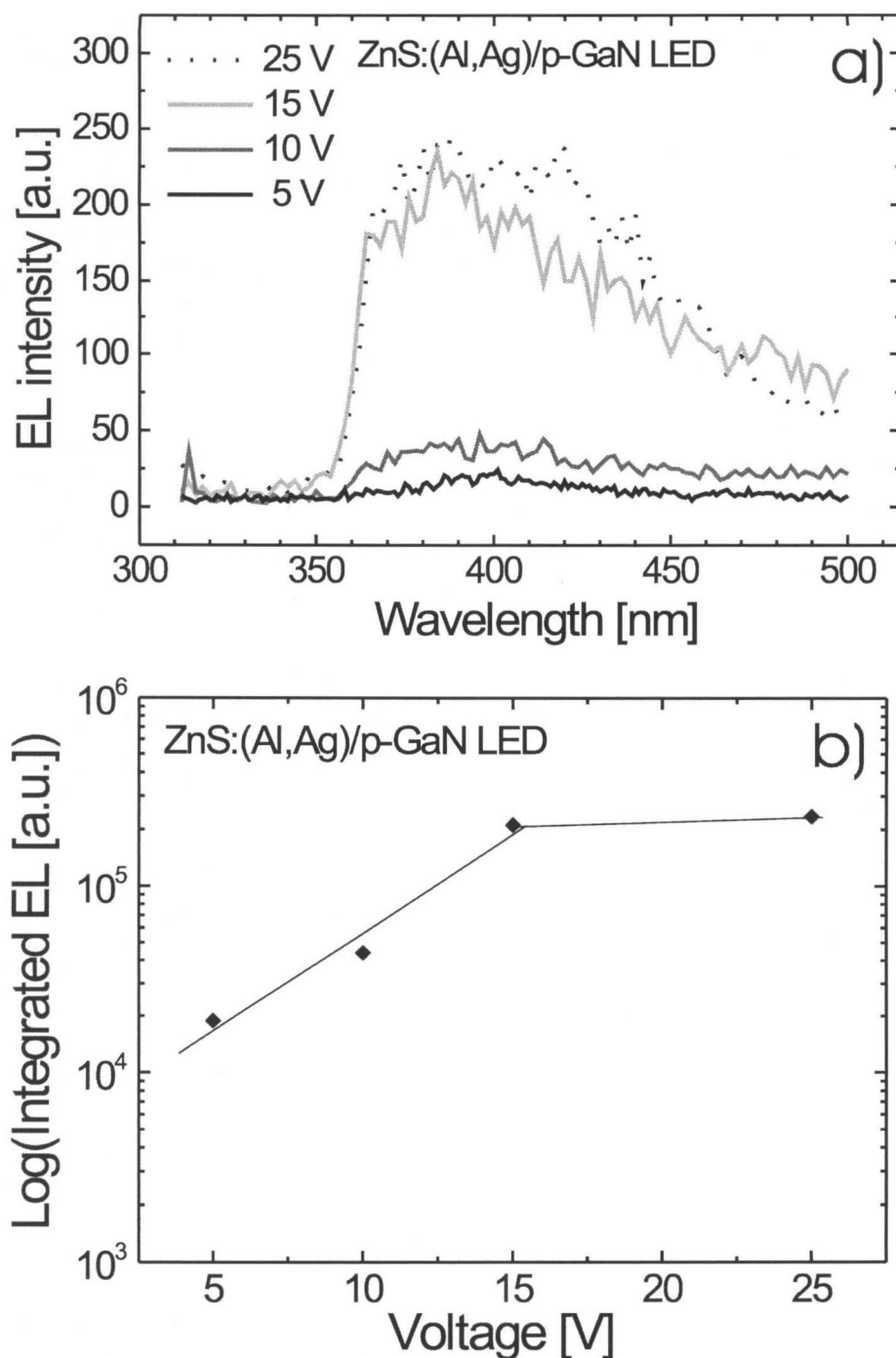


Figure 3.11: a) Room temperature EL as a function of device bias. EL emission is centered around 385-400 nm, depending on bias voltage with width of luminescence peak varying from 45 nm (at 5 V), to approximately 90-110 nm (at 10 V and above). b) Integrated EL emission intensity as a function of device bias. We can notice saturation at ≈ 15 V.

crystalline quality of ZnS layers. Since the luminescence properties were correlated to the crystalline properties (mosaicity), an attempt has been made to improve structural properties of the ZnS layers by post-growth treatments. One such attempt, the high pressure solid phase recrystallization, is described in the next section.

3.6 High pressure solid phase recrystallization of ZnS thin films

It was described in the section 3.3 that the initial phases of growth in the heavily mismatched interface geometry, such as growth of ZnS on sapphire or GaN, are the most critical, and it is not expected that the ZnS epilayer would grow coherently strained for more than 1 epilayer. In fact, the large mismatch-related energy will be relaxed in the form of tilting and three-dimensional relaxation (see Fig. 3.6). [24, 22] This would certainly damage the overall crystalline quality of the ZnS layer, which is known to be important to the performance of the II-VI - based optical devices, [28] as seen in section 3.4.1. It is therefore of significant interest to develop post-growth techniques which can improve crystalline properties of the ZnS films grown on heavily mismatched substrates.

In this section we discuss the solid phase recrystallization (SPR) of undoped, 0.3–0.5 μm -thick, molecular beam epitaxy (MBE) grown, (111)-oriented, cubic ZnS films on sapphire ($\sim 20\%$ mismatch). [29] These samples were recrystallized by annealing at temperatures in the 825–1000 $^{\circ}\text{C}$ range, and sulfur pressures of 10 atm. Details about the MBE ZnS growth system and procedures were given in section 3.3. Thermal annealing at large sulfur overpressure consistently improved the structural properties of the films, thereby compensating the effects of strong mismatch. Some of the previous efforts on recrystallization of thin films are described in the Ref. [26]. Presently, recrystallization is an important industrial process, and plays a vital role in the manufacture of steel and aluminum, [30] and HgCdTe. [31] Solid phase recrystallization of bulk ZnSe, CdTe and CdSe was recently successfully demonstrated

by Triboulet *et al.*, [32, 33] by annealing at the high temperatures under high column VI element overpressure, and excellent optical and structural properties were obtained. [34]

3.6.1 Experimental details

To contain ZnS samples and sulfur during the experiment, quartz ampoules with 2mm-thick walls were used. Prior to the experiment, the ampoules were cleaned with organic solvents (acetone and isopropyl alcohol) and then baked at 1000 °C for 2-4 hours. The MBE-grown undoped ZnS/Sapphire films were placed in the ampoules together with 100–200 mg of 99.9999% Sulfur. The amount of sulfur placed in the ampoule was calculated according to the van der Waals equation of state, so that gas pressure of 10 atm is reached on the anneal temperature. The ampoules were then attached to a turbo-molecular pump to attain a vacuum of $1 \cdot 10^{-6}$ Torr, and then sealed while the pump was still running (see Fig. 3.12). The sealed ampoules were then transferred into the temperature-controlled furnace. The temperature was slowly increased at the rate of 2–3 °C/min to avoid thermal strains, until the final temperature in the 825–1000 °C range was achieved. After the samples were kept at this temperature for 2–20 hours, the temperature was slowly reduced at the rate of 2–3 °C/min, again to avoid thermal stressing.

3.6.2 Structural characterization

High resolution X-ray diffraction

Samples were characterized before and after the annealing by *ex-situ* high resolution X-ray diffraction (HRXRD), using commercial Philips Materials Research Diffractometer, described in Chapter 2. The Ω and $\Omega/2\Theta$ scans around the ZnS thin film (111) reflections were performed in the 4 or 6-crystal mode (without or with Bonse-Hart collimator in front of the detector) respectively, using Ge(220) reflections.

To characterize the effects of different anneal temperatures, one sample (II391) was cut into 5 pieces, and each of them was annealed at different temperature be-

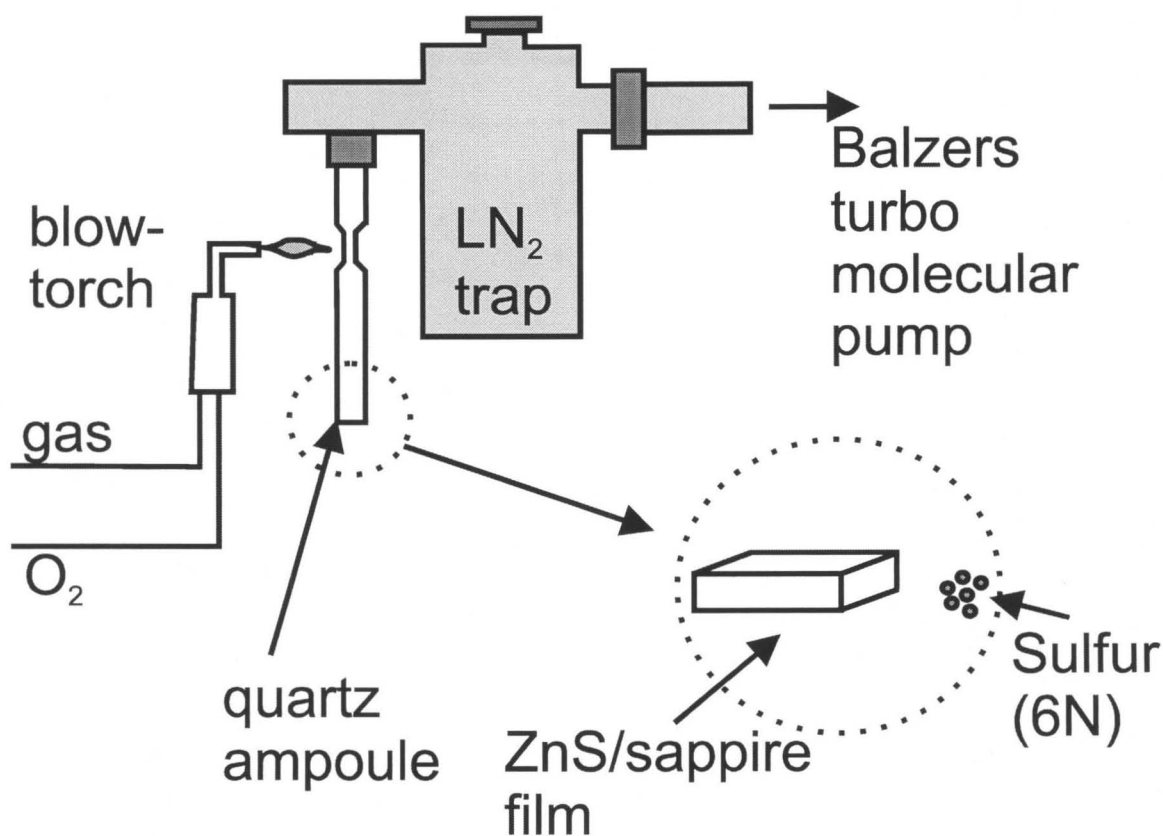


Figure 3.12: Schematics of the experimental setup used to vacuum-seal quartz ampoules containing ZnS thin films and sulfur. The ZnS and sulfur were placed in cleaned and baked ampoules, and ampoules were attached to the Balzers turbo-molecular pump through liquid nitrogen trap. Liquid nitrogen trap was used to prevent streaming of sulfur into turbo pump. The air was evacuated to attain vacuum level of $1 \cdot 10^{-6}$ Torr. The ampoules were then sealed while the pump was still running.

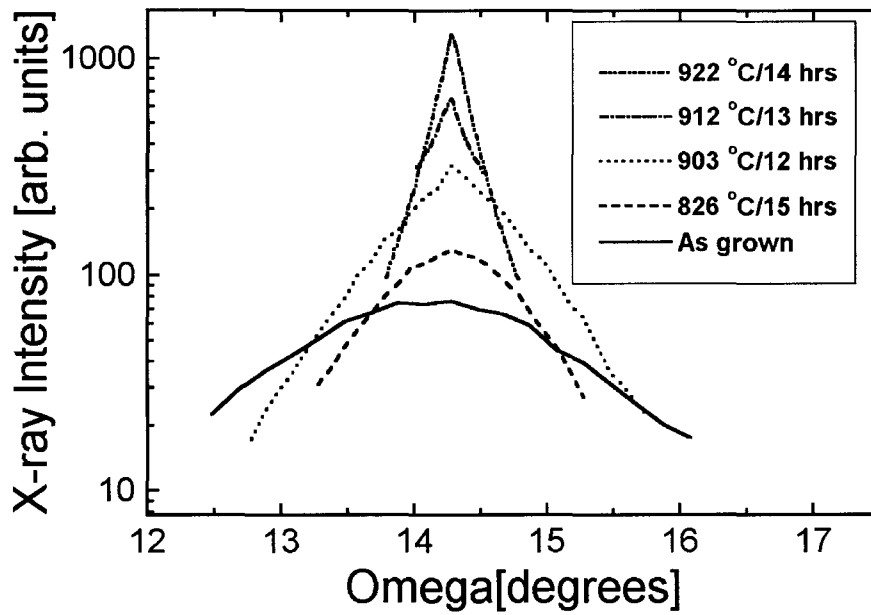


Figure 3.13: Summary of X-ray Ω -scans for different recrystallization temperatures of sample II391. The curves for samples recrystallized at higher temperatures have lower widths and higher maximum intensity.

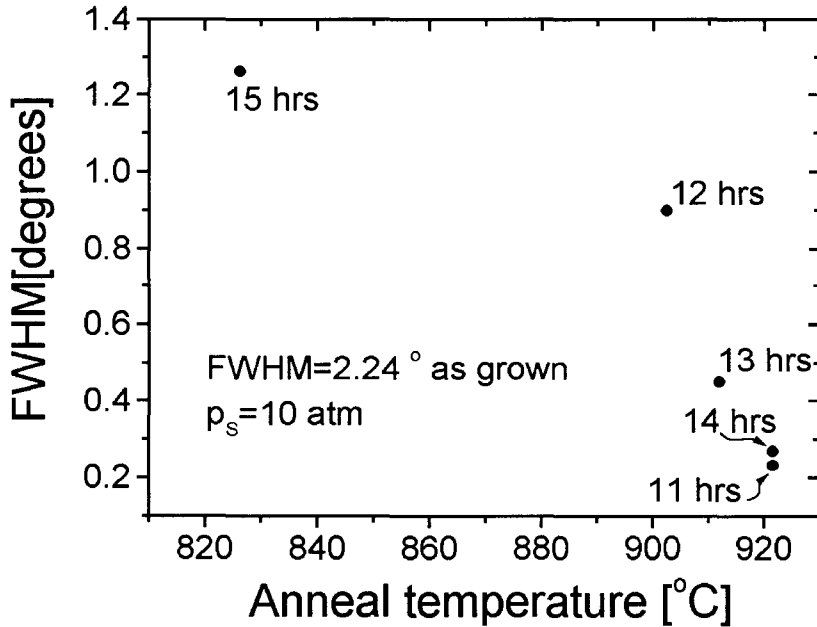


Figure 3.14: Summary of FWHM's of X-ray Ω -scans for different recrystallization temperatures of sample II391.

tween 825°C and 922°C. The anneal temperature has to be chosen below the melting temperature, but has to be high enough so that the original grain boundaries become unstable. At that point, the conditions are favorable for the migration of grain boundaries and growth of defect-free nuclei. The anneal time ranged between 11 and 15 hours, and sulfur overpressure was kept constant at 10 atm. The X-ray Ω -scans (Fig. 3.13), and the full width of the half maximum (FWHM) of the curves as a function of temperature (Fig. 3.14), indicate the amount of mosaic tilting present in the films, [35] and show that the crystalline mosaicity is significantly reduced at anneal temperatures above 900°C. As grown samples exhibited mosaic structure with grains approximately 10 μm or less in size. Following recrystallization, the degree of mosaic tilting reduced approximately an order of magnitude, while the size of mutually tilted grains increased to approximately 130 μm or less. However, the overall crystalline orientation was preserved across the grain boundaries, which was verified by X-ray diffraction on the asymmetric set of crystalline planes. The typical

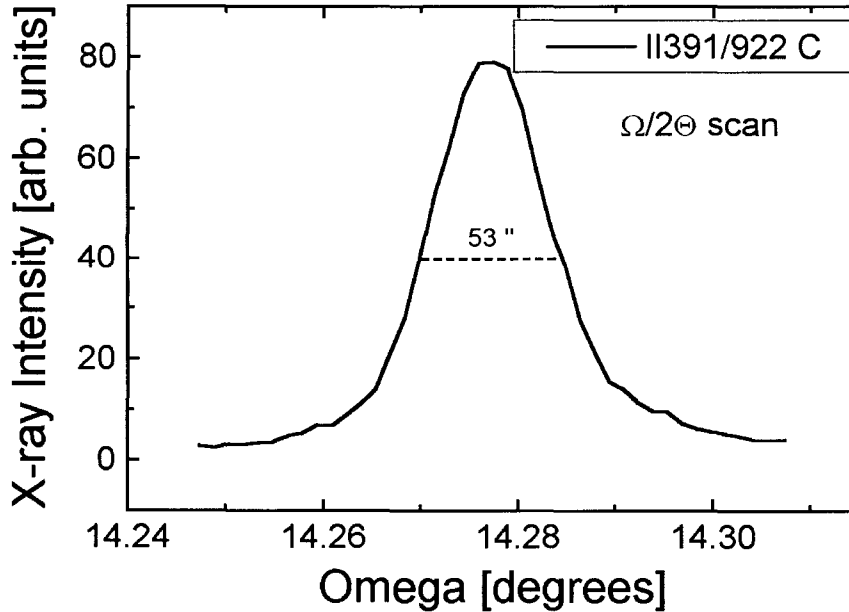


Figure 3.15: The $\Omega/2\Theta$ -scan of the sample II391 after recrystallization process. The anneal temperature was 922 °C and the sulfur overpressure 10 atm.

FWHM of $\Omega/2\Theta$ curves for the samples in the II391 series after recrystallization was around 50", (see Fig. 3.15) measured in the 6-crystal configuration (using Bonse-Hart monochromator with 12" acceptance angle in front of the detector-see Fig. 2.2 in Chapter 2).

It was not possible to use this particular configuration before recrystallization, because the quality of the crystal was not good enough. Measured with the 4-crystal configuration, the typical width before recrystallization was around 270" (450" was typically measured, but there is a correction of 180" for the slit width). The width of the $\Omega/2\Theta$ scan corresponds to the crystalline quality of the individual grains, and in the case of the symmetrical reflection (like (111)) it depends on the thickness L of the sample approximately as $\sim 0.886\lambda/(\cos\theta L) \sim 29"/L[\mu\text{m}]$. [36] Since the thickness of the sample II391 was 0.45 μm , the width of 50" corresponds to recrystallized, defect-free grains. The set of Ω and $\Omega/2\Theta$ X-ray rocking curves of the sample II366 before and after recrystallization is shown in Fig. 3.16. The anneal temperature was 970 °C

and sulfur overpressure 10 atm. Tenfold improvement in crystalline quality can be observed.

Scanning electron microscopy: electron channeling

Electron channeling patterns (ECP) are an interesting example of the electron diffraction which can be obtained in scanning electron microscopy, and are analogous to more commonly known Kikuchi patterns, which are electron diffraction patterns obtained in transmission electron microscope. The basic principles for formation of ECP are laid out in Fig. 3.17. When an electron beam is incident on a crystalline sample (see Fig. 3.17a), the beam incident to a particular set of lattice planes with an angle slightly smaller than the Bragg angle θ_H (beam 1 on Fig. 3.17a) will backscatter from the sample. The beam with an angle slightly larger than the Bragg angle (beam 2 on Fig. 3.17a) will penetrate into the sample. [37] Since the backscattered electron intensity is proportional to the degree of inelastic scattering, the intensity of backscattered electrons changes at the Bragg angle $\pm\theta_H$ (see Fig. 3.17b). This change at Bragg angle results in line contrast corresponding to a particular set of lattice planes, when the beam is angle-scanned in two orthogonal directions. Each pair of lines in Fig. 3.17c corresponds to the set of lattice planes having various spacings. Electron channeling patterns (ECP) were obtained in a JEOL 6400V scanning electron microscope (SEM). The pattern for sample II366, recrystallized at 970 °C for 3 hours at sulfur pressure of 10 atm, is shown in Fig. 3.18. The corresponding Ω and $\Omega/2\Theta$ scans, before and after recrystallization, are shown in Fig. 3.16.

It was not possible to obtain visible ECP's for samples before they were recrystallized, probably due to tilting and large number of defects. In Fig. 3.18 we can notice fine structure, where each line corresponds to the set of crystalline planes reflecting or absorbing high energy electrons. The high level of detail on this image corresponds to good crystallinity, in agreement with the X-ray measurements. The pattern has 3-fold symmetry, indicating that the sample is indeed cubic, and that no phase transition to the hexagonal crystal modification (which would have 6-fold symmetry) occurred.

The changes in surface morphology of the recrystallized samples have been in-

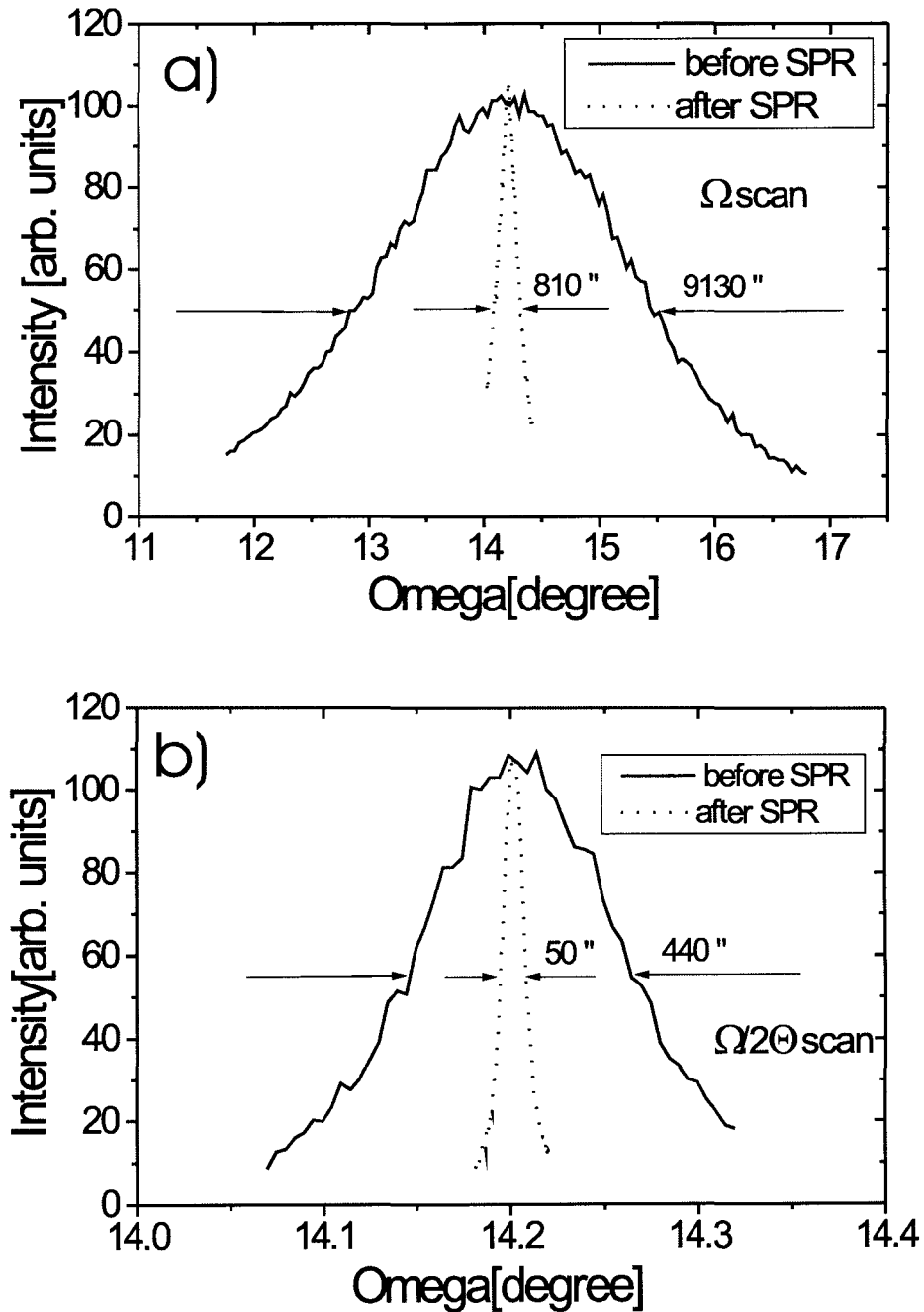


Figure 3.16: The Ω and $\Omega/2\Theta$ -scan X-ray curves of the sample II366 before and after recrystallization process. The anneal temperature was 970°C and the sulfur overpressure 10 atm. The maximum intensities of the curves in the case of the recrystallized sample have been reduced to the maximum intensity of the initial curve, so that curve widths can be compared.

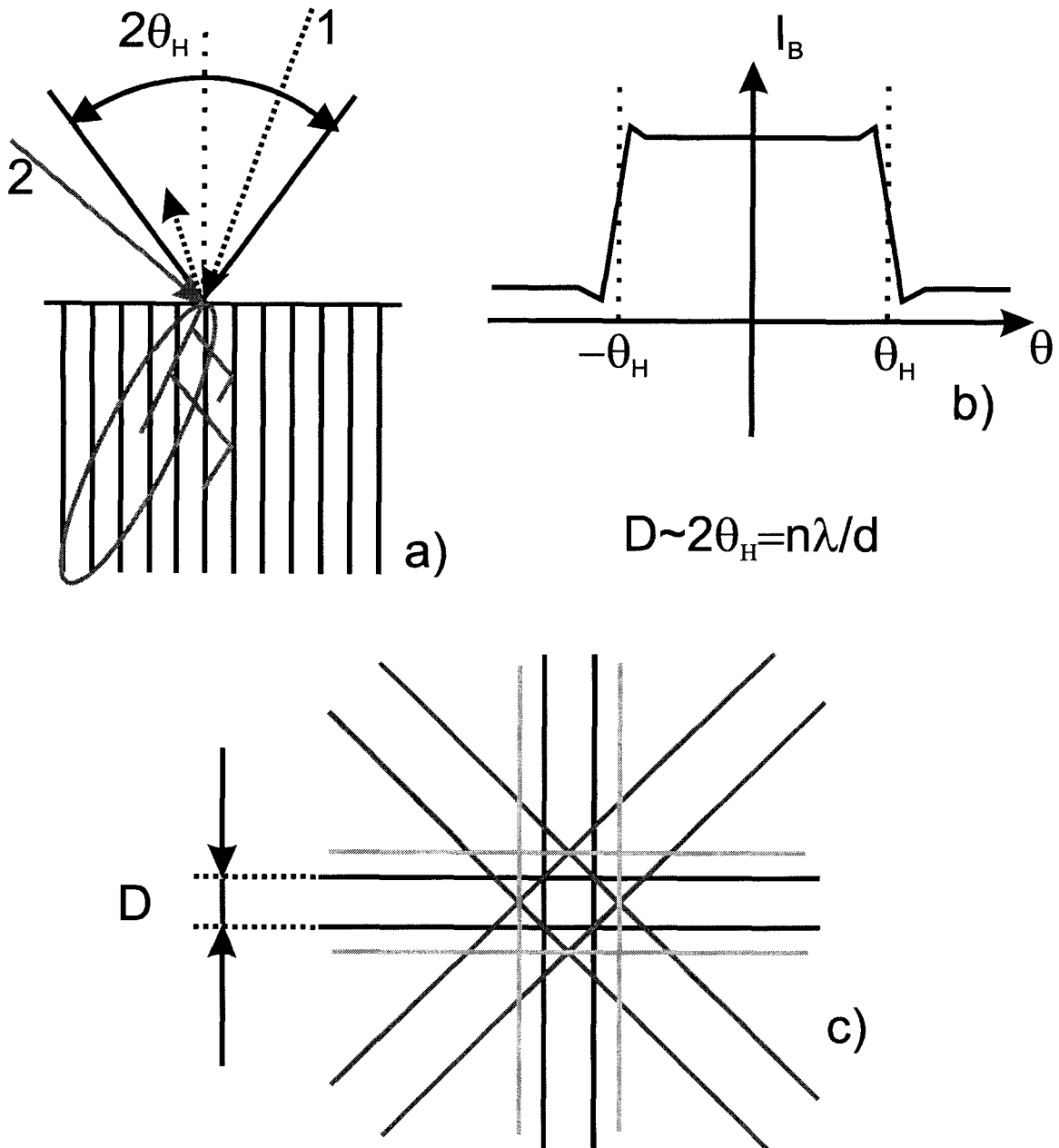


Figure 3.17: a) When an electron beam is incident on a crystalline sample, the beam incident to a particular set of lattice planes with an angle slightly smaller than the Bragg angle θ_H (beam 1) will backscatter from the sample, while the beam with an angle slightly larger than the Bragg angle (beam 2) will penetrate into the sample. b) Since the backscattered electron intensity is proportional to the degree of inelastic scattering, the intensity of backscattered electrons changes at the Bragg angle $\pm\theta_H$. c) This results in line contrast corresponding to a particular set of lattice planes, when the beam is angle-scanned in two orthogonal directions. Each pair of lines corresponds to the set of lattice planes having various spacings.

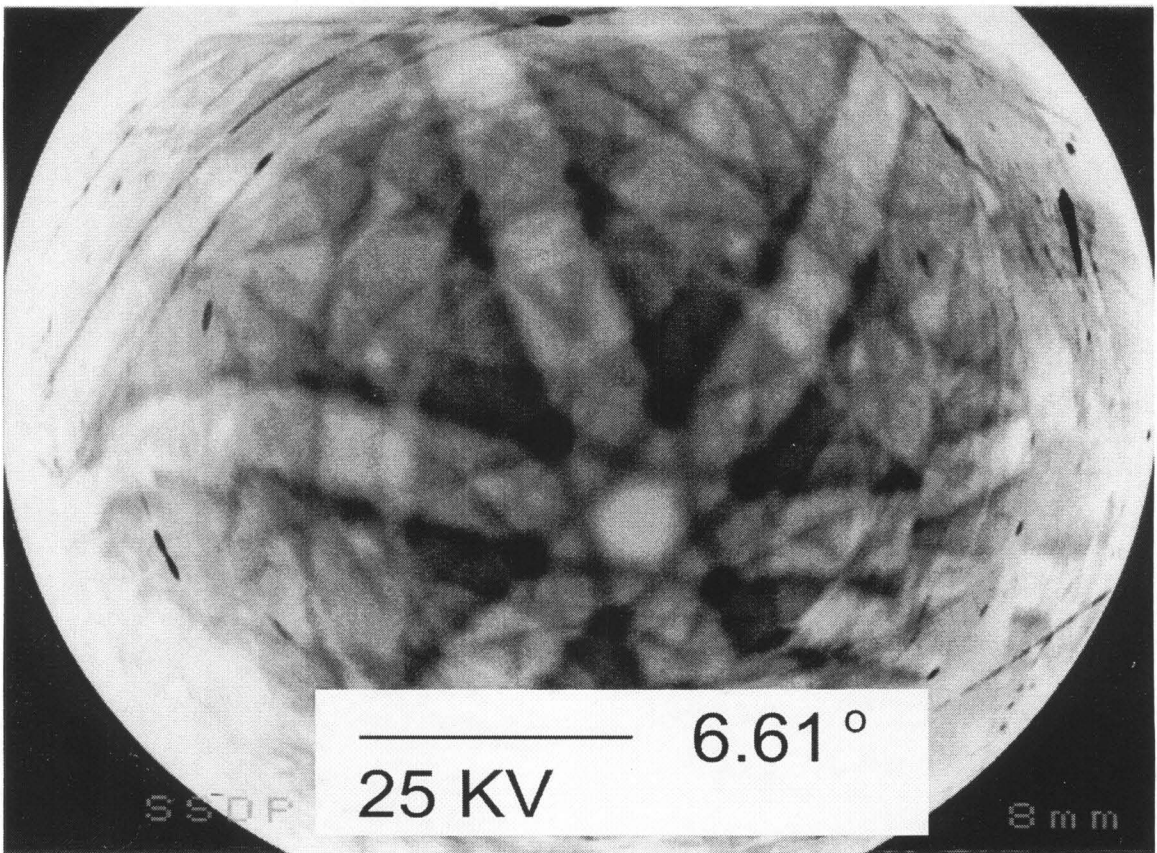


Figure 3.18: Electron channeling pattern of the sample II366, recrystallized at 970°C for 3 hours at sulfur pressure of 10 atm. The 3-fold symmetry of the pattern indicates cubic crystalline lattice and that no phase transition occurred. The fine structure in the pattern confirms good crystallinity of the sample.

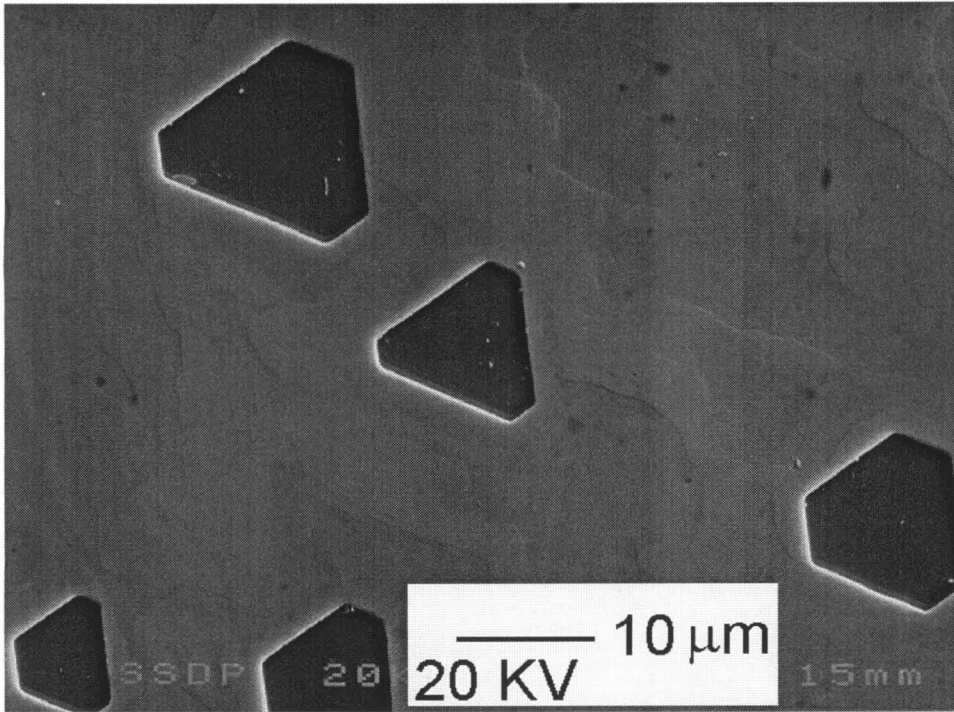


Figure 3.19: Surface of the sample II391 recrystallized at 922 °C. The change in the surface morphology in form of hexagonal pits can be observed.

investigated with the SEM. On most of the samples, the surface morphology after recrystallization remained smooth, which is important for device-related reasons, like electrical contacting. However, on some samples recrystallized at higher temperatures we observed hexagonal pits (see Fig. 3.19). One possible reason for the formation of pits at higher recrystallization temperatures is excess crystalline volume associated with large density of defects. During the recrystallization process and boundary migration, the annihilation of defects takes place, during which volume of the crystal reduces resulting in the pit formation. At lower temperatures, however, the boundary migration is slower and crystal relaxation times larger, which leads to fewer or no pits formed.

3.6.3 The role of sulfur

The role of the sulfur gas overpressure is manifold. First, the high sulfur overpressure greatly reduces zinc partial pressure, and thus prevents the evaporation of the ZnS

film. Second, the sulfur-rich stoichiometry produces grain boundaries enriched by fast diffusing sulfur, which helps grain boundary migration. The large solubility of the chalcogen in the chalcogenides was accounted for to explain the result that bulk ZnSe recrystallization cannot be achieved under zinc overpressure. [32] In addition, we hypothesize that sulfur might also play an important role at the ZnS/sapphire interface. The significant difference between recrystallization of thin films and bulk, is the large mismatch-related energy accumulated at the interface, which should reduce grain boundary mobilities. One possible route for the relaxation of this energy is a sulfur-rich ZnS/sapphire interface. Sulfur-terminated sapphire surface might change into "quasi van der Waals" one, similar to selenium-terminated GaAs surface. [38] Weaker interface bonding could change interface structure, assist boundary migration and provide compliancy to the sapphire substrate.

3.7 Conclusion

Zinc sulfide/Galium nitride heterostructures are potentially interesting system for light emitters in blue and green part of visible spectrum. One attractive application of this diodes would be low power consumption DC electroluminescent displays.

Zinc sulfide thin films grown on GaN (0001), GaAs (001) and sapphire (0001) substrates by MBE were characterized by variable temperature photoluminescence and high resolution X-ray diffraction. It was found that structural properties of ZnS films grown on sapphire and GaN suffered from heavy lattice mismatch. The optical properties of the ZnS films, characterized by integrated photoluminescence intensity over the measured wavelength range, were found to be in correlation with structural properties of the films, characterized by FWHM of X-ray rocking curves.

The ZnS films grown on n- and p-type GaN were characterized by low temperature photoluminescence and compared to the ZnS films grown on sapphire. All samples displayed bright blue luminescence with two characteristic silver activator bands at 390 nm and 440 nm. N-ZnS/p-GaN heterostructures were fabricated and characterized by current-voltage and electroluminescence. Electroluminescence was found to

be centered around 390 nm, corresponding to high energy silver band, and it shifted to higher energies with increase in device voltage.

Since as grown films suffered from crystalline imperfections, the ZnS thin films on sapphire were recrystallized, by annealing at temperatures above 900 °C at sulfur overpressure of 10 atm. The structural properties of samples, quantified in terms of widths of X-ray Ω and $\Omega/2\Theta$ scans, significantly improved, indicating more than 10-fold reduction in tilting and excellent crystallinity. The electron channeling patterns confirmed good structural quality of the films. Surfaces of most recrystallized samples remained smooth, which is important for device-related applications. On some samples recrystallized at elevated temperatures the formation of hexagonal pits was observed and associated with the annihilation of large number of defects initially occupying excess crystalline volume. The role of sulfur was discussed, and it was found that sulfur is important in preventing film evaporation, increasing boundary migration and providing compliancy to sapphire substrate.

Bibliography

- [1] S. Yamaga, *Physica B* **185**, 500 (1993).
- [2] T. Yokogawa and T. Narusawa, *Appl. Phys. Lett.* **61**, 291 (1992).
- [3] J.M. Depuydt, M.A. Haase, S. Guha, J. Qiu, H. Cheng, B.J. Wu, G.E. Hofler, G. Meishaugen, and M.S. Hagedorn *et al.*, *J. Cryst. Growth* **138**, 667 (1994).
- [4] C.N. King, *J. Vac. Sci. Technol. A* **14**, 1729 (1996).
- [5] Y. Sato, N. Takahashi, and S. Sato, *Jpn. J. Appl. Phys. Lett.* **2** **35**, L838 (1996).
- [6] S. Nakamura, N. Iwasa, M. Senoh, and T. Mukai, *Jpn. J. Appl. Phys.* **31**, 1258 (1992).
- [7] H. Amano, M. Kito, K. Hiramatsu, and I. Akasaki, *Jpn. J. Appl. Phys.* **28**, L2112 (1989).
- [8] C. Yuan, T. Salagaj, A. Gurary, P. Zawadzki, C. S. Chern, W. Kroll, and R. A. Stall, *J. Electrochem. Soc.* **142**, L163 (1995).
- [9] M. W. Wang, J. O. McCaldin, J. F. Swenberg, T. C. McGill, and R. J. Hauenstein, *Appl. Phys. Lett.* **66**, 1974 (1995).
- [10] J. O. McCaldin, M. W. Wang, and T. C. McGill, *J. Crystal Growth* **159**, 502 (1996).
- [11] announced at [http : //www.storage.ibm.com/hardsoft/diskdrdl/micro/](http://www.storage.ibm.com/hardsoft/diskdrdl/micro/).
- [12] Materials for Flat-Panel Displays, *MRS Bulletin* **21** (1996).
- [13] Y.A. Ono, *Electroluminescent Displays*, World Scientific, Singapore (1995).
- [14] M. Yokoyama, K. Kashiroy, and S. Ohta, *J. Crystal Growth* **81**, 73 (1987).

- [15] I. P. McClean and C. B. Thomas, *Semicon. Sci. and Technol.* **7**, 1394 (1992).
- [16] T. Yao and S. Maekawa, *J. Crystal Growth* **53**, 423 (1981).
- [17] J. W. Cook, Jr., D. B. Eason, R. P. Vaudo, and J. F. Schetzina, *J. Vac. Sci. Technol. B* **10**(2), 901 (1992).
- [18] K. B. Ozanyan, L. May, J. E. Nicholls, J. H. C. Hogg, W. E. Hagston, B. Lunn, and D. E. Ashenford, *Solid State Commun.* **97**, 345 (1996).
- [19] O. Kanehisa, M. Shiiki, M. Migita, and H. Yamamoto, *J. Crystal Growth* **86**, 367 (1988).
- [20] S. Ohta, K. Kashiro, and M. Yokoyama, *J. Crystal Growth* **87**, 217 (1988).
- [21] K. Yoneda, T. Toda, Y. Hishida, and T. Niina, *J. Crystal Growth* **67**, 125 (1984).
- [22] J. E. Ayers, S. K. Ghandhi, and L. J. Schowalter, *J. Crystal Growth*, **113**, 2156 (1991).
- [23] E.C. Piquette, Z.Z. Bandić, J.O. McCaldin, and T.C. McGill, *Mat. Res. Soc. Symp. Proc.* **449**, 385 (1997).
- [24] E.C. Piquette, Z.Z. Bandić, J.O. McCaldin, and T.C. McGill, *J. Vac. Sci. Technol. B* **15**, 1148 (1997).
- [25] M. Volmer and A. Weber, *Z. Phys. Chem.* **119**, 277 (1926).
- [26] *Physics and Chemistry of II-VI Compounds*, edited by M. Aven and J.S. Prener (North-Holland, Amsterdam, 1967).
- [27] E. S. Hellman, *MRS Internet J. Nitride Semicon. Res.* **3**, 11 (1998).
- [28] J. Petruzzello, K.W. Haberern, S.P. Herko, T. Marshall, J.M. Gaines, S. Guha, G.D. Uren, and G.M. Haugen, *J. Cryst. Growth* **159**, 573 (1996).
- [29] Z. Z. Bandić, E. C. Piquette, J. O. McCaldin, and T. C. McGill, *Appl. Phys. Lett.* **72**, 2862 (1998).

- [30] F.J. Humphreys and M. Hatherly, *Recrystallization and related annealing phenomena* (Elsevier Science Inc., New York, 1995).
- [31] See for example M.J. Brau and R.A. Reynolds, US Patent N° 3, 849, 205 (1974).
- [32] R. Triboulet, J.O. Ndap, A. Tromson-Carli, P. Lemasson, C. Morhain, and G. Neu, *J. Cryst. Growth* **159**, 156 (1996).
- [33] R. Triboulet, J.O. Ndap, A. El Mokri, A. Tromson-Carli, and A. Zozime, *J. De Phys. IV* **5**, 141 (1995).
- [34] E. Tournie, C. Morhain, G. Neu, M. Laügt, C. Ongaretto, J.P. Faurie, R. Triboulet, and J.O. Ndap, *J. Appl. Phys.* **80**, 2983 (1996).
- [35] M. Meshkinpur, M.S. Goorsky, G. Chu, D.C. Streit, T.R. Block, and M. Wojtowitz, *Appl. Phys. Lett.* **66**, 748 (1995). See also Ref. [34]
- [36] F.C. Brown, *The Physics of Solids - Ionic Crystals, Lattice Vibrations and Imperfections* (Benjamin, New York, 1967).
- [37] JSM-6400 Scanning Microscope, Manual, Chapter 5, JEOL Ltd. (1989).
- [38] A. Koma, *Prog. Crystal Growth and Charact.* **30**, 129 (1995).

Chapter 4 The values of minority carrier diffusion lengths and lifetimes in GaN and their correlation with structural properties

4.1 Introduction

High critical fields for electric breakdown and good electronic properties of GaN and SiC have caused significant research interest for applications of these materials in high power, microwave, and high temperature electronics. While both of these materials can support large electric fields before breakdown, nitrides have several additional advantages over SiC, including the availability of cheap and efficient halide vapor phase growth epitaxy (HVPE) technology for thick standoff layers and the possibility of GaN/AlGaN heterojunctions. [1, 2] Some of the important parameters for high power devices are critical field for electric breakdown, thermal conductivity and minority carrier diffusion lengths and lifetimes. Critical field for electric breakdown and thermal conductivity are discussed in more detail in Chapter 5. Besides critical field and thermal conductivity, important parameters for design and performance of high power devices are minority carrier diffusion lengths and lifetimes. Minority carrier (both electron and hole) diffusion lengths and lifetimes are important for bipolar devices and they directly influence sensitivity of UV photodetectors, [3] current gain of bipolar transistors [4] and forward drop voltage of thyristors, [2, 4, 5] to name a few examples. In this chapter, the measurements of minority carrier (both holes and electrons) diffusion lengths and lifetimes in GaN by electron beam induced currents (EBIC) are presented. The influence of structural defects on these minority carrier

properties is experimentally analyzed through atomic force microscopy (AFM) studies of surfaces of these materials and discussed through simple physical models.

4.2 Experimental setup

We determined the minority carrier (holes and electrons) diffusion lengths and lifetimes from the EBIC measurements implemented in a scanning electron microscope (SEM). The samples used for this study were Schottky diodes fabricated on GaN substrates.

4.2.1 Device preparation

The samples used were unintentionally doped (UID), n- and p-type doped GaN on sapphire grown by MOCVD, molecular beam epitaxy (MBE) and HVPE. UID samples were n-type as grown, n-type samples were doped with Si, while p-type samples were doped with Mg. EBIC measurements were carried out on Schottky diodes fabricated on these GaN films. Prior to device processing, the GaN surface was cleaned with organic solvents, and then dipped in HF : H₂O(1 : 5).

Contact metals were sputtered in a chamber with a background pressure of $2 \cdot 10^{-8}$ Torr and patterned to produce Schottky contacts as well as large-area ohmic contacts (see Fig. 4.1). In the case of UID and n-type GaN, Au was used as a Schottky contact, while Ti/Al was used as an ohmic contact. For p-type GaN, a Ni/Au metalization scheme was used for the ohmic contact, while Ti/Au was used for the Schottky contact. The Schottky diodes on the GaN chip were placed on a 24-pin die package, contacted with Au wires and transferred to the SEM. The SEM micrograph of fabricated device is shown in Fig. 4.2. More details about current-voltage characteristics of the fabricated devices are given in Chapter 5 and section 5.5.

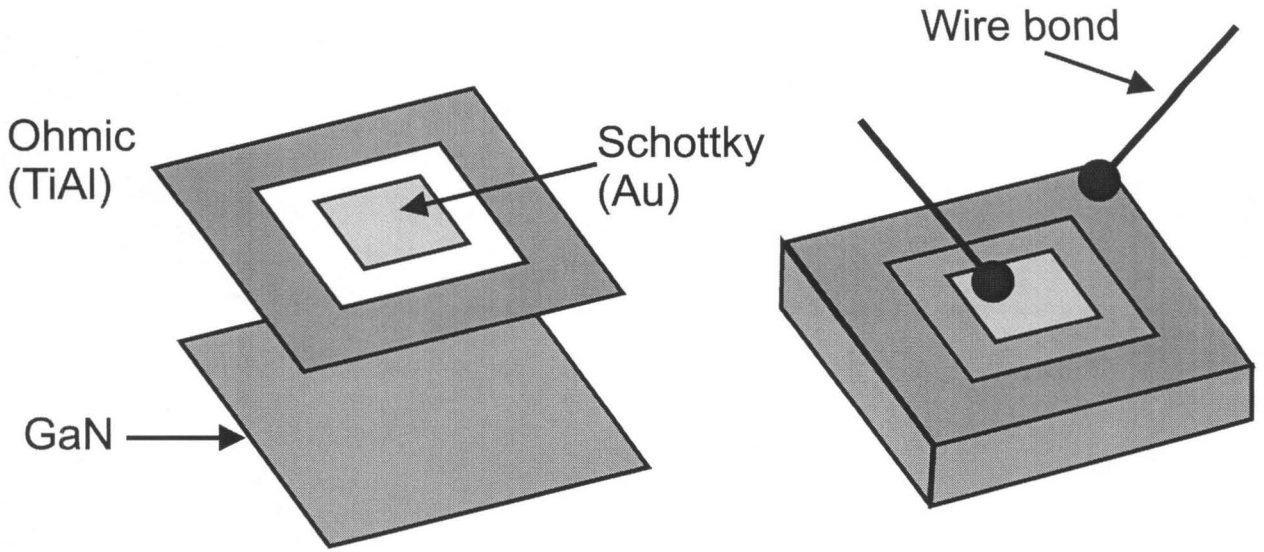


Figure 4.1: Schematic of the Schottky devices processed on the GaN substrates. Schottky and ohmic contacts are fabricated by sputtering and optical lithography. Schottky diodes on GaN chip were mounted on die package and Au wires were contacted (wire-bonded) to metal contacts.

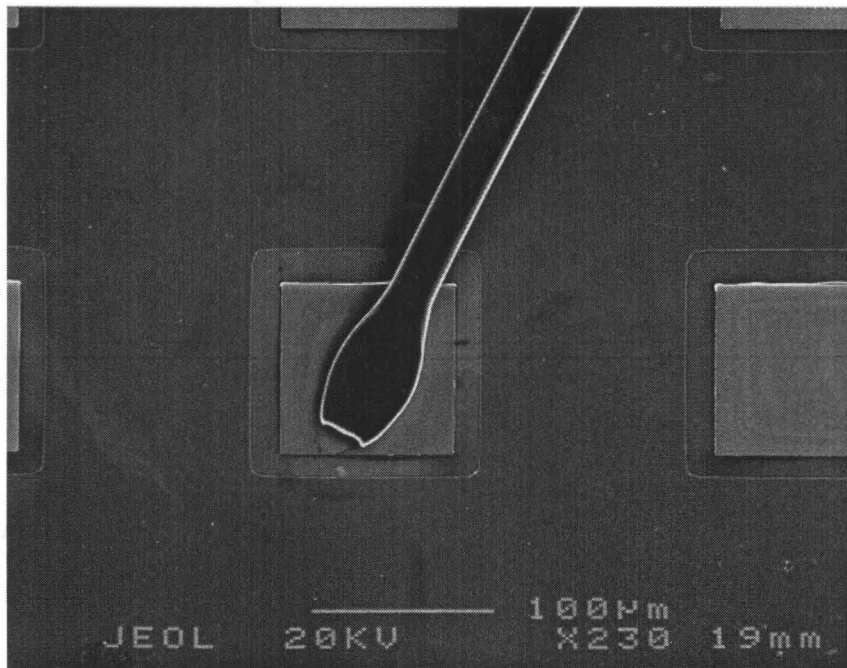


Figure 4.2: Scanning electron micrograph of fabricated device used for EBIC measurements.

4.2.2 Electron beam induced current measurements setup

EBIC measurements on these samples were carried out in a JEOL 6400V scanning electron microscope, using either GW Electronics pre-amplifier model 103B, followed by GW Electronics Specimen Current Amplifier model 31, or Keithley 486 picoammeter. [6, 7] The schematic of the experimental setup is shown in Fig. 4.3.

When electrons from the electron beam are injected into the semiconductor near a Schottky contact, generation of electron-hole pairs occurs (see Fig. 4.4). Due to the large concentration of holes in p-type sample (or electrons in UID or n-type sample) compared to the generated electron-hole concentration, only minority carriers are effectively generated, assuming low electron beam currents. This is the reason why a p-type sample is required for measurement of electron (as a minority carrier) transport parameters, and n-type sample is required for measurement of hole transport properties. If the circuit is closed with a lateral ohmic contact on the semiconductor surface, minority carriers which diffuse close to the Schottky contact generate an induced current. The current follows the law $I = kx^\alpha \exp(-x/L_m)$ where α ranges from $-1/2$ in case of negligible surface recombination to $-3/2$ in case of large surface recombination. L_m is the minority carrier diffusion length and x is the distance between the Schottky contact and the injection spot. [8] The derivation of EBIC is given in Appendix A in the analytically simple case of large (infinite) surface recombination. The minority carrier diffusion length is obtained by fitting the measured $I(x)$ dependence to the theoretical equation. The small surface recombination corresponding to $\alpha = -1/2$ was assumed since the GaN samples analyzed here have good photoluminescence efficiency. Even if infinite surface recombination was assumed, which is unlikely, the quantitative values would not change more than 20–25%, since the analytical expression for EBIC is dominated by the exponential term. The data was collected at distances x larger than either the electron range in the material, or the diffusion length, so that expression for EBIC is approximately correct (see Appendix A). [8] The minority carrier lifetime, τ_m , can then be obtained from Einstein's relationship $L_m^2 = D_m \tau_m$, where the diffusivity, D_m , can be calculated from the mi-

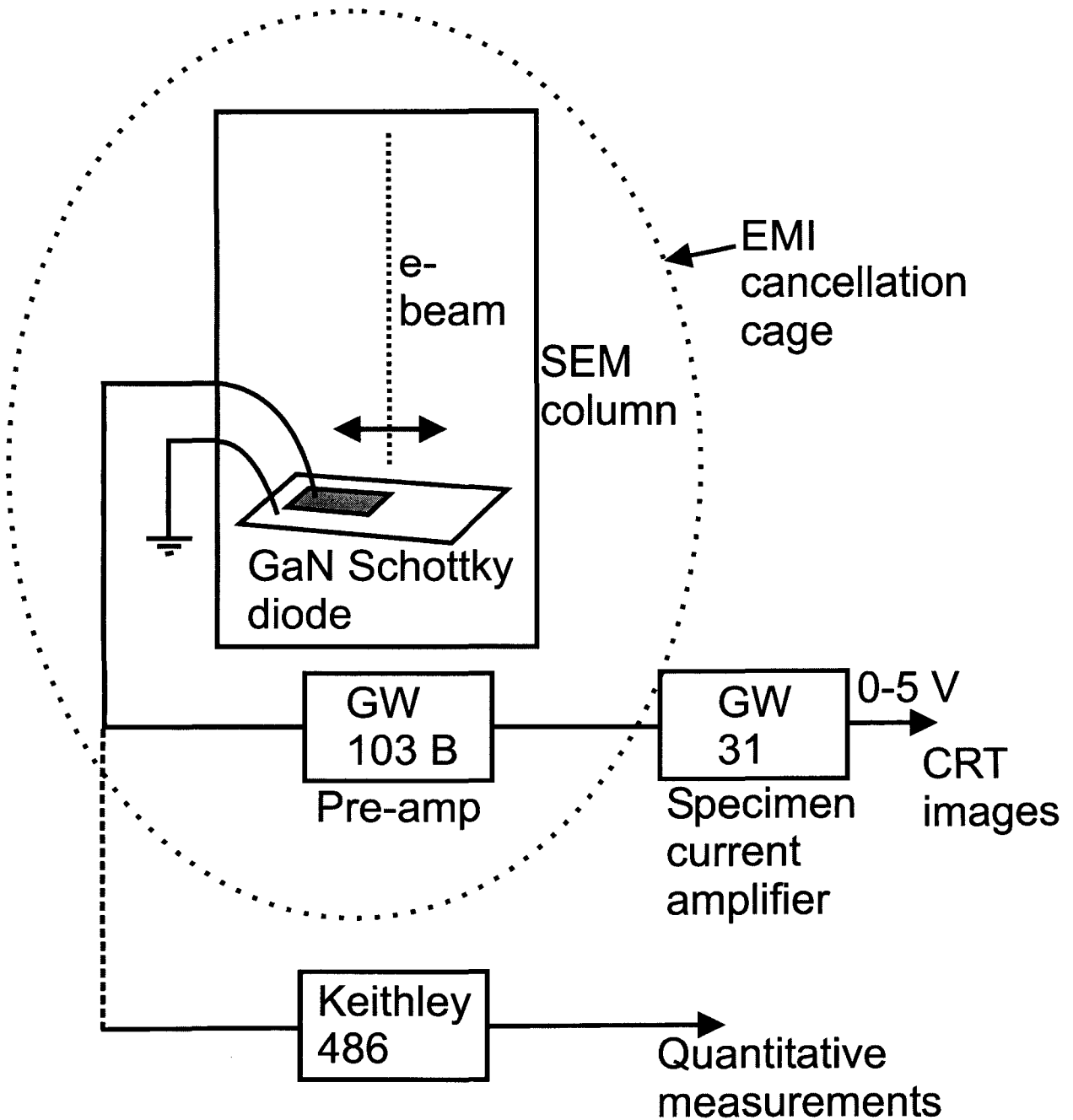


Figure 4.3: Schematic of the experimental setup for EBIC measurements. Sample mounted on die package is placed inside SEM. SEM column is protected by the electromagnetic interference (EMI) cancellation cage. If EBIC is measured by combination of GW Electronics 103 B preamplifier and GW 31 specimen current amplifier, signal is used to form EBIC images. Keithley 486 picoammeter was used for the quantitative measurements.

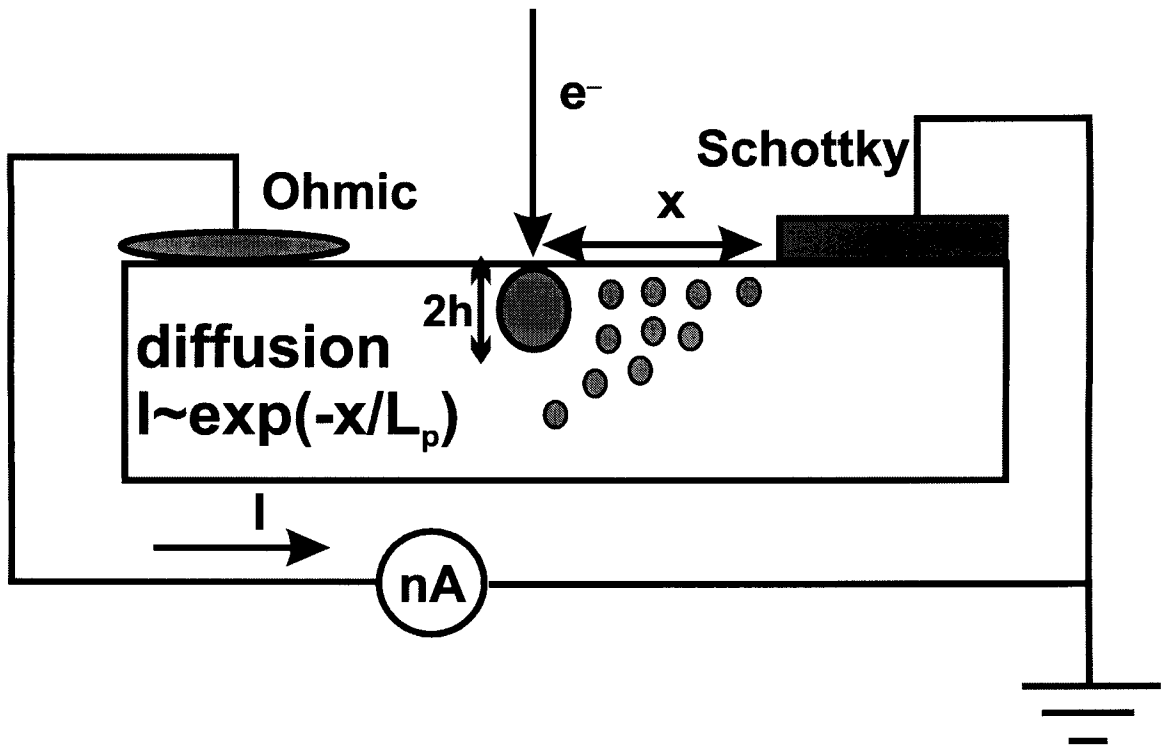


Figure 4.4: Experimental setup for EBIC measurements of minority carrier diffusion lengths using Schottky diodes. Injected minority carriers diffuse to the Schottky contact and form EBIC current.

minority carrier mobility using $D_m = (kT/q) \cdot \mu_m$. Hall measurements were used to obtain carrier mobilities.

4.2.3 Optimization of electron beam current and voltage

Considerations for electron beam current-minority carrier injection

The electron beam current has to be kept low enough so that only minority carriers are effectively injected. High energy electrons impinging on the surface will penetrate inside the semiconductor, and since they have enough energy (much larger than the threshold energy approximately equal to the energy of the bandgap which is energy required to produce electron-hole pair), each electron will produce one electron-hole pair with smaller energies in the avalanche process. This process will continue until the electron-hole pairs of last generation reach energy levels below the threshold energy. The radius of the generation volume can be approximated by $h = [3.98 \cdot 10^{-2}/\rho] U_b^{1.75}$, [9] where $\rho = 6.056 \text{ g/cm}^3$ is density of GaN and U_b is the energy of the electron beam (see Fig. 4.5). This relationship overestimates the generation radius when compared to more accurate Monte-Carlo calculations. [10]. If a multiplicative factor of 2/3 is used, the equation $h = 4.44 \cdot 10^{-3} U_b^{1.75}$ is obtained, which agrees well with Monte-Carlo simulations. [10] The range as a function of electron beam voltage is shown in Fig. 4.6a.

Total generation (gain, or number of generated electrons per one impinging electron) inside the generation volume will be: [11]

$$G = (1 - \eta_c) \frac{U_b}{U_{th}}, \quad (4.1)$$

where η_c represent the loss of electron-hole pair generation by electron backscattering, and U_{th} is threshold energy for electron-hole pair production, empirically given by: [11]

$$U_{th} \approx 2.1E_g + 1.3eV. \quad (4.2)$$

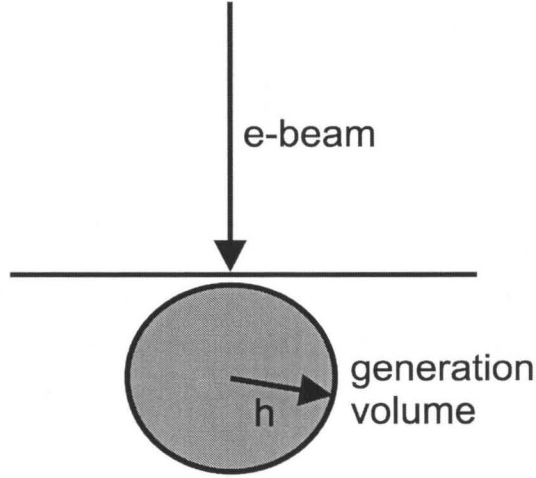


Figure 4.5: Generation volume of electrons approximated by sphere of radius R .

The generation rate of minority carriers in the generation volume is given by: [11]

$$n' = \frac{I_b}{q} G \frac{1}{\frac{4}{3}\pi h^3}, \quad (4.3)$$

where q is electron charge. Finally, the steady state concentration of generated excess carriers can be estimated as $\Delta n = \Delta p = n'\tau$, [11] where τ is relaxation lifetime. Since only minority carriers have to be effectively injected, in the case of minority holes in n-type GaN, condition $\Delta n \ll n$ has to be fulfilled. In terms of electron beam current:

$$I_b \ll \frac{n \frac{4}{3}\pi h^3}{G\tau_p} q \quad (4.4)$$

Using typical values for electron beam energy in the range of 15-20 kV, a carrier concentration of 10^{17} cm^{-3} and minority carrier lifetime of 10 ns, one finds that the electron beam current has to be kept smaller than 20 nA. This condition was carefully taken into account during our measurements. If minority carrier injection condition is not fulfilled, the electron-hole recombination lifetime will decrease, resulting in underestimate of the actual diffusion length.

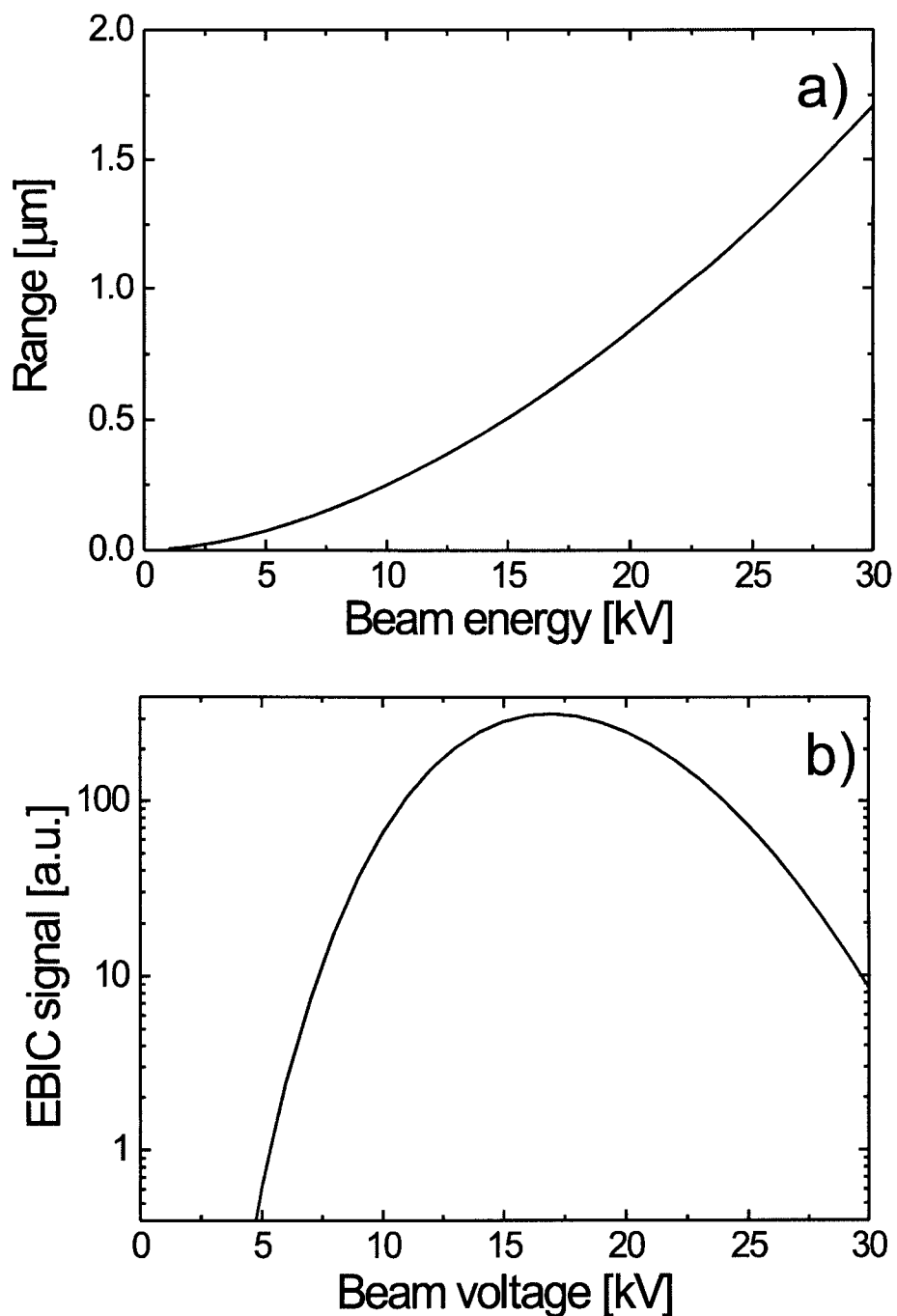


Figure 4.6: a) Range, or generation radius as a function of electron beam voltage for GaN. b) EBIC signal at distance $x = 2h$ as a function of electron beam voltage. The value $L_m = 0.25 \mu\text{m}$ was used for minority carrier diffusion length. The optimal voltage is in 15-20 kV region.

Optimization of electron beam voltage

Another important issue is finding the optimal electron beam voltage for the EBIC measurements. Clearly, if the beam voltage is very low, generation rate G will be low, and induced current which is proportional to G will also be low. That would result in small signal, which would be hard to measure. On the other side, if beam voltage is very high, the range h will be high, and therefore injection spot x has to be on distances larger than h . However, since induced current is also proportional to e^{-x/L_m} , large distances x will also result in small signal. In the case of small surface recombination, induced current is proportional to the electron beam current I_b , generation rate G and factor $x^{-1/2}e^{-x/L_m}$. [8] From considerations in previous section (see Eq. 4.4), we can notice that $I_b G \sim h^3$. For example, if we consider induced current at distance $x = 2h$, we obtain:

$$EBIC \sim h^3(2h)^{-1/2}e^{-2h/L_m} \sim h^{5/2}e^{-2h/L_m} \quad (4.5)$$

In the case of large surface recombination, $EBIC \sim I_b G h x^{-3/2} e^{-x/L_m}$ which would result in the same form as Eq. 4.5. Equation 4.5 is shown in Fig. 4.6b) using a minority carrier diffusion length $L_m = 0.25 \mu\text{m}$, which was a typical value measured for MOCVD samples in this study. It can be noticed that the optimal electron beam voltage lies in the 15-20 kV range, where most of the measurements were done.

4.3 Measurements of minority carrier diffusion lengths and lifetimes

Typical examples of the line scan profiles of the EBIC as a function of distance from the edge of the Schottky contact in the case of MOCVD-grown UID and p-type GaN is shown in Fig. 4.7a and Fig. 4.7c respectively.

The EBIC line scan profiles are shown superimposed on the secondary electron images of the edge of the Schottky contact. Corresponding AFM images of the GaN

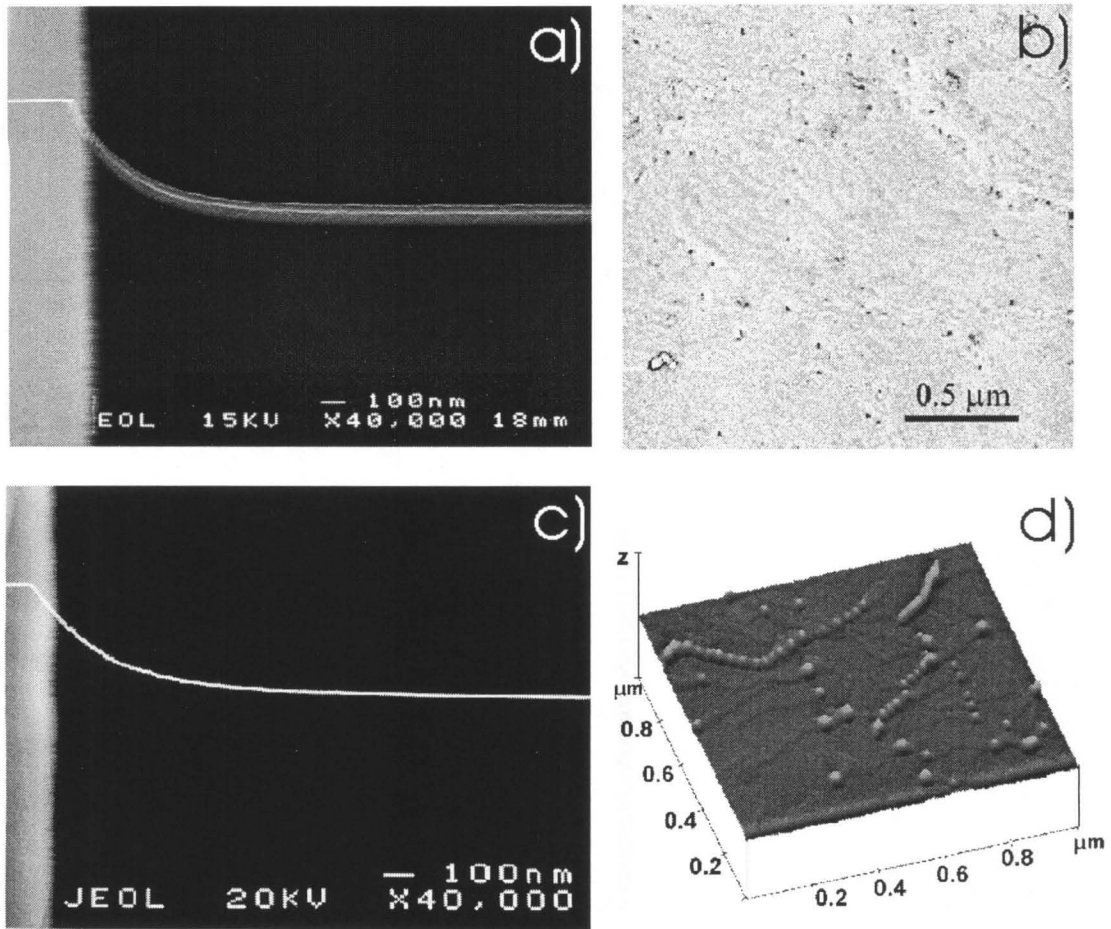


Figure 4.7: a) Line scan profile of the EBIC superimposed on the secondary electron image of the edge of the Au Schottky contact, for the MOCVD grown UID GaN. The electron beam voltage and current are 15KV and 0.4nA respectively. b) Processed AFM tapping mode phase image of the surface of the MOCVD-grown UID sample shown in a). This image shows that the boundaries of defect-free columns of crystal are decorated with linear dislocations. The defect-free regions span from 0.5–1.5 μm in size. c) Line scan profile of the EBIC superimposed on the secondary electron image of the edge of the Ti/Au Schottky contact, for the MOCVD grown p-type GaN. The electron beam voltage and current are 20KV and 0.5nA respectively. d) AFM scan of the surface of MOCVD p-type sample shown in c) shows pits induced by linear dislocations terminated at the surface which occupy boundaries between otherwise defect-free grains. The size of defect free grains varies in 0.5–1 μm range.

Table 4.1: Summary of the EBIC measurements. The diffusion lengths in each row of the table are average over the range of beam currents and different measurement positions on the sample. The corresponding lifetime is calculated according to the relation $L_p^2 = D_p \tau_p$, if the experimentally measured diffusivity of the minority carriers was available.

Sample	type	CC [cm^{-3}]	DD [cm^{-2}]	U_{beam} [KV]	I_{beam} [nA]	L [μm]	τ [ns]
MOCVD-1	n	10^{17}	$(2 - 5) \cdot 10^9$	10	0.2-0.5	0.29 ± 0.02	7
				20	1.4-5.6	0.25 ± 0.03	5.2
MOCVD-2	n	10^{17}	$(2 - 5) \cdot 10^9$	15	0.3-1	0.28 ± 0.03	6.5
				20	0.8-5.4	0.26 ± 0.02	5.6
				30	0.7-5.6	0.30 ± 0.03	7.5
MBE-1	n	10^{16}	$5 \cdot 10^9$	20	0.1-0.5	0.22 ± 0.03	
HVPE-1	n	10^{16}	10^8	20	1.3-2.6	$\approx 1 - 2$	
MOCVD-3	p	10^{17}	$5 \cdot 10^9$	20	0.05-0.5	0.20 ± 0.04	0.1
MOCVD-4	p	10^{17}	$5 \cdot 10^9$	20	0.05-1.7	0.21 ± 0.05	0.1

material are shown in Fig. 4.7b and Fig. 4.7d. A summary of results for GaN samples of both n- and p-type, grown by MBE, MOCVD and HVPE is shown in Table 4.1. Typical data used to extract diffusion lengths is shown in Fig. 4.8 in case of three samples grown by three different growth techniques. Minority carrier diffusion lengths shown in Table 4.1 are obtained after averaging over the range of beam currents, different measurement positions on the sample, and different Schottky diodes on each sample. MOCVD samples had diffusion lengths of approximately $(0.28 \pm 0.02) \mu\text{m}$ for holes and $(0.20 \pm 0.05) \mu\text{m}$ for electrons, MBE sample had hole diffusion length of $(0.22 \pm 0.03) \mu\text{m}$, while HVPE-grown sample had hole diffusion lengths in the $1 - 2 \mu\text{m}$ range. Since electron concentration of the HVPE sample was very low (10^{16} cm^{-3}), it was hard to achieve the minority carrier injection condition. If the minority carrier injection is violated, experimentally obtained values for diffusion lengths are typically underestimated. Therefore, actual diffusion lengths might be higher than $1 - 2 \mu\text{m}$. In the case of MOCVD samples, diffusivities of $D_p = 0.12 \text{ cm}^2/\text{s}$ and $D_n = 2.6 \text{ cm}^2/\text{s}$, for holes and electrons respectively, were obtained from Hall measurements of concentration and mobility. Using these values, in the case of MOCVD samples, we estimated a hole lifetime as a minority carrier of approximately 7 ns, and an electron lifetime as a minority carrier of approximately 0.1 ns. In the case of HVPE and MBE GaN,

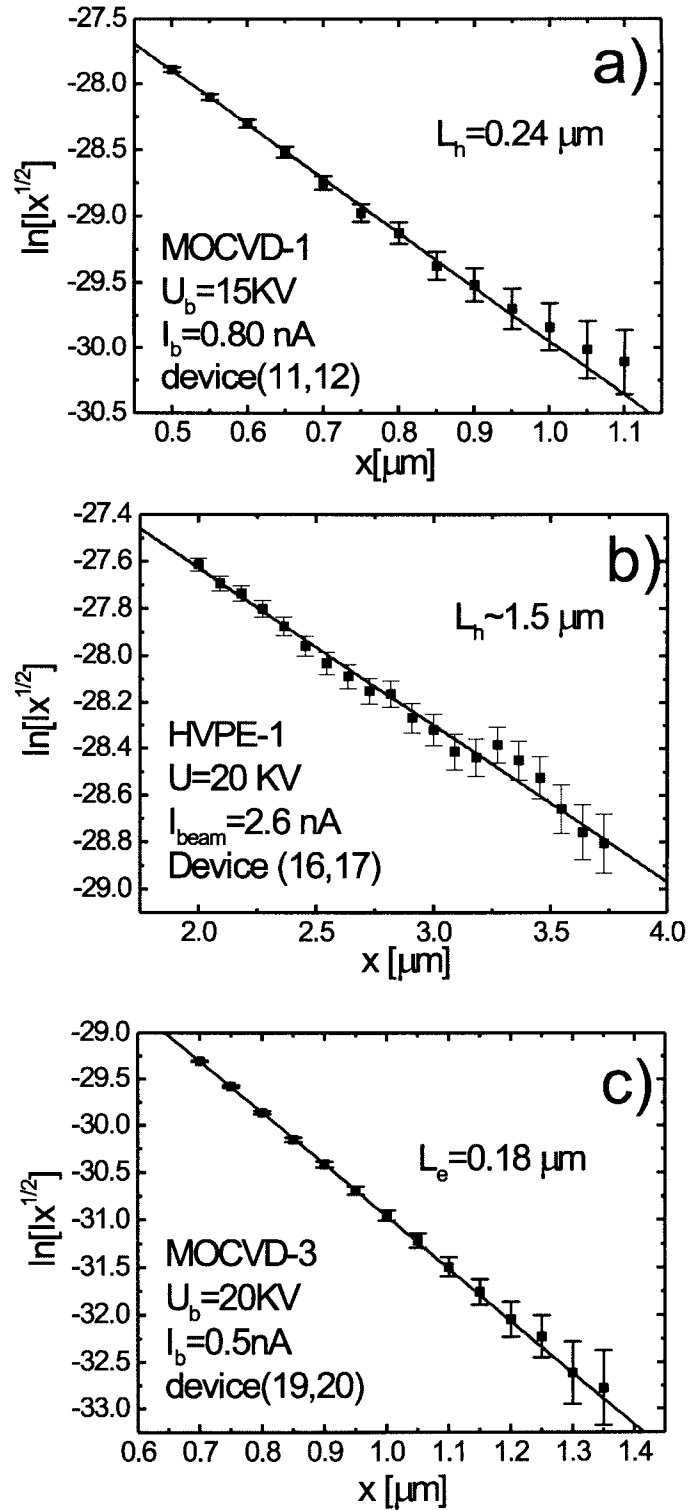


Figure 4.8: Typical data used to extract diffusion length. a) MOCVD-1 and hole diffusion length, b) HVPE-1 and hole diffusion length, and c) MOCVD-3 and electron diffusion length.

Table 4.2: Summary of the measured, estimated and calculated diffusion lengths and lifetimes from the published literature.

Material	Diffusion length [μm]	Minority carrier lifetime [ns]
GaN		$8 - 10^{\text{a}}$
InGaN/GaN MQW		$15 - 20^{\text{b}}$
GaN	0.1^{c}	
InGaN/GaN MQW		$1 - 3^{\text{d}}$
GaN	$\leq 0.25^{\text{e}}$	
GaN	0.05^{f}	
GaN	$1.2 - 3.4^{\text{g}}$	15^{g}
GaN	$1.7 - 2.5^{\text{h}}$	

^a Estimated from reference [12].

^b Reference [13].

^c Reference [3].

^d Reference [14].

^e Reference [10].

^f Reference [15].

^g Reference [16].

^h Reference [17].

p-type doped samples were not available, and therefore diffusivities and mobilities of holes could not be measured. This resulted in the lack of estimate for hole lifetime for these particular samples.

Measurements and calculations of minority carrier (hole) diffusion lengths and lifetimes obtained from the published literature are shown in Table 4.2, in the case of GaN and InGaN/GaN multiple quantum wells (MQW). We can observe variation in measured (or estimated) diffusion lengths in the range between $0.05 \mu\text{m}$, [15] and $3.4 \mu\text{m}$. [16] The variation in hole lifetime is smaller, and ranges from 1 ns, [14] to 20 ns. [13] Variation in these values is attributed to the variation in structural properties of GaN.

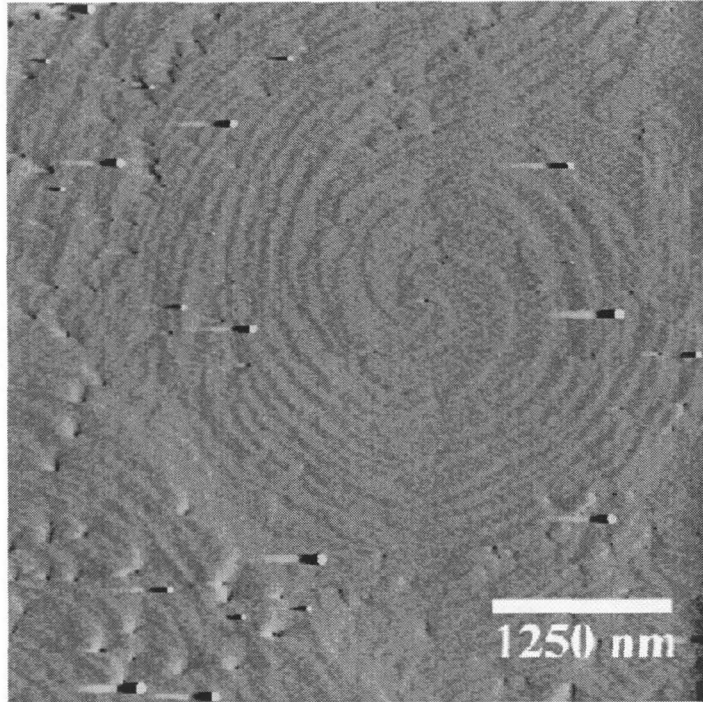


Figure 4.9: AFM scan of the surface of HVPE-grown GaN sample. Large pits-free areas can be observed.

4.4 Correlation of minority carrier lifetimes with structural defects

4.4.1 Experimental observations by Atomic Force Microscopy

The lack of a suitable GaN substrate has forced researchers to grow GaN on other substrates, such as SiC, GaAs and most notably sapphire. However, growth on lattice-mismatched and thermally-mismatched substrates causes a number of defects which propagate from the GaN/substrate interface. A typical dislocation density for material grown directly on sapphire is in the $10^9 - 10^{10} \text{ cm}^{-2}$ range. More recently, using lateral epitaxial overgrowth technique, it is possible to grow GaN films with a dislocation density in the 10^7 cm^{-2} range. [18] Parallel to our EBIC measurements of minority carrier diffusion lengths and lifetimes, we performed extensive structural characterization of the surfaces of GaN samples analyzed here using AFM to establish

the possible effects that linear dislocations and other defects may have on transport properties. [19] Linear dislocations are known to induce pits on the surface which can be measured by AFM. [20] On most of the AFM images, we observed that linear dislocation-induced pits are located at boundaries between otherwise defect-free grains. We can notice from AFM images for MOCVD samples in Figs. 3c) and 3d) that the measured diffusion lengths (in the range of $0.2 - 0.3 \mu\text{m}$) are smaller than the average defect-free grain size, which is in the range between $0.5 \mu\text{m}$ and $1.5 \mu\text{m}$. If recombination at linear dislocations indeed occurs, [10] it would limit diffusion lengths to sub-grain size length, in agreement with our experimental observation. In addition, EBIC measurements on HVPE samples, which had smallest dislocation density of approximately 10^8 cm^{-2} , gave values for diffusion length in the range of $1 - 2 \mu\text{m}$. The AFM image of the surface of HVPE sample is shown in Fig. 4.9. This increase in measured diffusion length with decrease in linear dislocation density and increase in the size of defect-free grains is in qualitative agreement with recombination at linear dislocations.

4.4.2 Simple models for minority carrier lifetime as a function of structural properties: dislocation density or grain size

If minority carrier recombination is the limiting mechanism for minority carrier diffusion length and lifetime, it should be possible to derive an analytical model which connects a minority carrier property, such as lifetime, with the structural properties, such as linear dislocation density. Models of this type have been previously derived in case of GaP, [21].

Random distribution of dislocations

If we assume that linear dislocations are distributed in a hexagonal "honeycomb-type" array, then the dislocation density can be expressed as $N_{dd} = 1/(\pi r_s^2)$, where $2r_s$ is the distance between two first-neighbor dislocations (see Fig. 4.10a). Dislocations

are assumed to have core diameter $2r_0$. The minority carrier concentration (holes, for example) is obtained by solving the two-dimensional diffusion equation for the minority carrier concentration p :

$$D_p \nabla^2 p = \partial p / \partial t. \quad (4.6)$$

Boundary conditions are given by:

$$(i) \quad p|_{r=r_0} = 0 \quad (4.7)$$

$$(ii) \quad \left. \frac{\partial p}{\partial r} \right|_{r=r_s} = 0. \quad (4.8)$$

Boundary condition (i) reflects the fact that due to infinite recombination, the minority carrier concentration at dislocations must be zero. Condition (ii) is approximation to the periodic boundary condition. [21] After solving Eq. 4.6 in cylindrical geometry, minority carrier lifetime τ_{scat} is obtained: [21]

$$\tau_{scat} = \frac{1}{2\pi D_p N_{dd}} \left(\ln \frac{2}{r_0 \sqrt{\pi N_{dd}}} - 0.57 \right) \quad (4.9)$$

More details of the derivation leading to Eq. 4.9 can be found in Appendix B. If the minority carrier lifetime without scattering at dislocations is given by τ_0 , then the total minority carrier lifetime becomes $\tau_p^{-1} = \tau_0^{-1} + \tau_{scat}^{-1}$. Hole lifetime and corresponding diffusion length, obtained from the model, are shown in Fig. 4.10b as a function of dislocation density. In the calculation shown in Fig. 4.10b, we used measured value for hole diffusivity $D_p = 0.12 \text{ cm}^2/\text{s}$ obtained from MOCVD samples, and dislocation core radius of $r_0 = 30 \text{ nm}$, which is typically observed by AFM measurements.

Dislocations occupying grain boundaries

From the experimental observations of the linear dislocations patterns, it was observed that in the majority of samples linear dislocations are distributed at the boundaries of otherwise defect-free grains (as opposed to random distribution). The schematic of this type of distribution of linear dislocations is shown in Fig. 4.11a. In that case,

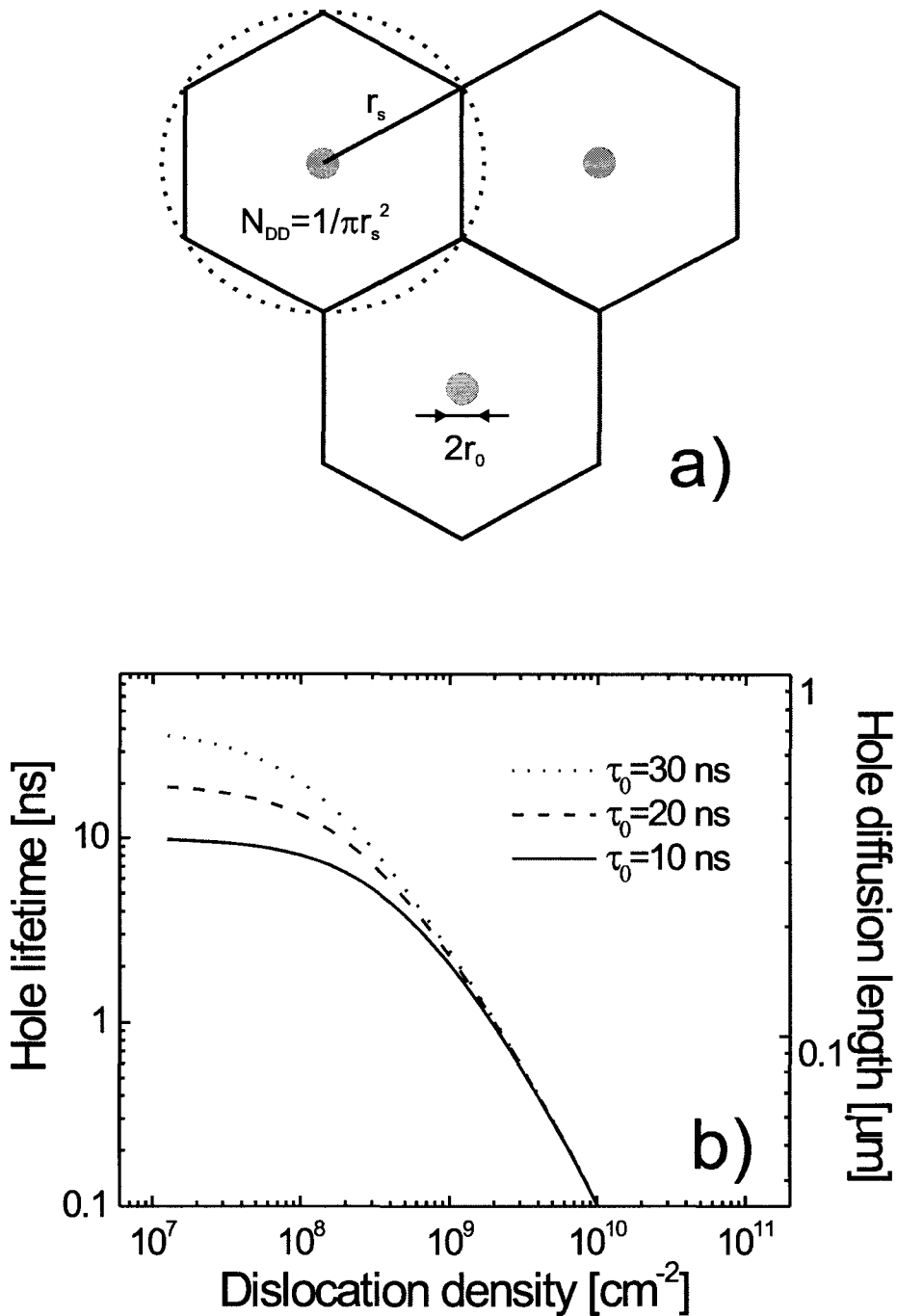


Figure 4.10: a) Uniform array of linear dislocations. Dislocation core radius is r_0 , and distance between dislocation is $2r_s$. b) Hole lifetime and diffusion length as a function of dislocation density, assuming uniform distribution of dislocations. The data is plotted using diffusivity measured for MOCVD samples. The hole lifetime τ_0 without recombination at dislocations is used as an parameter in the plot.

the boundary conditions become:

$$(i) \quad p|_{r=r_s} = 0 \quad (4.10)$$

$$(ii) \quad \left. \frac{\partial p}{\partial r} \right|_{r=0} = 0. \quad (4.11)$$

The solution in this case gives minority carrier lifetime (see Appendix B):

$$\tau_{scat} = \frac{r_s^2}{D_p} \frac{1}{2.4^2}. \quad (4.12)$$

The hole lifetime and diffusion length obtained from Eq. 4.12 are shown in Fig. 4.11b, using $\tau_p^{-1} = \tau_0^{-1} + \tau_{scat}^{-1}$, where τ_0 is minority carrier lifetime without scattering at linear dislocations.

Both models, either in the case of uniform distribution of linear dislocations, or in the case of linear dislocations occupying boundaries of defect-free grains, predict that minority carrier lifetime and diffusion length should increase with decrease in the dislocation density or increase in the size of defect-free grains. This is in qualitative agreement with our experimental observations, as can be observed from Fig. 4.7, Table 4.1 and Fig. 4.9.

4.4.3 Why would linear dislocations act as recombination centers?

It is interesting to discuss possible reasons for hole recombination at linear dislocations, and to give directions for future improvements of the model presented in previous section. Linear dislocations in GaN, in particular dislocations which have an edge component, are known to induce acceptor-like states, similar to Ge. [22, 23, 24] Since these states act as electron traps, [23, 24], dislocations become negatively charged and create a space charge region with a radius approximately equal to the Debye length, $\lambda_D = \sqrt{\epsilon_0 \epsilon_r k_B T / e^2 n}$, where k_B is the Boltzmann constant, T is the temperature and n is the electron concentration (see Fig. 4.12 and Appendix C). The negative charge creates an electric field oriented towards dislocation. Therefore, holes as minority car-

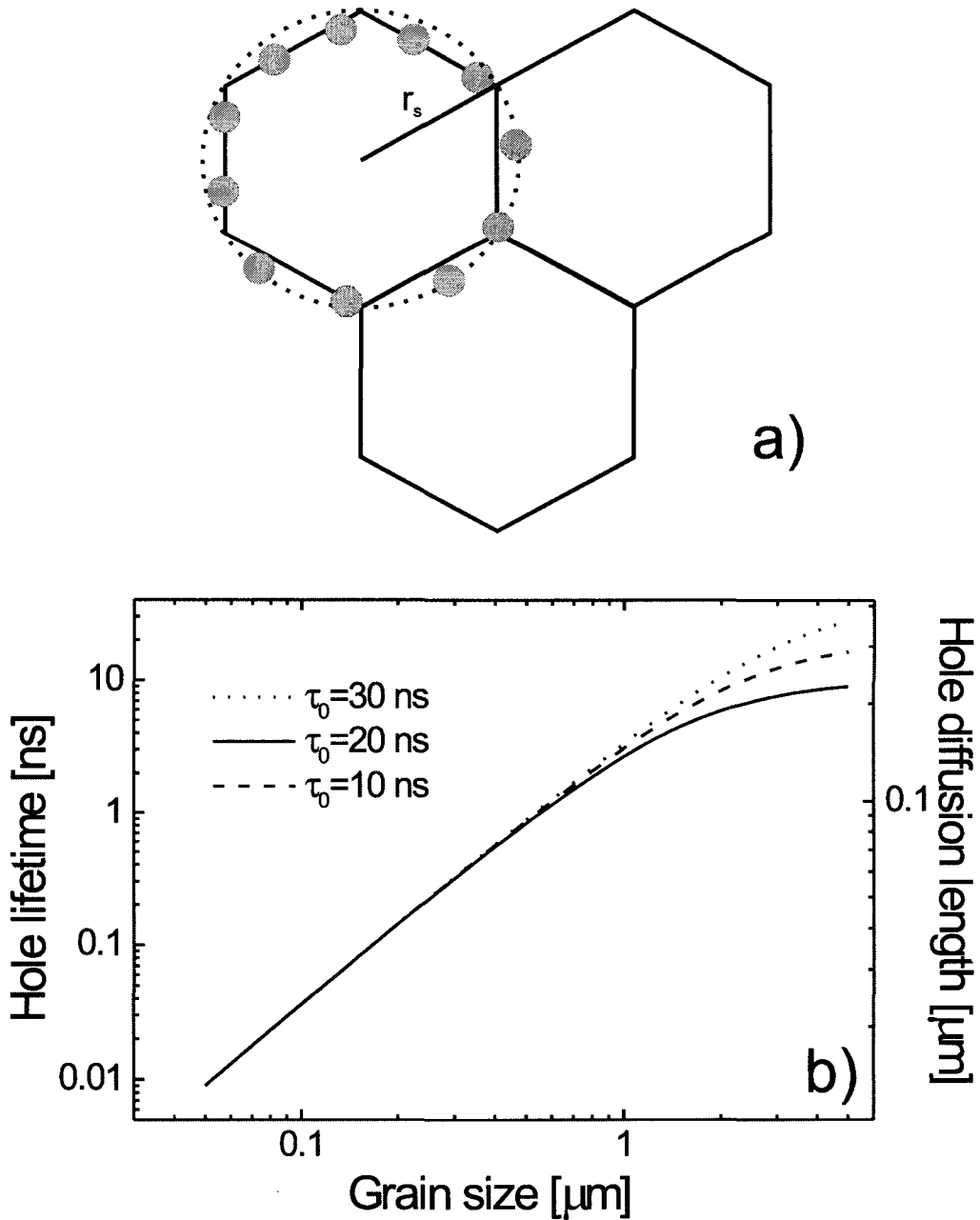


Figure 4.11: a) Dislocations occupying boundaries of otherwise defect-free grains. The radius of grains is r_s . b) Hole lifetime and diffusion length as a function of average grain size in the case of linear dislocations occupying grain boundaries of defect-free grains. The data is plotted using diffusivity measured for MOCVD samples.

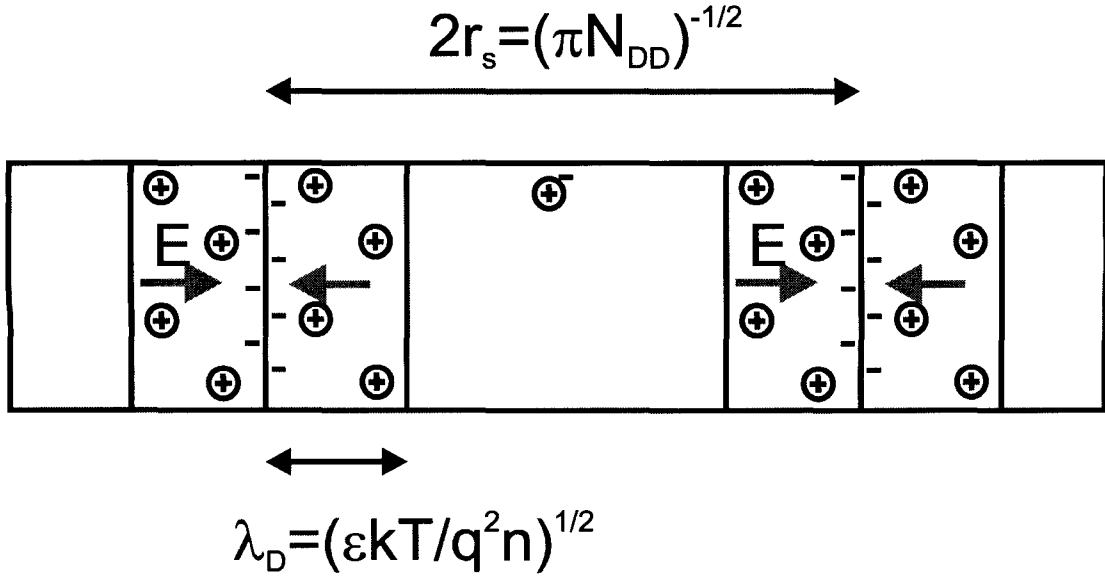


Figure 4.12: One-dimensional model of GaN with negatively charged linear dislocations. Negative charges (trapped electrons) at linear dislocations create space charge region with radius approximately equal to Debye length λ_D . Holes are attracted to linear dislocations by electric field of the space charge region, and recombine with trapped electrons.

riers will be attracted by this electric field, and will recombine with trapped electrons at the linear dislocation. This mechanism explains how linear dislocations may act as recombination centers. The hole diffusion length will then be limited by free space between dislocations given by $2r_s = 2/\sqrt{\pi N_{dd}}$, and by the Debye length which defines a region of electric field which attracts holes to recombine with trapped electrons at linear dislocations:

$$L_p \sim 2r_s - \lambda_D = \frac{2}{\sqrt{\pi N_{dd}}} - 2\sqrt{\frac{\epsilon_0 \epsilon_r k_B T}{e^2 n}} \quad (4.13)$$

One interesting consequence of this model is that the hole diffusion length might depend on both dislocation density and electron concentration.

4.5 Conclusion

The minority carrier diffusion lengths and lifetimes were measured for electrons and holes in MOCVD, MBE, and HVPE grown UID, n- and p-type doped GaN. The experimentally observed diffusion lengths were in the $0.2 - 0.3 \mu\text{m}$ range for MOCVD and MBE grown samples, and $1 - 2 \mu\text{m}$ in the case of HVPE grown sample. In the case of MOCVD grown samples, the hole lifetime was estimated to approximately 7 ns, and electron lifetime to approximately 0.1 ns. The same samples were structurally characterized by AFM, and the size of the defect-free regions surrounded by linear dislocations is found to be of the order of measured diffusion length, in qualitative agreement with minority carrier recombination at linear dislocations. A simple model was presented which explains an increase in minority carrier lifetime and diffusion length with a decrease in the dislocation density or increase in the size of defect-free grains. A model which explains why linear dislocations might act as recombination sites is also presented. Linear dislocations with edge component act as electron traps, and are consequently negatively charged and create space charge region around themselves. The electric field in the space charge region attracts holes to linear dislocations, where they might recombine with trapped electrons.

Bibliography

- [1] N.R. Perkins, M.N. Horton, Z.Z. Bandić, T.C. McGill, and T.F. Kuech, *Mat. Res. Soc. Symp. Proc.* **395**, 243 (1996).
- [2] Z.Z. Bandić, E.C. Piquette, P.M. Bridger, R.A. Beach, T.F. Kuech, and T.C. McGill, *Solid-State Electron.* **42**, 2289 (1998).
- [3] X. Zhang, P. Kung, D. Walker, J. Piotrowski, A. Rogalski, A. Saxler, and M. Razeghi, *Appl. Phys. Lett.* **67**, 2028 (1995).
- [4] S. Sze, *Semiconductor Devices* (John Wiley & Sons, New York, 1981).
- [5] B.J. Baliga, *Power Semiconductor Devices* (PWS, Boston, 1996).
- [6] Z.Z. Bandić, P.M. Bridger, E.C. Piquette, and T.C. McGill, *Appl. Phys. Lett.* **72**, 3166 (1998).
- [7] Z. Z. Bandić, P. M. Bridger, E. C. Piquette, and T. C. McGill, *Appl. Phys. Lett.* **73**, 3276 (1998).
- [8] H.K. Kuiken and C. Vanopdorp, *J. Appl. Phys.* **57**, 2077 (1985).
- [9] D.B. Holt and D.C. Joy, *SEM Microcharacterization of Semiconductors* (Academic Press, San Diego, 1985).
- [10] S. J. Rosner, E. C. Carr, M. J. Ludowise, G. Girolami, and H. I. Erikson, *Appl. Phys. Lett.* **70**, 420 (1997).
- [11] L. Reimer, *Scanning Electron Microscopy* (Springer-Verlag, Berlin, 1985).
- [12] F. Binet, J.Y. Duboz, E. Rosencher, F. Scholz, and V. Härle, *Appl. Phys. Lett.* **69**, 1202 (1996).

- [13] R. J. Radtke, U. Waghmare, H. Ehrenreich, and C. H. Grein, *Appl. Phys. Lett.* **73**, 2087 (1998).
- [14] X. Zhang, D. H. Rich, J. T. Kobayashi, N. P. Kobayashi, and P. D. Dapkus, *Appl. Phys. Lett.* **73**, 1430 (1998).
- [15] T. Sugahara, H. Sato, M.S. Hao, Y. Naoi, S. Kurai, S. Tottori, K. Yamashita, K. Nishino, L.T. Romano, and S. Sakai, *Jpn. J.Appl. Phys.* **37**, L398 (1998).
- [16] L. Chernyak, A. Osinsky, Henryk Temkin, J. W. Yang, Q. Chen, and M. Asif Khan, *Appl. Phys. Lett.* **69**, 2531 (1996).
- [17] J. W. Yang, C. J. Sun, Q. Chen, M. Z. Anwar, M. Asif Khan, S. A. Nikishin, G. A. Seryogin, A. V. Osinsky, L. Chernyak, H. Temkin, Chimin Hu, and S. Mahajan, *Appl. Phys. Lett.* **69**, 3566 (1996).
- [18] C. Sasaoka, H. Sunakawa, A. Kimura, M. Nido, A. Usui, and A. Sakai, *J. Cryst. Growth* **190**, 61 (1998).
- [19] P.M. Bridger, Z.Z. Bandić, E.C. Piquette, and T.C. McGill, *Appl. Phys. Lett.* **73**, 3438 (1998).
- [20] F.A. Ponce, *MRS Bull.* **22**, 51 (1997).
- [21] W.R. Harding, I. D. Blenkinsop, and D.R. Wright, *Electron. Lett.* **12**, 502 (1976).
- [22] G.L. Pearson, W.T. Read, and F.J. Morin, *Phys. Rev.* **93**, 666 (1954).
- [23] H.M. Ng, D. Doppalapudi, T.D. Moustakas, N.G. Weimann, and L.F. Eastman, *Appl. Phys. Lett.* **73**, 821 (1998).
- [24] N.G. Weimann, L.F. Eastman, D. Doppalapudi, H.M. Ng, and T.D. Moustakas, *J.Appl. Phys.* **83**, 3656 (1998).

Chapter 5 GaN based high power devices: design and fabrication

5.1 Design of GaN based high power devices

5.1.1 Introduction

The interest in wide bandgap materials is motivated by their high breakdown fields and the possibility of high temperature operation, with the primary candidates being SiC and GaN. Compared to silicon, approximately 10-20 times higher critical field for electric breakdown would result in much thinner devices, with smaller forward drop voltages and smaller power dissipation. This potential dramatic reduction in size and power dissipation attracted significant interest from both Department of Defense and electric utility industry. [1] Some of the major advantages of nitrides over SiC are the availability of cheap and efficient growth technology for thick standoff layers and the possibility of GaN/AlGaN heterojunctions. High quality GaN has been epitaxially grown by hydride vapor phase epitaxy (HVPE) with growth rates as high as $100\ \mu\text{m/hr}$. [2] Possible devices include Schottky diodes, power FET's, bipolar transistors and thyristors. Since all of the power supply functions can be produced by a switch and a rectifier, [3] our attempts have focused on producing Schottky diode rectifiers and thyristor switches based on GaN/AlGaN heterostructures. The Schottky diode is easy to fabricate and gives excellent high-speed rectification, while thyristors offer high current gain and the excellent current switching characteristics of bipolar technology.

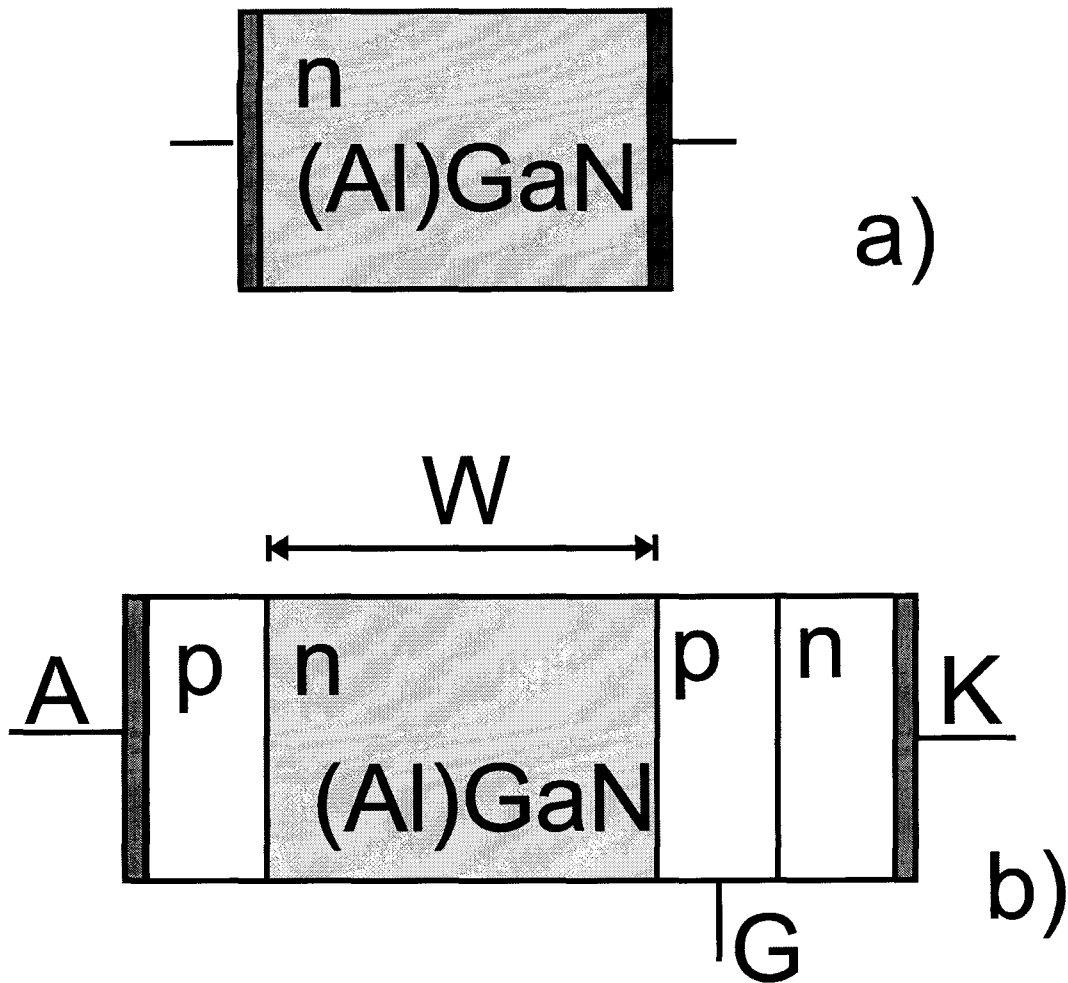


Figure 5.1: Schematic of nitride based: a) Schottky rectifier, b) thyristor.

5.1.2 Nitride based Schottky rectifiers and thyristor switches

The nitride based thyristor and Schottky rectifier are shown in Fig. 5.1. The principles of operation of these devices is well known and described in many classic texts. [4, 5] The numerous advantages one can obtain by implementing these devices in GaN/AlN semiconductor system will be considered here in detail.

5.1.3 Thickness and doping of the standoff layer

To estimate the required thickness and doping of the standoff layer, one has to consider the avalanche mechanism for the breakdown. By fitting Shockley's analytical form of the ionization coefficients $\alpha_0 \cdot \exp(-b/E)$ to the calculated values for electron and

hole avalanche multiplication coefficients, [6] the following equation is obtained for large values of the electric field:

$$\alpha_n = \alpha_p = 2.9 \cdot 10^8 \cdot \exp(-32.7[\text{MV/cm}]/E) \text{ m}^{-1} \quad (5.1)$$

To estimate the breakdown voltage of the standoff layer of thickness W and uniform doping N_d , the impact ionization integral equation should be solved: [4]

$$\int_0^{x_{sc}} \alpha(E(x)) dx = 1, \quad (5.2)$$

where $x_{sc} = \sqrt{2\epsilon_0\epsilon_r V_R/qN_d}$ is the width of the space charge layer. As a fit to the numerical solution to Eq. 5.2, the following equation is obtained for the dependence of the breakdown voltage on the doping concentration:

$$V_{BR}^{GaN} = 6860 \cdot \left(\frac{N_d[\text{cm}^{-3}]}{10^{16}}\right)^{-0.73} [\text{V}]. \quad (5.3)$$

For a meaningful solution, it is necessary that the width of the standoff layer is larger than the width of the space charge layer at the point of breakdown, which can be achieved at this reverse bias voltage if:

$$W \geq \sqrt{2\epsilon_0\epsilon_r V_{BR}/qN_d} = 7.58 \cdot 10^{-4} \cdot (V_B[\text{V}])^{1.19} [\mu\text{m}] \quad (5.4)$$

Also, the critical field for electric breakdown (as a maximum electric field at the onset of breakdown) for GaN is found to be:

$$E_{cr}^{GaN} = \sqrt{2qN_d V_B/\epsilon_0\epsilon_r} = 5.1 \text{ MV/cm} \cdot \left(\frac{N_d[\text{cm}^{-3}]}{10^{16}}\right)^{0.14}. \quad (5.5)$$

This gives a breakdown field of approximately 5 MV/cm for a doping range of 10^{16} cm^{-3} . It is important to point out that values close to this number have been experimentally confirmed with Schottky rectifiers [7, 8] and heterostructure field effect transistors. [9]. Equation 5.3 is plotted in Fig. 5.2a as a solid line. The dotted

lines represent the punch-through condition for different widths of the standoff layer. Intersections of the solid and dotted lines give the maximum reverse blocking voltage and the optimum doping for a given standoff layer thickness. It can be observed that a 5000 V standoff voltage GaN-based Schottky rectifier or thyristor can be obtained with an 18 – 20 μm thick layer with doping concentration of $1.5 \cdot 10^{16} \text{ cm}^{-3}$ which can be achieved with currently available nitride technology. For comparison, it would take 50 – 100 μm of SiC and 650 μm of Si at lower doping levels to withstand the same reverse bias voltage, which clearly highlights the advantage of nitrides in terms of smaller device resistance.

AlGaN standoff layer

In addition, if GaN is replaced with ternary compound AlGaN, there is a further improvement in critical field for electric breakdown because of the larger band gap of AlN. Since larger values of critical field for electric breakdown can be expected, even smaller thicknesses for the standoff layer are possible. Besides using AlGaN for higher critical field for electric breakdown, AlGaN/GaN heterojunctions can be used to enhance thyristor performance by optimizing injection efficiency. Since impact ionization coefficients for AlGaN are not available, it is not possible to use the same formalism as the one applied to GaN. To estimate the breakdown voltage for the uniformly doped AlGaN standoff layer, either in Schottky rectifiers or thyristors, we used the result that critical electric field for the breakdown scales with the square of the energy band gap, or $E_c \propto E_g^2$ (see Fig. 5.3). [10] Although crude and empirical in nature, this relation gives an estimate for the electric breakdown field in GaN (using a multiplicative coefficient which is determined from the fit to existing diamond and SiC data [10]) in good agreement with the more elaborate calculations above. Following that assumption, the critical field estimate for electric breakdown in a uniformly doped AlGaN layer will be:

$$E_{cr}^{AlGaN} = (E_g^{AlGaN} / E_g^{GaN})^2 \cdot E_{cr}^{GaN} \quad (5.6)$$

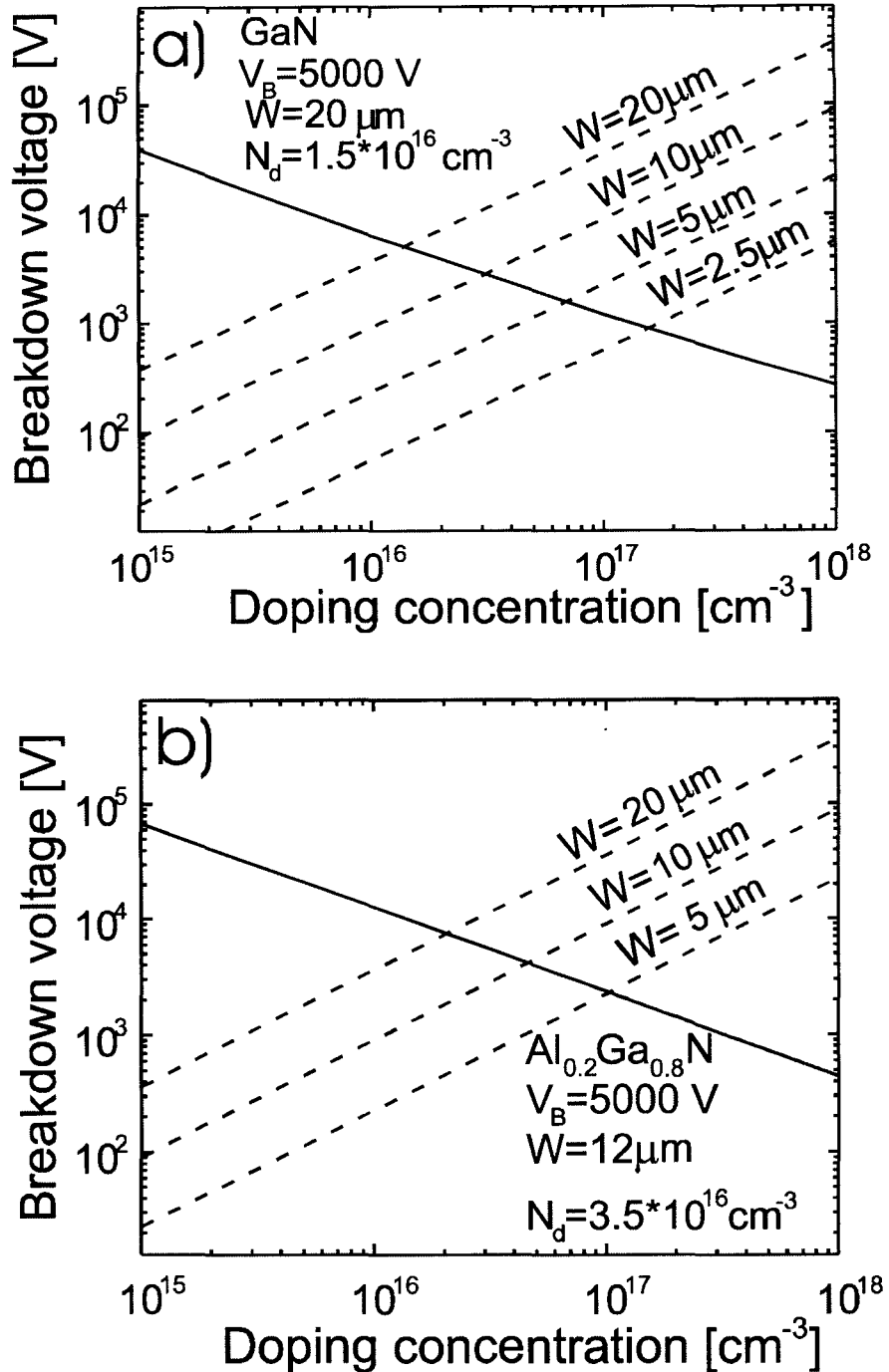


Figure 5.2: a) The solid line represents the breakdown voltage as a function of doping concentration for GaN layer. The dotted lines are the punch-through conditions as a function of doping for different layer thicknesses. The intersection of black and dotted lines gives the maximum reverse blocking voltage and the optimal doping for given standoff layer thickness. For example, 5000V can be achieved with $20\mu\text{m}$ of GaN with doping concentration of $1.5 \cdot 10^{16}\text{cm}^{-3}$. b) The same calculation for $\text{Al}_{0.2}\text{Ga}_{0.8}\text{N}$ gives that the reverse blocking voltage of 5000V can be achieved with $12\mu\text{m}$ of $\text{Al}_{0.2}\text{Ga}_{0.8}\text{N}$ with doping concentration of $3.5 \cdot 10^{16}\text{cm}^{-3}$.

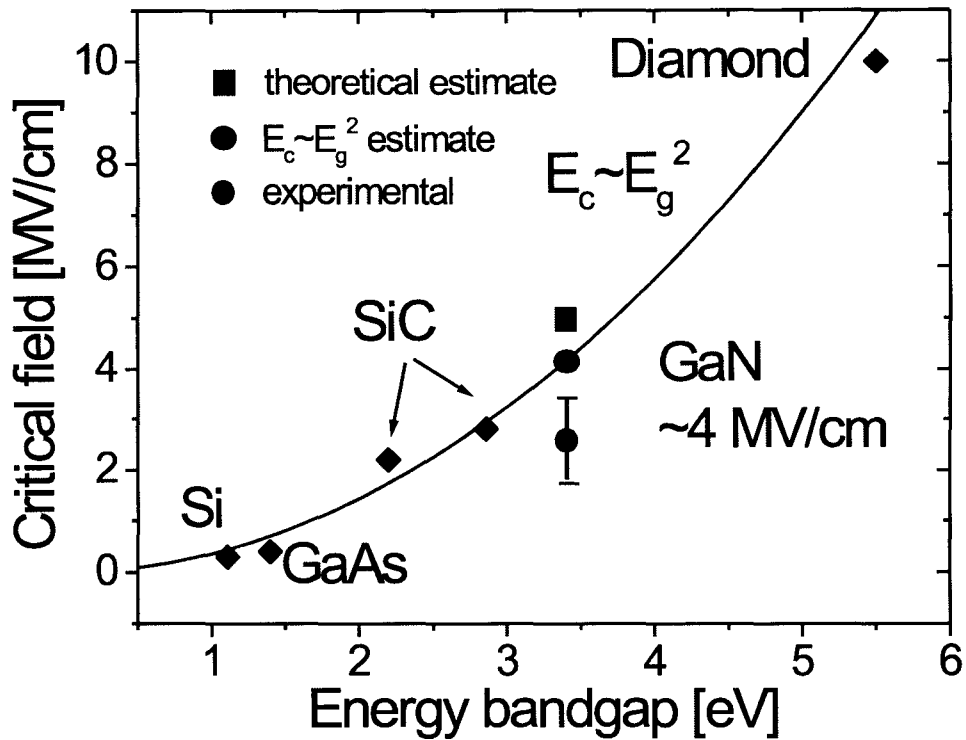


Figure 5.3: Critical field for electric breakdown as a function of energy bandgap. The critical field scales approximately with the square of the bandgap. This scaling law can be used to estimate critical fields for semiconductors where experimental data is not available.

Using Eq. (5.6) the breakdown voltage for a uniformly doped $\text{Al}_{0.2}\text{Ga}_{0.8}\text{N}$ layer with doping concentration N_d can be determined assuming Vegard's law for the band gap of a ternary nitride compound:

$$V_{BR}^{\text{Al}_{0.2}\text{Ga}_{0.8}\text{N}} = 12600 \cdot \left(\frac{N_d[\text{cm}^{-3}]}{10^{16}} \right)^{-0.73} [\text{V}] \quad (5.7)$$

This result is correct for the reverse blocking voltage of an n-AlGa_{0.8}N standoff layer for both the asymmetric p⁺-n junction (such as one in thyristor) or Schottky diode. Fig. 5.2b is a plot of avalanche breakdown and punch-through condition as a function of doping concentration for several widths of the $\text{Al}_{0.2}\text{Ga}_{0.8}\text{N}$ standoff layer. It can be seen that 5000V devices can be obtained with 12 μm thick $\text{Al}_{0.2}\text{Ga}_{0.8}\text{N}$ layer with a doping concentration of $3.5 \cdot 10^{16} \text{cm}^{-3}$.

5.1.4 Forward voltage drop for thyristor

Since the thyristor behaves as a p-i-n diode in the ON-state, a similar approach to find the forward voltage drop (ON-state voltage) can be applied to the thyristor as for the p-i-n diode. [4, 5] The forward drop voltage in the thyristor is approximately inversely proportional to the minority carrier (hole) lifetime in the standoff layer and directly proportional to the square of the standoff layer thickness, or $V_{ON} \propto W^2/\tau_h$. [4] However, if the hole lifetime in the standoff layer is small enough so that the minority carrier diffusion length is approximately half the thickness of the standoff layer, the ON-state voltage increases more rapidly with the decrease in lifetime. [5] The dependence of the ON-state voltage in the case of thyristor based on an AlGa_{0.8}N standoff layer as a function of the required breakdown voltage (which determines the required thickness of the standoff layer) and hole lifetime is shown in Fig. 5.4a. We notice that V_{ON} is lower when the thickness, W , is lower, as is the case for wide bandgap materials. Figure 5.4b shows the dependence of the ON-state voltage as a function of temperature and hole lifetime for a thyristor which uses a 12 μm thick $\text{Al}_{0.2}\text{Ga}_{0.8}\text{N}$ layer. In our calculations we used an electron mobility of $960 \cdot (T/300)^{-1.84} \text{cm}^2/\text{Vs}$ which was obtained by fitting a theoretically calculated mobility published in Ref. [11],

and assumed an electron to hole mobility ratio to be ~ 10 . The measured and estimated hole lifetimes for GaN range from 1 ns to 20 ns (see Chapter 4, Table 4.2). Measurements on HVPE-grown GaN with a lower defect density in the 10^8 cm^{-2} range resulted in hole diffusion lengths in the $1 - 2 \mu\text{m}$ range, which might correspond to even larger hole lifetimes (see Chapter 4.5). These measured values indicate that reasonably low ON-state voltages can be expected.

5.1.5 Power dissipation and maximum current density for thyristor

Power dissipation

Power in the device is dissipated both in the ON and OFF state. In the ON-state dissipated power depends on the product of ON-state voltage and forward current, while in the OFF-state it depends on product of saturation current and standoff voltage. The advantage of nitrides and other wide band gap materials is that the ON-state voltage is reduced by having smaller standoff layer thicknesses because of larger critical field, while saturation current density is expected to be low because of the small intrinsic carrier concentration. Assuming a 50% duty cycle, the power dissipated in the device is given by:

$$P_D = 1/2A(V_{ON}J_{ON} + R_cJ_{ON}^2 + J_sV_B) \quad (5.8)$$

where V_{ON} , J_{ON} and R_c are voltage, current density and contact resistance in the ON state, and J_s is the saturation current density. A is the cross-sectional area of the device. We used a value for total ohmic contact resistance which is a sum of the resistances to the p-type injection layer and n-type layer of $R_c = R_{cp} + R_{cn} \cong R_{cp} \sim 10^{-3} \Omega\text{cm}^2$. The ohmic contact resistance to the p-type injection layer dominates, while the resistance of the ohmic contact on the n-type layer can be neglected, since it is typically much smaller. Another potential advantage of wide band gap materials is small leakage current, due to the small intrinsic carrier concentration. Since intrinsic

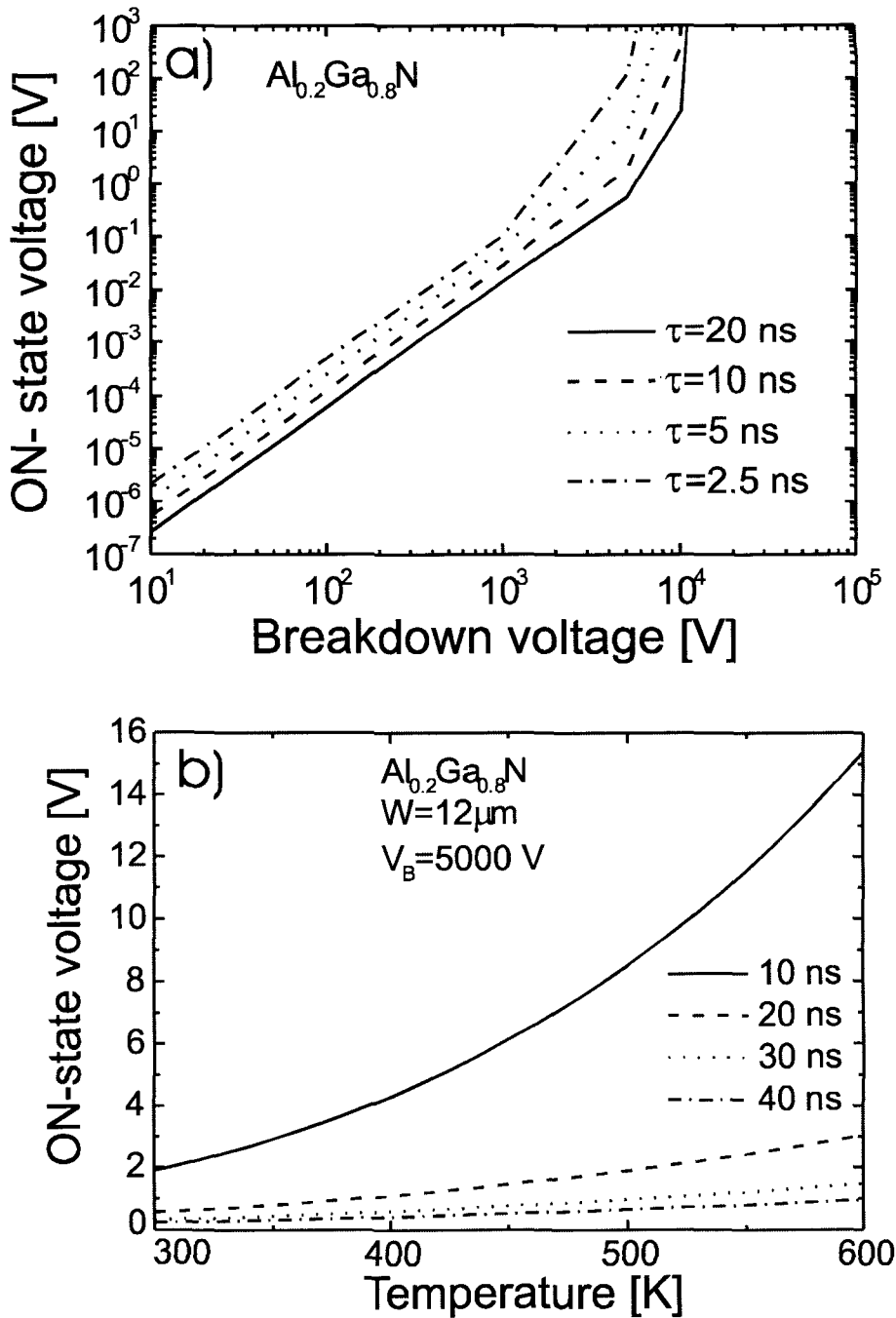


Figure 5.4: a) ON-state voltage for a thyristor with $\text{Al}_{0.2}\text{Ga}_{0.8}\text{N}$ standoff layer as a function of reverse breakdown voltage. Larger reverse breakdown voltage requires a larger standoff layer thickness, producing larger ON-state voltage. Note the more rapid increase in ON-state voltage at larger reverse blocking voltages ($> 5000\text{V}$). b) ON-state voltage for thyristor with $12 \mu\text{m}$ thick $\text{Al}_{0.2}\text{Ga}_{0.8}\text{N}$ standoff layer, as a function of temperature and hole lifetime. Reasonably low values of ON-state voltages can be expected for the measured range of hole lifetimes.

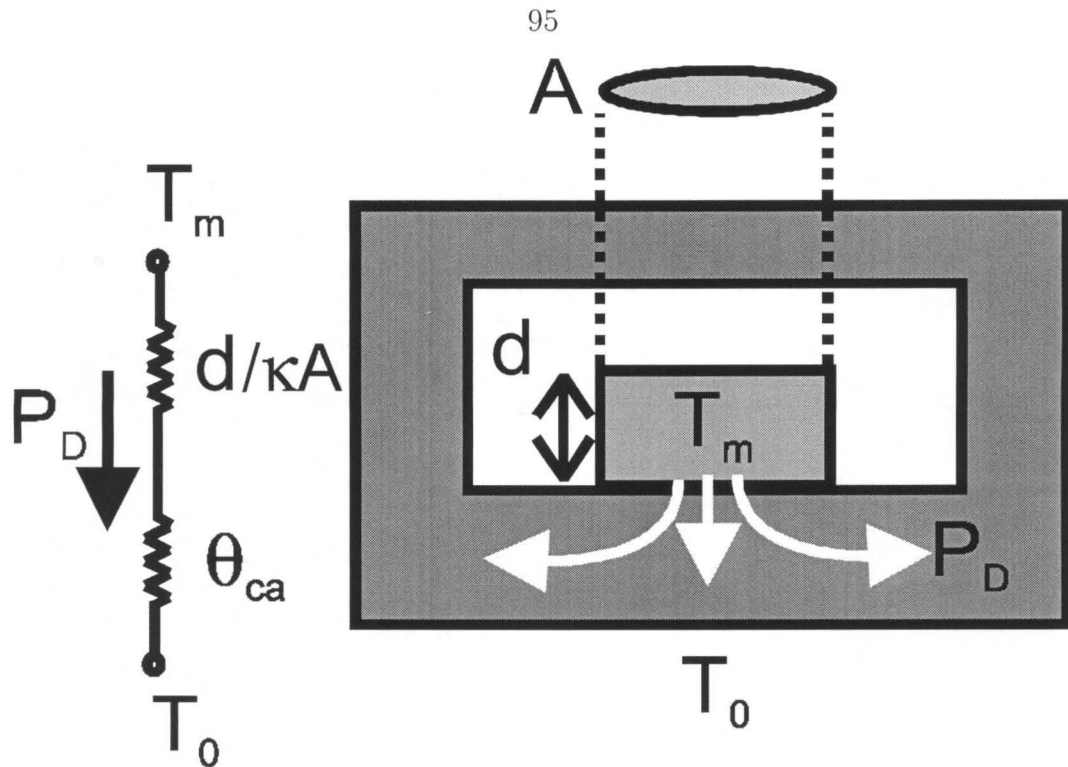


Figure 5.5: The equivalent circuit for thermal dissipation calculation. Temperature acts as a potential, while dissipated power acts as a current. A typical value of $1.0\text{Kcm}^2/\text{W}$ was used for the case to ambient thermal resistivity.

material has not yet been achieved with nitrides we have adopted an upper limit of $J_s = 10^{-3}\text{A}/\text{cm}^2$, although much smaller values should be possible with better materials.

Maximum current density

The maximum current density is limited by the ability of the device and its housing to dissipate power (see Fig. 5.5) while keeping the temperature of the device lower than the maximum allowed temperature. The difference between the device and ambient temperature under steady state conditions is determined by the product of the total device to ambient thermal resistivity and the total power dissipated in the device:

$$\Delta T = T_m - T_0 = (d/\kappa A + \theta_{ca})P_D. \quad (5.9)$$

The total device to ambient thermal resistivity is sum of the resistivities of the

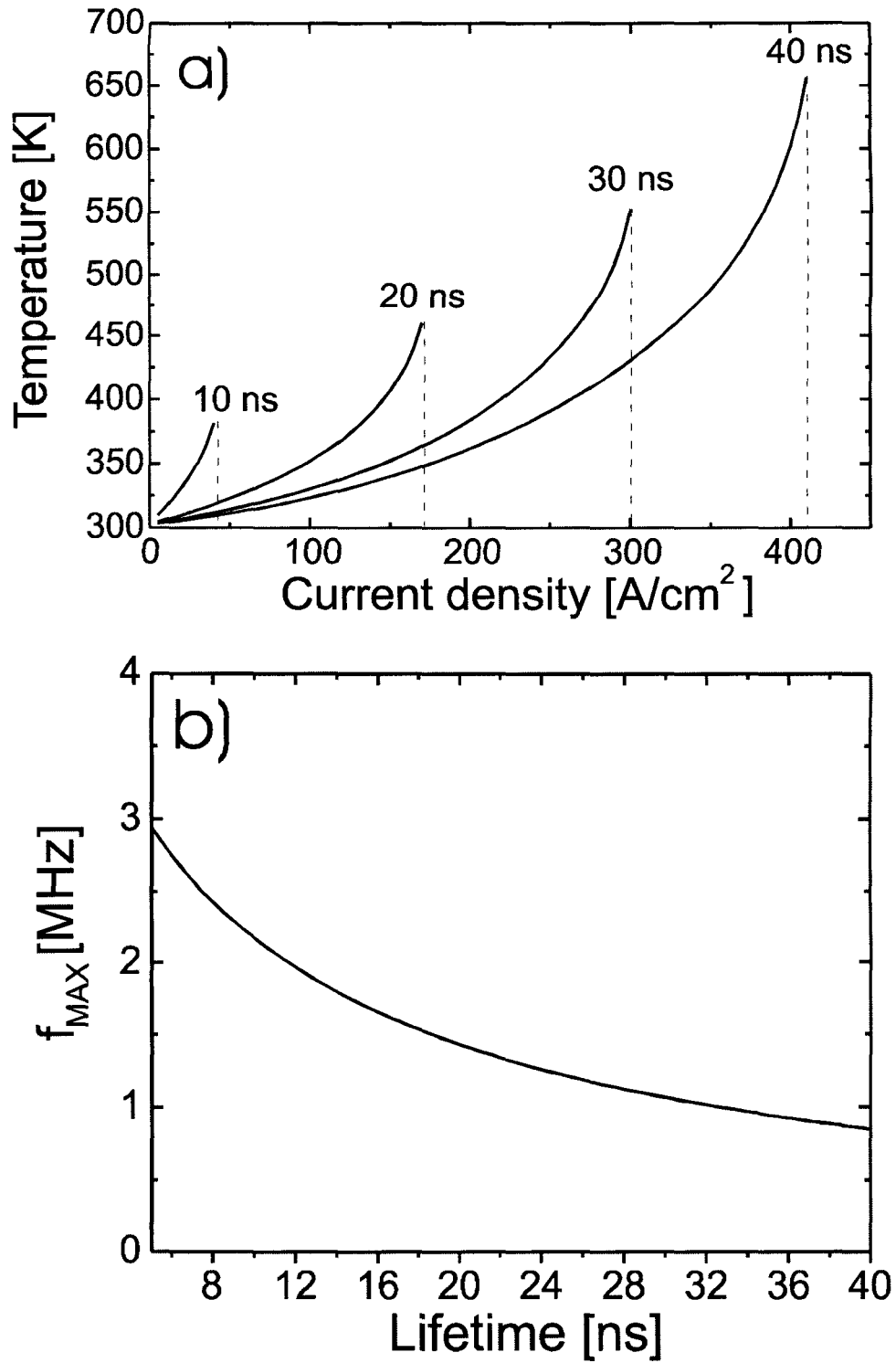


Figure 5.6: a) The relation between the temperature generated in the device and the device current density for different values of the hole recombination lifetime. b) Maximum operating frequency of the thyristor as a function of hole lifetime.

device ($d/\kappa A$) and case to ambient (θ_{ca}) thermal resistivities, where $d \sim 1\text{mm}$ is the substrate thickness. We used values of $\kappa = 1.0\text{ W/K cm}$ for the thermal conductivity, assuming reduction of thermal conductivity at elevated temperatures from a room temperature value of $\kappa_0 = 1.4\text{ W/K cm}$ and $\theta_{ca} = 1\text{ Kcm}^2/\text{W}$ as a typical value for the case to ambient thermal resistivity. Figure 5.6 shows the dependence of the device temperature as a function of current density (obtained from Eqs. 5.8 and 5.9) for several hole lifetimes in the range between 10 and 40 ns, assuming a 50% duty cycle. It can be observed that the maximum current density at a particular hole lifetime is limited by thermal breakdown when power cannot be efficiently dissipated. In the case of the Schottky rectifier even smaller forward voltages of approximately 1 – 2 V are expected, [7] giving smaller power dissipation and much larger maximum current density. We notice that a maximum current density for thyristor in the range of 200 – 400 A/cm² can be expected for measured values of hole lifetime.

5.1.6 Maximum operating frequency for thyristor

Typically, the maximum operating frequency of the thyristor is limited by the forward recovery time, which is the sum of time required to reduce forward conduction current I_f , the time to switch the device from the ON to OFF state, t_{OFF} , and the time needed to increase voltage to the forward blocking voltage V_{BF} : [4]

$$t_{fr} = \frac{I_f}{\left.\frac{dI}{dt}\right|_{max}} + t_{OFF} + \frac{V_{BF}}{\left.\frac{dV}{dt}\right|_{max}}. \quad (5.10)$$

The time taken to turn a device from ON to OFF requires that charges in the standoff layer recombine, and depends on the hole lifetime as $t_{OFF} = \tau_p \ln \frac{I_f}{I_h}$, where I_h is a "hold" current, defined as the current at the low-voltage, low-current end of the negative resistance region in the static $I - V$ characteristic. The value of $\left.\frac{dI}{dt}\right|_{max}$ is determined by the maximum temperature which will appear at the "hot spot" at the cathode because only a small part of the cathode will conduct at the start. [4] We have assumed the value $\left.\frac{dI}{dt}\right|_{max} = 2000\text{ A}/\mu\text{s}$, although larger values could be expected since nitrides have a larger density \times specific heat product than silicon.

The value of $\left.\frac{dV}{dt}\right|_{max}$ is determined by the maximum transient current induced due to the capacitance of the standoff layer. Assuming a standoff layer thickness of a $12\ \mu\text{m}$, we obtain $\left.\frac{dV}{dt}\right|_{max} = 2.7 \cdot 10^{11}\text{V/s}$. Fig. 5.6b shows the maximum operating frequency $f_{max} = 1/2t_{fr}$ of the thyristor with $12\ \mu\text{m}$ -thick AlGaIn standoff layer as a function of the hole lifetime. Much higher operating frequencies can be expected for the Schottky rectifier because it is a unipolar device, where speed is not limited by carrier recombination.

5.2 GaN/AlGaIn heterostructures

Besides large critical field for electric breakdown and good electronic properties, nitride semiconductor system is also attractive because GaN/AlN heterojunctions can be employed. The band alignment between GaN and AlN favors hole injection from AlGaIn into GaN, and this property of the heterojunction system can be used for further device improvements. [14] GaN/AlGaIn heterojunction transistors have been recently fabricated by other groups, but so far poor current gain $\beta \approx 3$ at room temperature have been reported. [15, 16].

5.3 Fabrication of 450 V GaN based Schottky rectifiers

5.3.1 Introduction

In this section, the fabrication of high voltage, GaN based Schottky rectifiers and the measurement of the critical field for electric breakdown is presented. As can be seen in section 5.1, the critical field for electric breakdown is one of the most significant parameters in the design and performance of high power devices. It directly influences the required thickness of the standoff region in the Schottky rectifier and bipolar devices, such as the thyristor. Since the thickness of the standoff region sets forward voltage drop, it will determine power dissipation and maximum current density of the

device (see section 5.1). [12, 13] Schottky diodes have been previously fabricated on GaN using a variety of elemental metals including Pd and Pt, [17, 18], Au, Cr, and Ni, [19, 20], and Mo and W, [21]. More details on the metal-GaN contact technology can be found in Ref. [22].

5.3.2 Fabrication procedures

The Schottky rectifiers were fabricated on $8 - 10 \mu\text{m}$ thick GaN layers grown by HVPE on sapphire, where the electron concentration changes with the distance from the GaN/Sapphire interface. The conductivity and Hall measurements had been carried out on a series of HVPE GaN films of varying thickness ranging from 0.07 to $9.2 \mu\text{m}$, and data had been fitted to a two layer model.[23–26] It was concluded from the model that the GaN films consisted of a low conductivity, low electron concentration, $8 - 10 \mu\text{m}$ thick top layer on a very thin ($< 100\text{nm}$), highly conductive, high electron concentration bottom layer. The electron concentrations and mobilities in the thin interface layer and thick upper layer were $2 \cdot 10^{20} \text{cm}^{-3}$ and $35 \text{cm}^2/\text{Vs}$, and $2 \cdot 10^{16} \text{cm}^{-3}$ and $265 \text{cm}^2/\text{Vs}$ respectively. These values correspond to conductivities of 1120Scm^{-1} and 0.85Scm^{-1} for the interface layer and upper layer, indicating that the interface layer is approximately three orders of magnitude more conductive. C-V measurements performed on the $9.2 \mu\text{m}$ thick samples determined that the net donor concentration in the top few microns of the film was $(2 \pm 1) \cdot 10^{16} \text{cm}^{-3}$, consistent with the two layer model. A cross-sectional transmission electron microscopy (XTEM) study on our HVPE samples (grown under similar conditions) was presented in Ref. [27], where it was concluded that the region adjoining the interface was highly disordered and included large number of subgrain boundaries, stacking faults and prismatic plane faults. Previous XTEM studies on GaN samples grown by HVPE indicated the presence of a similar $100 - 200\text{nm}$ thick, highly defective interface layer. [26, 28] Secondary ion mass spectroscopy studies done on our samples revealed large oxygen impurity concentrations near the GaN/sapphire interface, which also can account for the observed high electron concentration. Therefore, we conclude that the

high electron concentration and low electron mobility at the GaN/sapphire interface are combination of both the observed high defect density and high concentration of impurities (oxygen).

We tested several device and contact geometries including lateral, mesa, and Schottky metal field plate devices as shown in Fig. 5.7 and 5.8. Prior to metal deposition, the GaN surfaces were cleaned with organic solvents, dipped in HF:H₂O (1:10), rinsed in deionized water, and blown dry with nitrogen gas. Following cleaning, gold (1500Å) was sputtered in a Kurt J. Lesker chamber with a background pressure of $2 \cdot 10^{-8}$ Torr and patterned to produce Schottky contacts (see Fig. 5.7 and 5.8). The size of Schottky contacts were 50 μm, 100 μm, and 200 μm. Ti/Al/Ni/Au (150Å/1500Å/100Å/1000Å) was then sputtered to produce ohmic contacts as deposited. On some devices, large area Au metalization was used as a low resistivity contact instead. For the metal field plate devices, SiO₂ was sputtered using SiO₂ targets and 10 sccm of O₂ flow, and then patterned.

Fabrication of mesa devices

The mesa edge termination was produced by chemically assisted ion beam etching, using Xe ions accelerated with 1000 V, and 25 sccm of Cl₂ flow (see Fig. 5.7). [12, 13] We etched 5 μm of the 8 – 10 μm top layer and deposited ohmic contacts closer to the more conductive interface layer (see Fig. 5.7). Figure 5.9a and b shows profile of etched GaN and etch rate as a function of ion beam current. Depending on sample and geometry, the etch rates of up to 0.8 μm/min were found. Figure 5.10 shows SEM micrograph of the 5 μm mesa device.

5.3.3 Current-voltage measurements

The current-voltage (I-V) measurements were taken with a Keithley 237 high voltage source measure unit and with an HP 4156A precision semiconductor parameter analyzer. The Keithley 237 was used for high voltage measurements while the HP 4156A was used to determine the Schottky barrier height and for I-V measurements up to

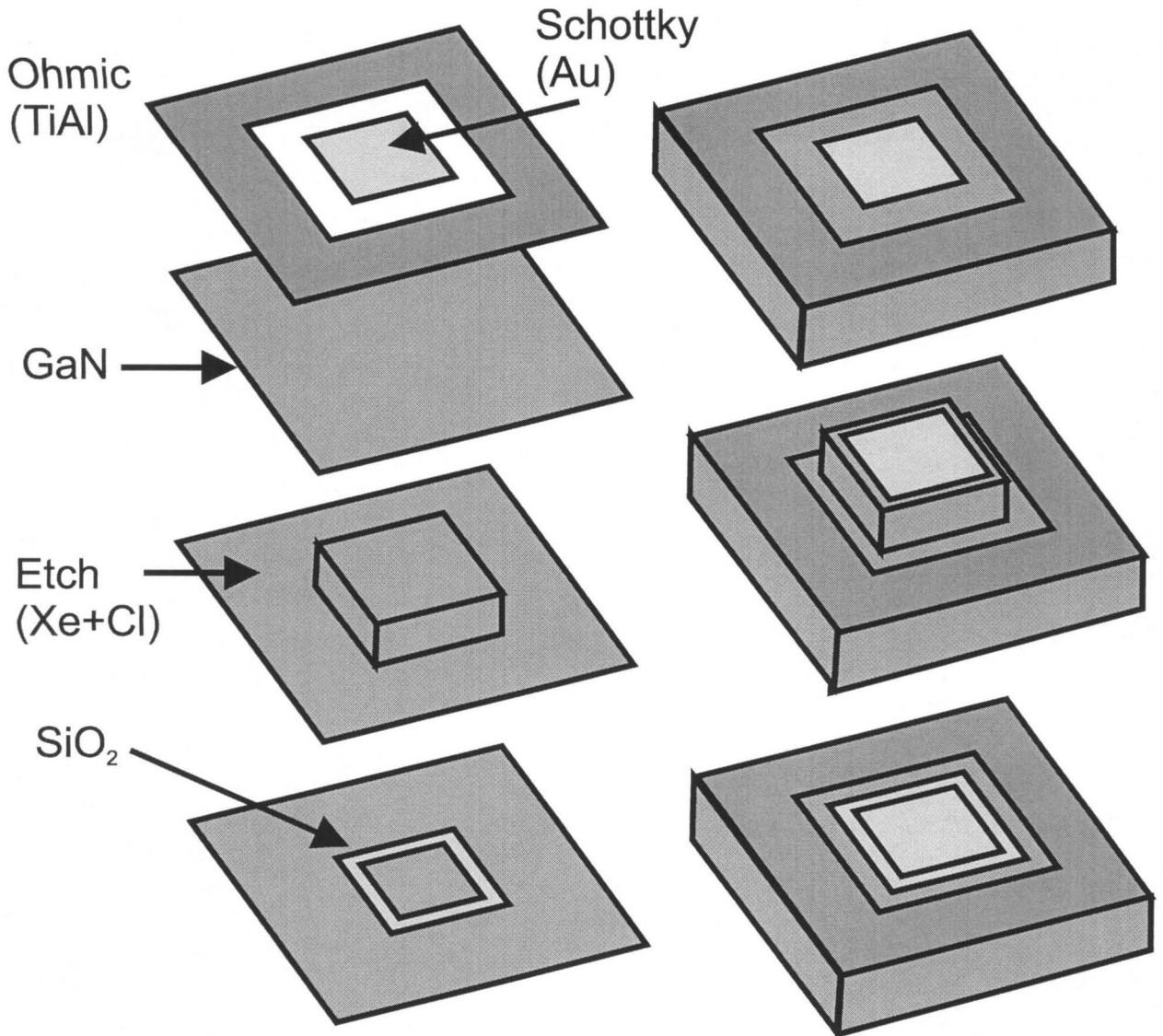


Figure 5.7: Schematic of the Schottky rectifiers processed on the GaN. Schottky and ohmic contacts are fabricated by sputtering and optical lithography. Mesas were defined using chemically assisted ion beam etching.

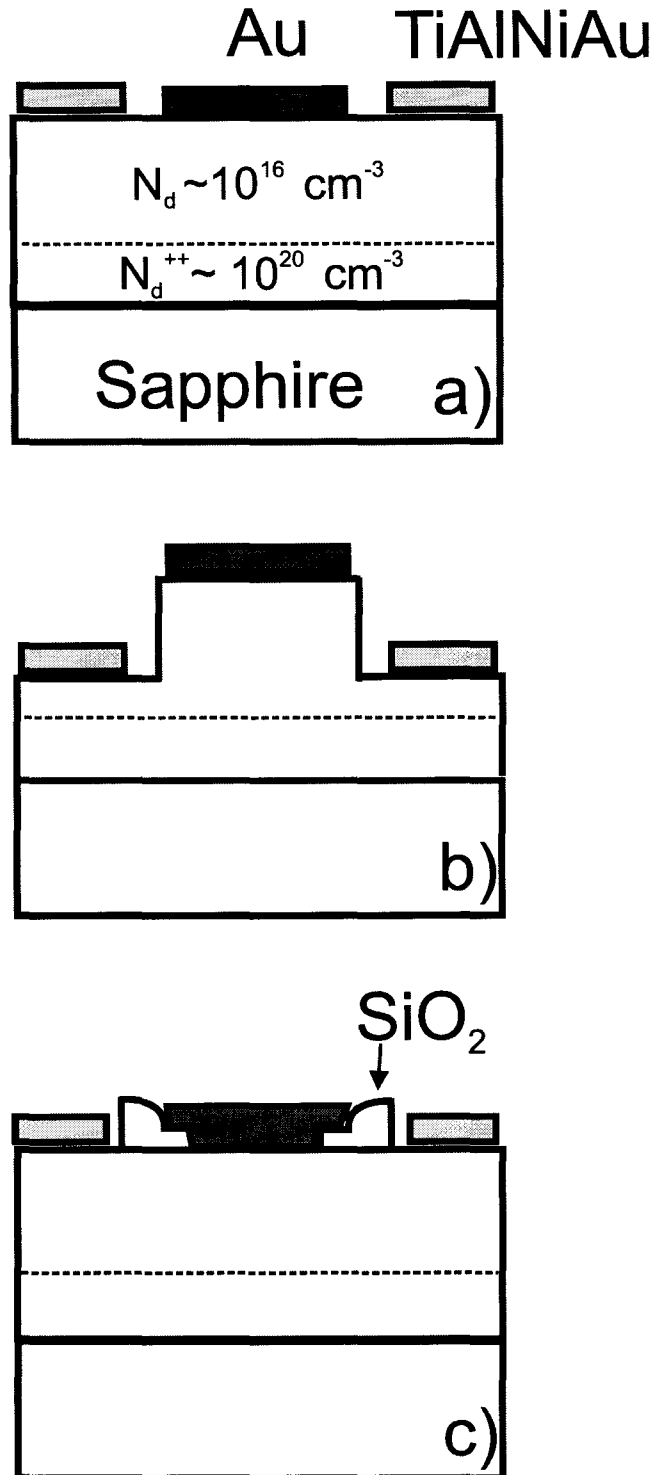


Figure 5.8: Different device geometries for GaN Schottky rectifiers. The thicknesses of the layers of different electron concentration are not drawn to scale. a) Lateral Schottky rectifier b) Mesa device offers lower resistivity since ohmic contacts are deposited closer to the high conductivity interface layer c) Lateral Schottky rectifier processed with Schottky metal field plate overlapping a SiO_2 layer.

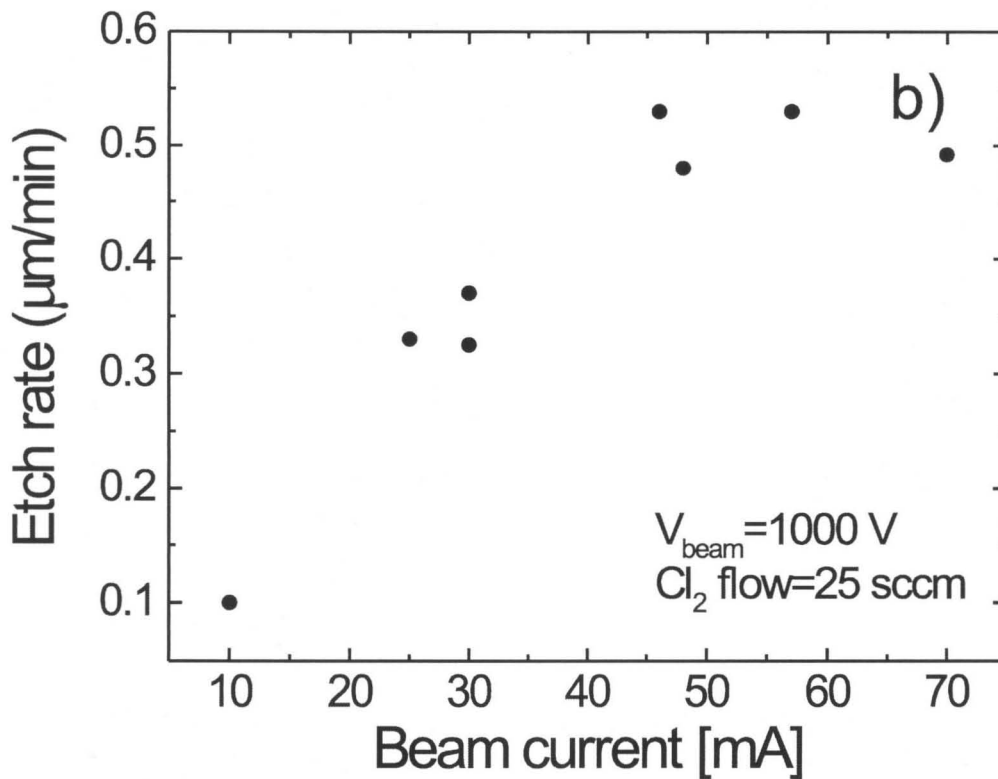
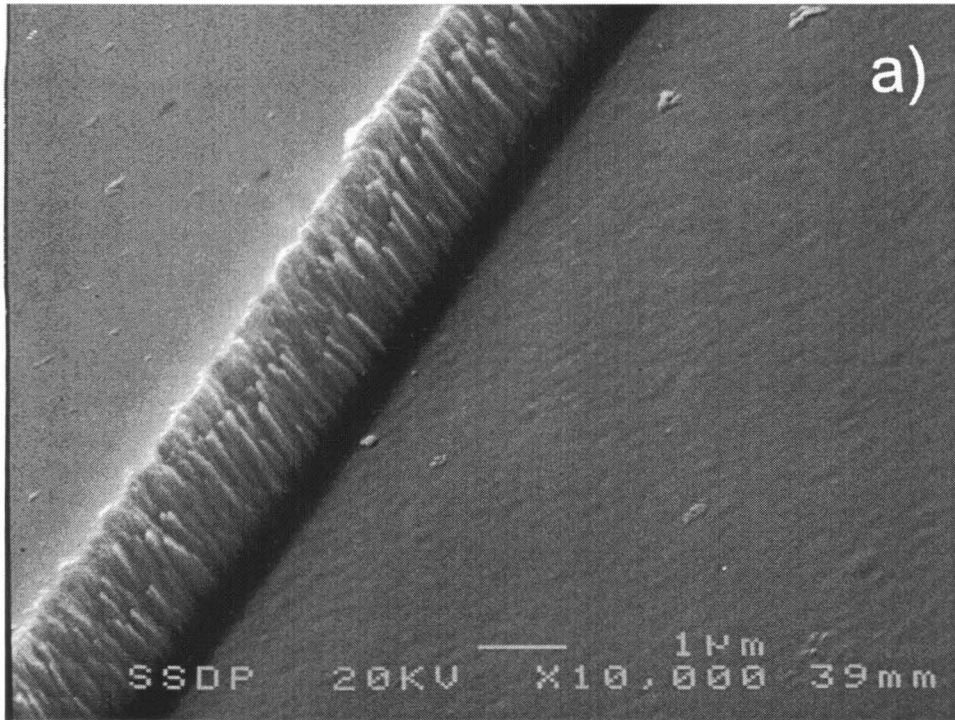


Figure 5.9: a) The SEM micrograph of the profile of the CAIBE etched MOCVD GaN. The 1 KeV Xe ions were used with the 10 sccm flow of Cl_2 . b) Etch rate in case of MBE-grown GaN as a function of electron beam current in case of 1 keV Xe ions and 25 sccm flow of Cl_2 .

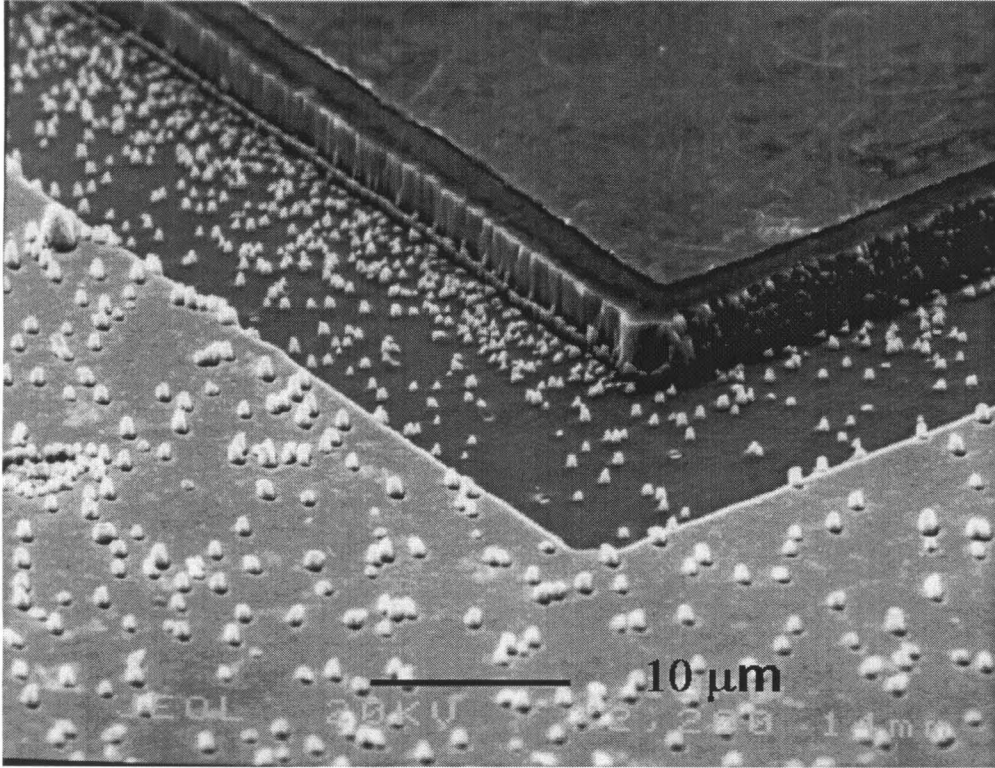


Figure 5.10: The SEM micrograph of the $5\ \mu\text{m}$ mesa device.

100 V. I-V characteristics for the fabricated devices are shown in Figs. 5.11, 5.12 and 5.13. The reverse breakdown voltages observed were in the range between 350 V and 450 V and reached 500 V in several devices (see Fig. 5.12). We associate this variation in the device breakdown voltage with non-uniformities in the electron concentration and surface roughness. The Schottky barrier height Φ_{Au} and ideality n were extracted from measured I-V characteristics by fitting to the Richardson thermionic current equation:

$$I = AA_e T^2 e^{-\frac{q\Phi_{Au}}{kT}} \left(e^{\frac{qV}{nkT}} - 1 \right), \quad (5.11)$$

where A is area of diode, A_e is Richardson constant, T is temperature, k Boltzmann constant, and q unit charge. [4] The Au Schottky barrier heights obtained from the I-V measurements varied between 1.1 eV and 0.8 eV, while the ideality factor of the diodes ranged between 1.6 and 4 (see Fig. 5.14). The Schottky barrier height for gold extrapolated to ideality factor 1 is $\Phi_{Au} = 1.2\ \text{eV}$.

This large variation in ideality of the diodes is attributed largely to the tunneling

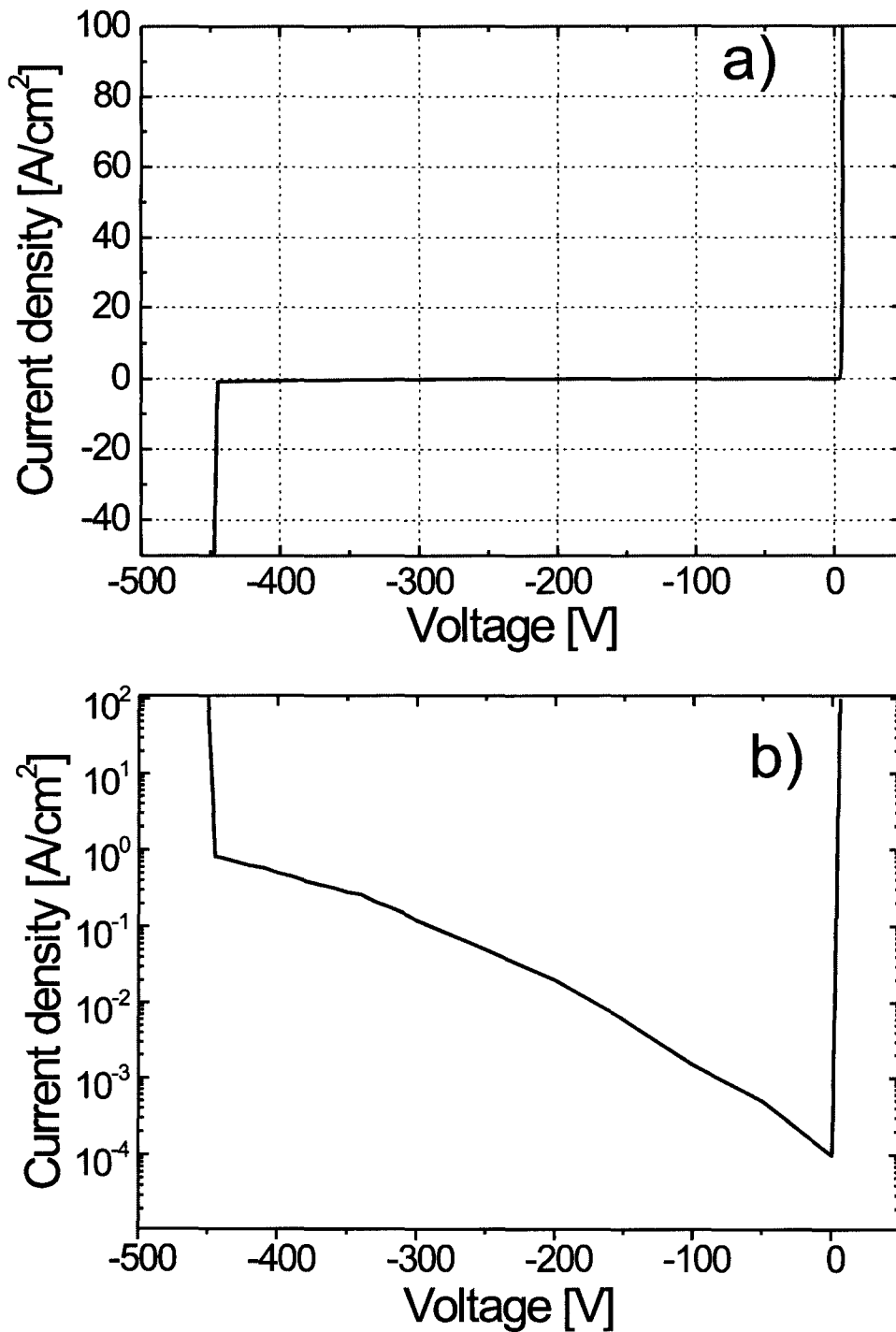


Figure 5.11: a) I-V curve shown on linear scale taken with Keithley 237 high voltage source measure unit for the high voltage rectifier displaying large standoff voltage. b) Same I-V curve shown on logarithmic scale.

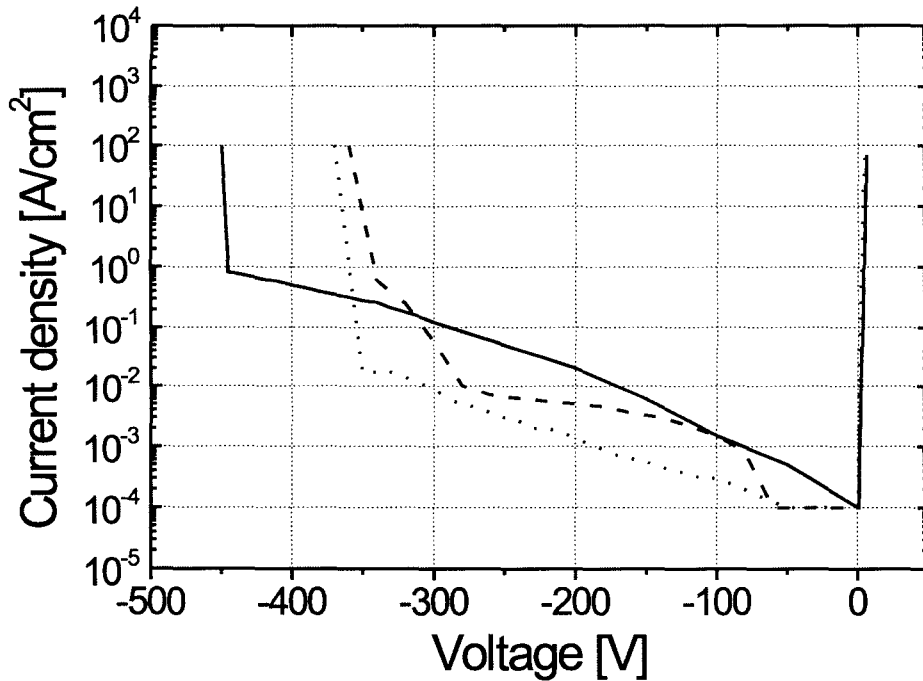


Figure 5.12: I-V curves of three processed devices showing typical variation in breakdown voltage across the chip.

caused by the interface defect states. [29] In the case of the lateral diode, the ON-state voltage was 5–5.5 V for a current density of 100 A/cm² (see Fig. 5.13 and 5.15). Large ON-state voltages are a consequence of both the large ohmic contact resistances and the low electron concentration of the upper layer. The series resistance of the device is significantly affected by the presence of the highly conductive interface layer. This layer “shorts” the conduction path, so that the series resistance consists mainly of the ohmic contact resistance, the resistance of the 8 – 10 μm thick layer between ohmic contact and the highly conductive layer, and the resistance of the 8 – 10 μm thick layer between highly conductive layer and the Schottky contact. Without the highly conductive interface layer, the device series resistance would be determined by the distance between ohmic and Schottky contact. The etching of the top 5 μm layer and the depositing of the ohmic contacts closer to the highly conductive interface layer reduced the ON-state voltage from ≈ 5.5 V to 4.2 V at a forward current density of 100 A/cm² (see Fig. 5.15). However, as can be observed from Fig. 5.13, the reverse leakage current increased to approximately 10⁻² A/cm², probably due to the etch

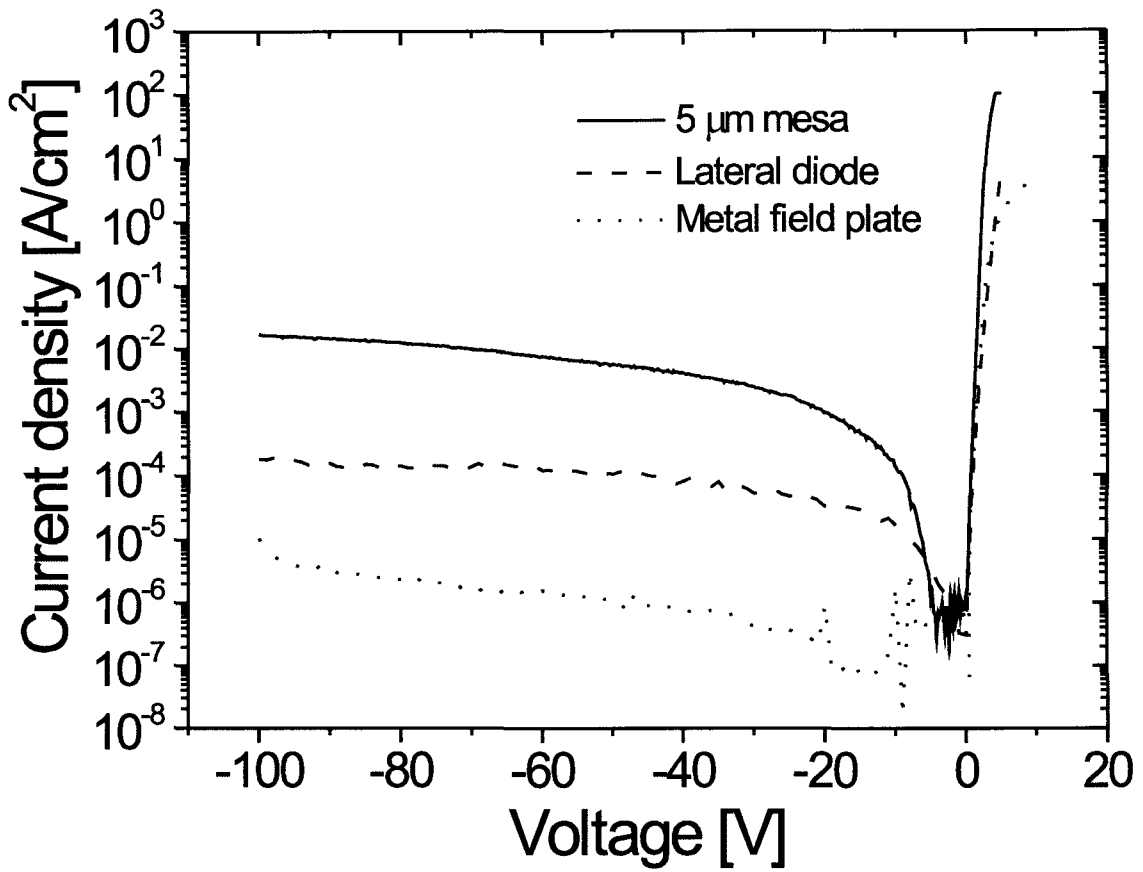


Figure 5.13: I-V curves obtained with HP 4156A precision semiconductor parameter analyzer for the three device geometries discussed above. In all three data sets the Schottky contacts were squares with $100\ \mu\text{m}$ sides.

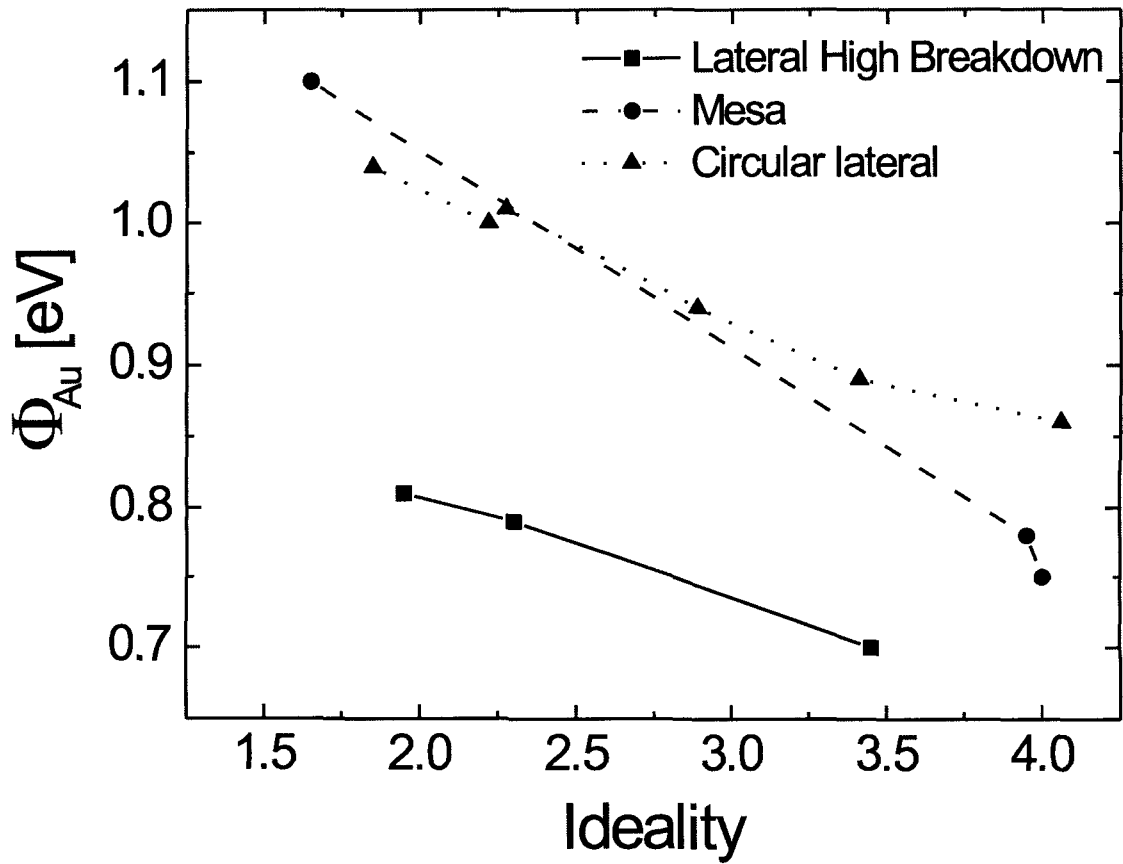


Figure 5.14: Schottky barrier height of gold (Au) on GaN shown as a function of ideality of the contact.

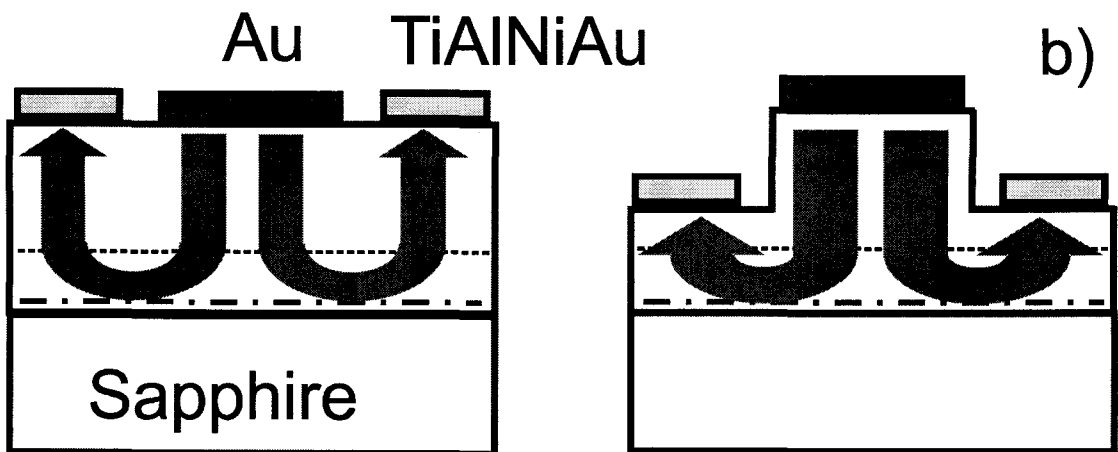
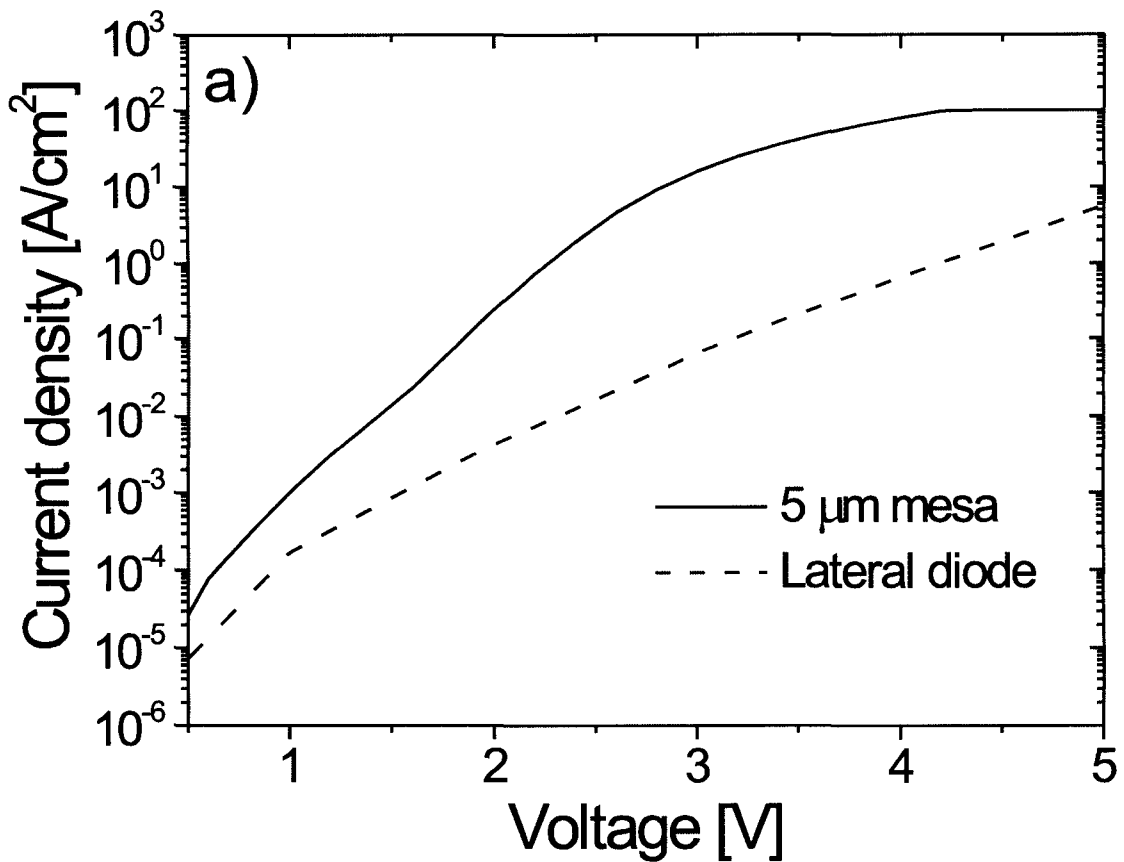


Figure 5.15: a) Forward bias I-V characteristics of devices with different geometries. b) Comparison between current flows in lateral and mesa devices. The highly conductive layer at the interface “shorts” the conduction path, so that mesa device has smaller resistance due to shorter overall current path.

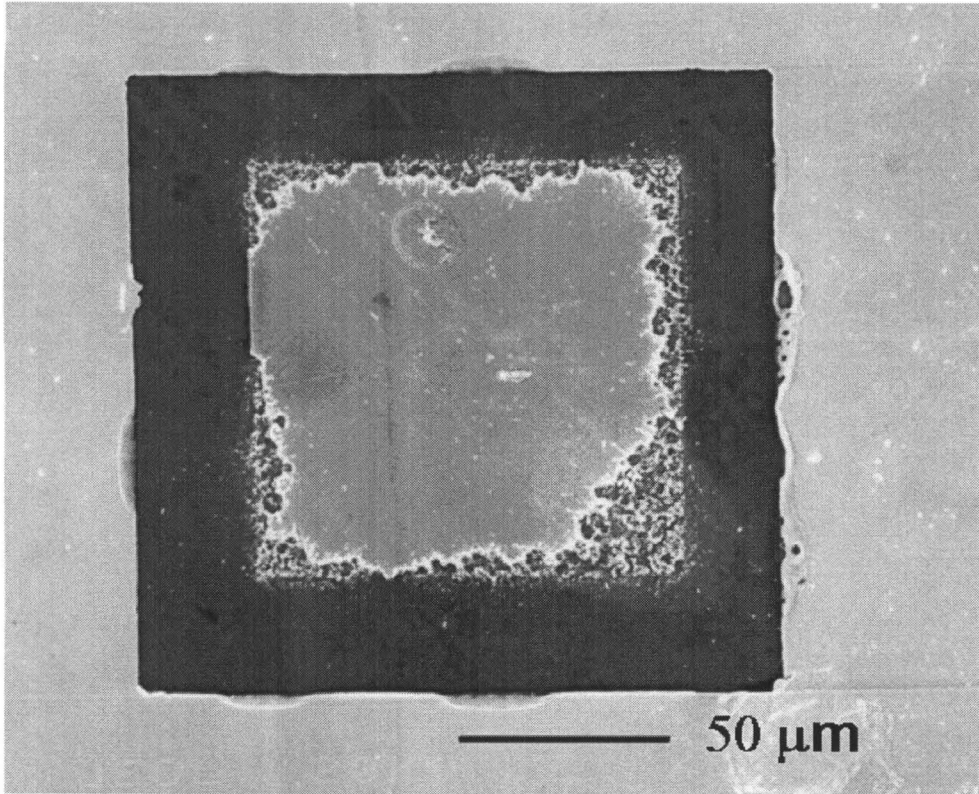


Figure 5.16: SEM photo of the Schottky contact of a diode after breakdown. The melted Au at its edges and corners indicates premature corner and edge breakdown.

damage of the mesa walls.

The electric field crowding at the edges and corners of the Schottky contact would reduce the effective barrier height and increase the reverse leakage current. This can also lead to premature breakdown due to nonuniform current spreading and excessive heating of the device, as can be observed in Fig. 5.16. To improve the Schottky contacts, we fabricated metal field plate contacts using SiO_2 as an insulator. [5] The edge of the Schottky contact overlaps sputtered SiO_2 , thereby reducing electric field crowding at edges and corners. [5] In this case, as can be observed from Fig. 5.13, measured saturation current at a reverse bias of 100 V was less than 10^{-5} A/cm^2 , an improvement of two orders of magnitude when compared to the saturation current density of diodes with lateral contacts.

5.3.4 Experimental determination of the critical field for electric breakdown

In this section we analyze the breakdown voltage of the Schottky diode consisting of lightly doped (N_d) layer of thickness W , at the top of the highly doped bottom layer. As the reverse voltage of the Schottky diode increases, the thickness of the space charge region also increases, as well as the electric field at the metal-semiconductor interface. The thickness of the space charge region is given by $x_{sc} = \sqrt{2\epsilon_0\epsilon_r V_R/qN_d}$. If the thickness W of the standoff layer is larger than the width of the space charge layer at the onset of the breakdown, then the breakdown voltage of the diode is determined from Eq. 5.5:

$$V_{BR} = \frac{\epsilon_0\epsilon_r E_{CR}^2}{2qN_d} \quad (5.12)$$

However, if the doping N_d is low enough, it is possible that the thickness of the space charge region becomes equal to the thickness of the standoff layer, or we have a case of a “punch-through” diode. [5] In that case the breakdown voltage of the diode is given by: [5]

$$V_{PT} = E_{CR}W - \frac{qN_dW^2}{2\epsilon_0\epsilon_r}. \quad (5.13)$$

It is important to consider both cases given by Eq. 5.12 and 5.13, due to the large variation in doping N_d of HVPE GaN material used for fabrication of the Schottky diodes. For example, diodes with low N_d values may be “punched-through” (so Eq. 5.13 should be used), while diodes with higher N_d will obey Eq. 5.12. The breakdown voltage as a function of doping concentration given by Eqs. 5.12 and 5.13 is shown in Fig. 5.17a and b respectively.

From the experimental results, we find the critical field for electric breakdown of $(2.0 \pm 0.5) \cdot 10^6$ V/cm. This value for critical field is in agreement with recent experimental and theoretical predictions. [9, 6] Since our devices suffered from premature corner and edge breakdown (Fig. 5.16), and since device geometries were not fully optimized, we conclude that this value of critical field is only a lower limit.

One of the most important consequences of this study is the experimental demon-

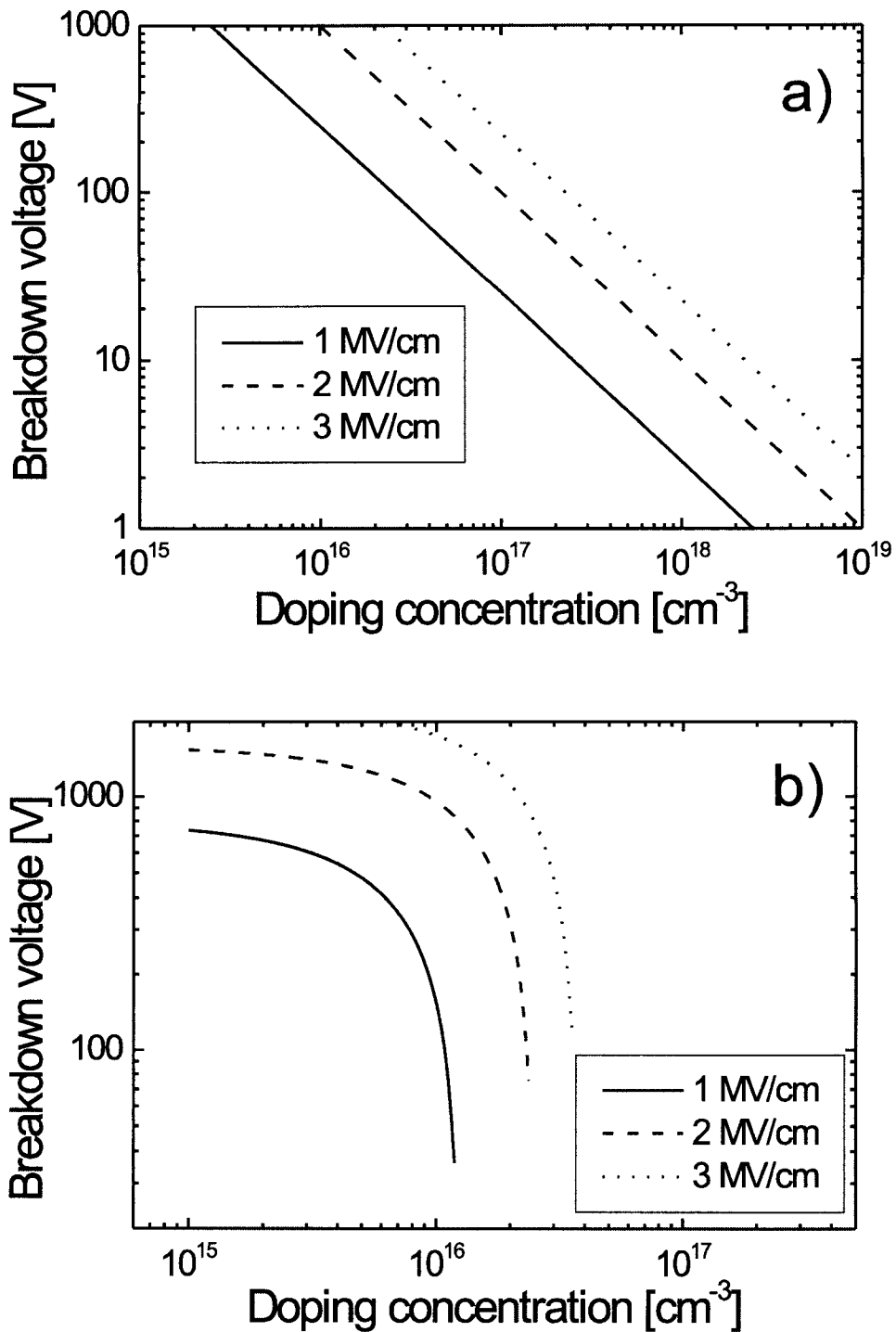


Figure 5.17: a) Breakdown voltage as a function of doping concentration for several values of critical field for electric breakdown. b) The same as a) in the case of “punch-through,” when the standoff layer is fully depleted.

stration of a high critical field for electric breakdown in GaN. A high critical field indicates feasibility of GaN as a material for a variety of unipolar and bipolar devices. [12, 13] Furthermore, assuming that the critical field for electric breakdown approximately scales as the square of the bandgap, even higher critical fields can be expected for AlGaN. The lack of a suitable conductive GaN substrate which can provide large area back ohmic contact, and therefore uniform current spreading, can be circumvented by using highly doped layers underneath the active standoff layer. Although ON-state voltages demonstrated in this work are rather high, estimates based on Eq. 5.11 show that the ON-state voltage for a current density of 100 A/cm^2 can be as low as $1 - 2 \text{ V}$. However, it is necessary to improve Schottky contact edge terminations, reduce ohmic contact resistances and achieve more precise control over doping.

5.4 Fabrication of 750 V GaN Schottky rectifiers

Further improvements in reverse breakdown voltage can be achieved either by thicker, more uniform GaN layers, or by additional improvements in device contact geometry. Figure 5.18 shows $3 \mu\text{m}$ thick GaN layer grown by MOCVD on HVPE GaN layers, nominally identical to the layers described in section 5.3.2. The MOCVD-grown GaN overlayer should provide smoother surface and better metallic contacts, while larger thickness of the sample should allow for larger reverse breakdown voltage.

5.4.1 Fabrication procedures

Fabrication procedures for the 750 V Schottky rectifiers is identical to the fabrication procedures described in section 5.3.2 and Fig. 5.8a. Palladium and Gold were used for Schottky contacts, while $\text{Ti}(200 \text{ \AA})/\text{Al}(1300 \text{ \AA})$ was used for ohmic contacts. In addition to thicker layer, new set of lithography masks were used. In particular, the diameter of circular Schottky contacts varied from $50 \mu\text{m}$ to 1 mm . Rectangular contacts were not used due to the enhanced breakdown at corners. Diodes were also

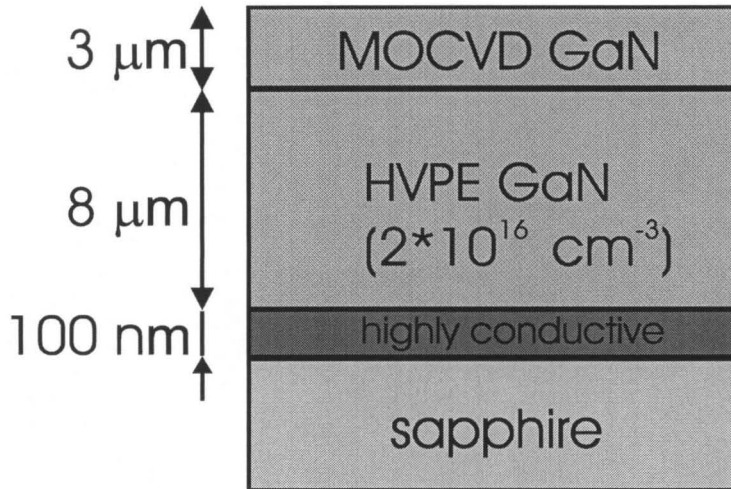


Figure 5.18: Schottky rectifiers with breakdown voltage up to 750 V were fabricated on these layers.

annealed at 700 °C for 60 s to improve properties of TiAl “ohmic” contacts, but no improvement was found as measured by current-voltage characteristics.

5.4.2 Current-voltage characterization

The current-voltage (I-V) measurements were taken with a Keithley 237 high voltage source measure unit and with an HP 4156A precision semiconductor parameter analyzer, similar to the procedures described in section 5.3.3. The reverse breakdown voltage of the Schottky rectifiers fabricated on these thicker MOCVD/HVPE samples was typically in the range between 550 V and 750 V depending on the position on the sample, indicating that uniformity of the sample is not ideal. Figure 5.19 shows current-voltage characteristic of the typical diode in the lateral geometry (see Fig. 5.8a). The reverse breakdown voltage is between 700 V and 750 V. The corresponding critical field for electric breakdown, calculated according to procedures described in section 5.3.4, is $(2.5 \pm 0.5) \cdot 10^6 \text{ V/cm}$. This is additional improvement compared to critical field obtained with the previous set of diodes obtained on HVPE GaN, described in section 5.3. This improvement is associated with lack of corner breakdown effects in circular contact geometry.

The ON-state voltage of the diodes, measured as voltage at current density of

100 A/cm², was between 8 V and 12 V, depending on the position of the diode on the sample. The large ON-state voltage is predominantly the consequence of the poor ohmic contacts. The current density at the reverse voltage of -100 V was typically in the 10⁻³–10⁻⁴ A/cm² range. Although attempts were made to process diodes in other geometries (as described in Fig. 5.8b and c), the results were nonsatisfactory, due to the processing problems. Namely, etching thicker layers was progressively harder with mesa height, due to the problems with the cooling of the sample stage of CAIBE etch chamber. The large process-induced temperature caused baking of the photo-resist which was used as an etch-mask. Baked photo-resist was then virtually impossible to remove. In addition to practical etching problems, TiAl ohmic contacts require larger electron concentration at the surface to become effectively ohmic; otherwise, they behave as “leaky” Schottky contacts. Currently, plans for improvements of etching chamber are under way, as well as plans for selective ion implantation of Si (n-type dopant for GaN) for improved ohmic contacts.

5.5 Fabrication of Schottky diodes on p-type GaN

Schottky diodes on the p-type GaN were fabricated in the course of studies of electron transport properties as a minority carrier. More details about properties of these diodes is given in this chapter, since this chapter focuses on fabrication and characterization of various two-terminal devices. However, Schottky diodes on p-type GaN did not qualify as high power devices since achieved reverse breakdown voltages were low.

5.5.1 Fabrication procedures

The samples used were p-type doped GaN on sapphire grown by MOCVD, and were doped with Mg. Prior to device processing, the GaN surface was cleaned with organic solvents, and then dipped in HF : H₂O(1 : 5). Contact metals were sputtered in a chamber with a background pressure of 2·10⁻⁸ Torr and patterned to produce Schottky contacts as well as large-area ohmic contacts (see Fig. 4.1). Ni/Au metalization

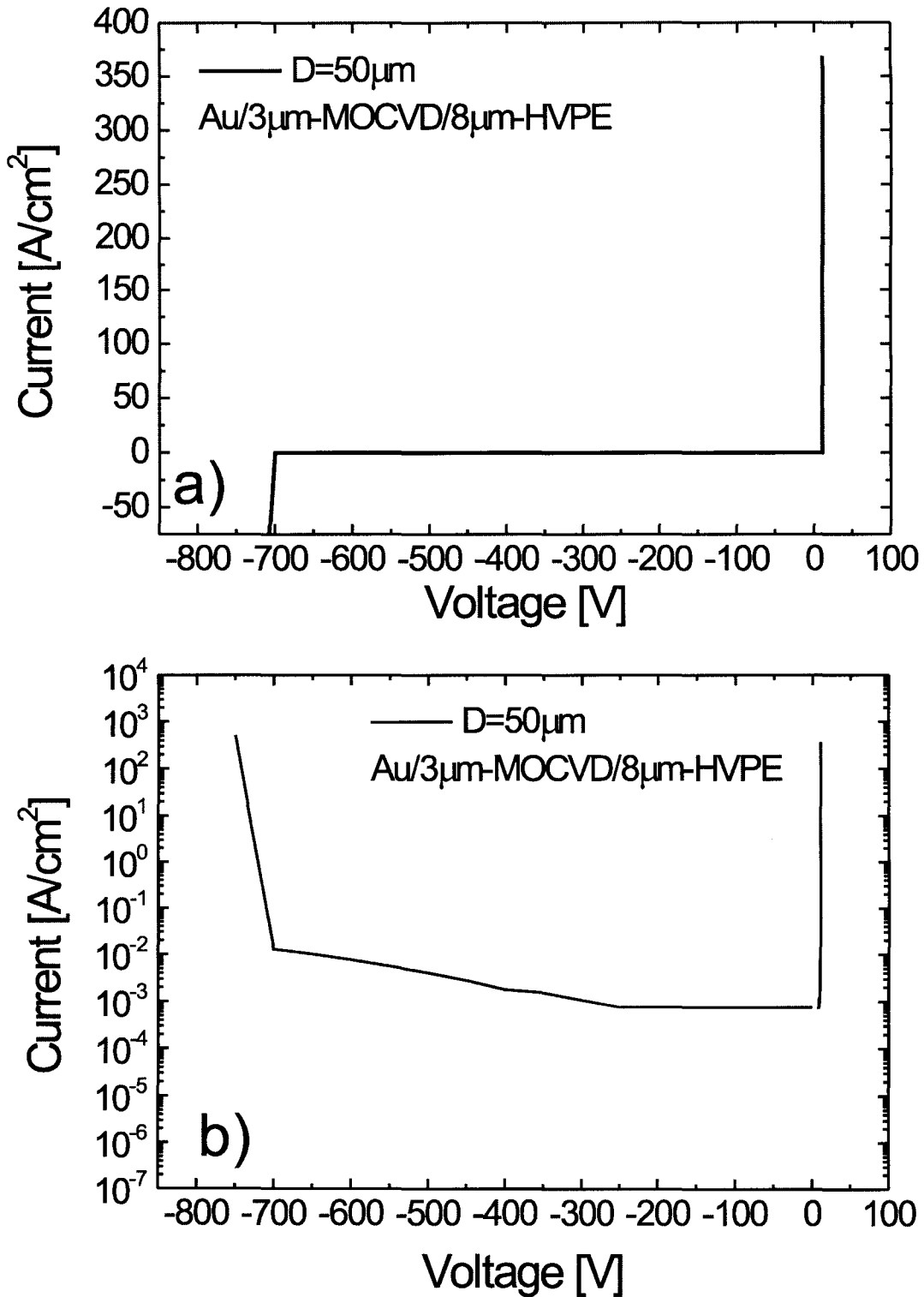


Figure 5.19: Fig. a) shows current on linear scale, while Fig. b) shows current on logarithm scale.

scheme was used for the ohmic contact, while Ti/Au was used for the Schottky contact. The micrograph of fabricated device is shown in Fig. 4.2.

5.5.2 Current-voltage characterization of p-type GaN Schottky diodes

The current-voltage (I-V) measurements were taken with a HP 4156A precision semiconductor parameter analyzer, similar to the procedures described in section 5.3.3. Figure 5.20 shows current voltage characteristics on linear and logarithmic scale. The analysis of the current-voltage characteristics using Eq. 5.11 yields ideality factor $n \approx 6.7$ and a Schottky barrier height for Ti $\Phi_{Bp}^{Ti} \approx 0.8 \text{ eV}$. Since the reported barrier heights of Ti on n-type GaN range from approximately 0.1 eV to 0.6 eV, [30] we may observe that for Ti we would expect $\Phi_{Bp} = 3.4 \text{ eV} - \Phi_{Bn} \approx 2.8 \text{ eV}$ which is much larger than experimentally observed value of 0.8 eV. This discrepancy can be partially accounted for by tunneling of holes through the very thin barrier formed at the contact due to the high Mg acceptor concentration necessary to achieve p-type doping, and due to the image force lowering of this barrier. The large ideality of the diodes, which we measured to be approximately 6.7, supports the hypothesis of the hole tunneling. Figure 5.21 shows the band diagram of the p-type GaN/Schottky metal contact. The large concentration of the Mg atoms produces very thin barrier of the height Φ_{Bp} . The tunneling through this barrier can be a very effective way to transport holes through this interface, which would significantly increase the total current, and apparently reduce barrier height measured from Eq. 5.11. The expression for tunneling probability is given by: [4]

$$T(E) = \exp\left[\frac{2}{\hbar} \sqrt{\frac{\epsilon_0 \epsilon_r m_v}{N_a}} (E - \Phi_{Bp})\right], \quad (5.14)$$

where \hbar is Planck constant, ϵ_r is dielectric constant, m_v is hole effective mass in GaN, N_a is acceptor concentration, Φ_{Bp} is ideal Schottky barrier height, and E is hole energy. If we assume that tunneling becomes unimportant at energy E^* , where

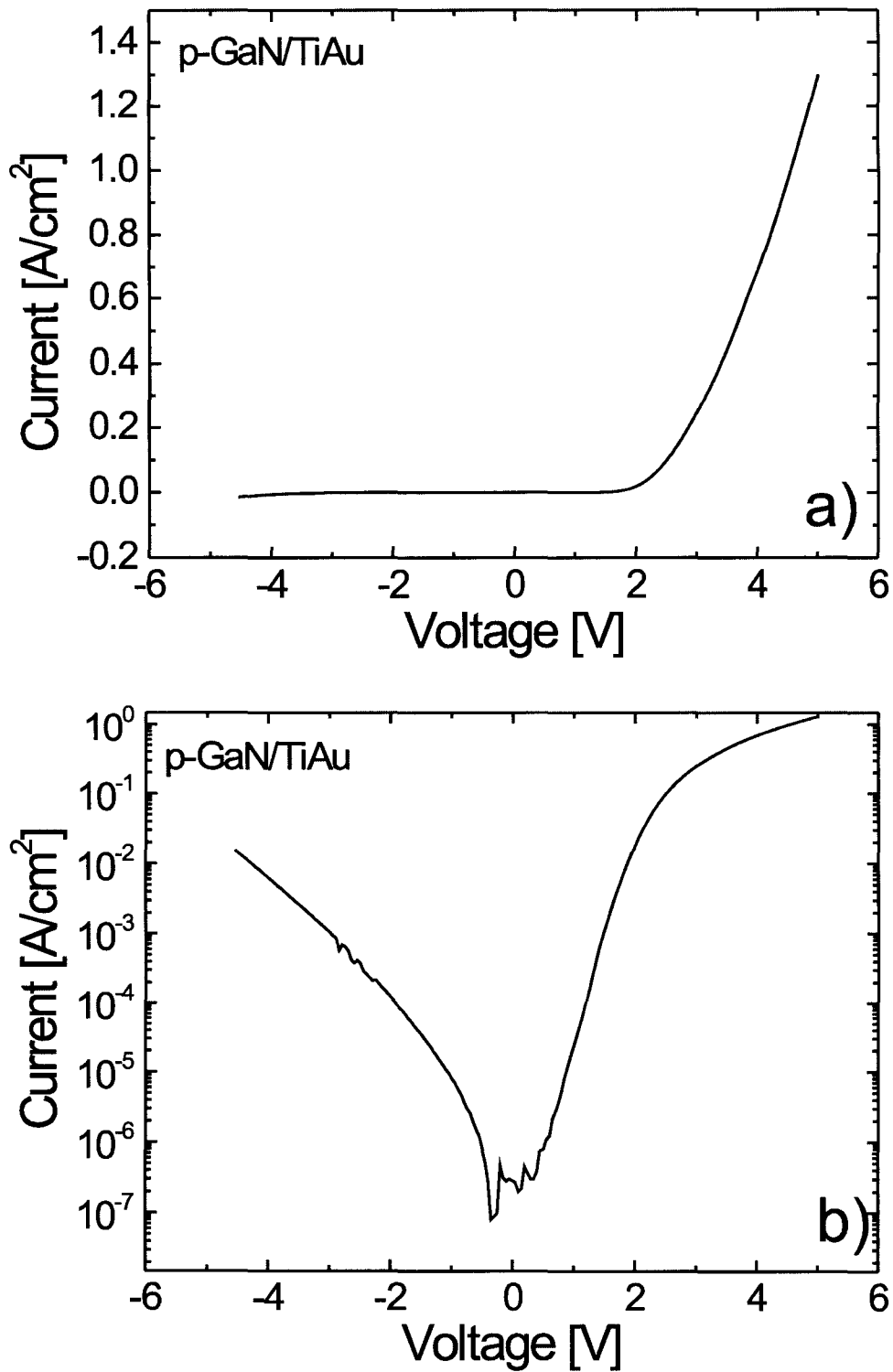


Figure 5.20: Fig. a) shows current on linear scale, while Fig. b) shows current on logarithm scale.

$T(E^*) = 10^{-3}$, then from Eq. 5.14 we obtain the corresponding reduction in effective barrier height:

$$\Delta\Phi_{Bp} = \frac{6.9\hbar}{2} \sqrt{\left(\frac{N_a}{\epsilon_0\epsilon_r m_v}\right)}. \quad (5.15)$$

By replacing $N_a = 10^{20} \text{ cm}^{-3}$ and $m_v \approx 1m_e$ in the Eq. 5.15, we obtain that the reduction of the apparent barrier height due to tunneling can be as much as 1.2 eV. Although this reduction is still not large enough to fully explain the experimentally observed reduction of 2 eV, it is probably one of the most important factors. Another important mechanism for the reduced barrier height might also be the image-force lowering. [4]

The main reason for low reverse breakdown voltages (10 V) achieved in these diodes was small thickness of diodes, and “soft” reverse breakdown caused by tunneling through thin barrier formed at metal-semiconductor interface.

5.6 Conclusion

The important advantage of nitrides and other wide band gap materials for high power devices is a smaller standoff layer thickness for the same standoff voltage, giving smaller ON-state voltage and resistance, smaller power dissipation and larger maximum current density, allowing physically smaller devices for the same power rating. The design rules for nitride based Schottky rectifiers and thyristors are presented. The important design parameters are critical electric field and hole recombination lifetime. Using modeling parameters in the range currently available with GaN, and measured from fabricated devices, design results indicate the possibility of 18 μm thick GaN Schottky rectifiers and 12 μm thick AlGaIn thyristors supporting 5 kV standoff voltage. The theoretical studies indicate that critical field for electric breakdown in GaN is approximately 5 MV/cm. The maximum current density for 5 kV thyristors is in the 200 – 400 A/cm² range depending on the hole lifetime, and is limited by thermal breakdown. The maximum operating frequency of 5 kV thyristors is in the 1-2 MHz range, also depending on the hole lifetime.

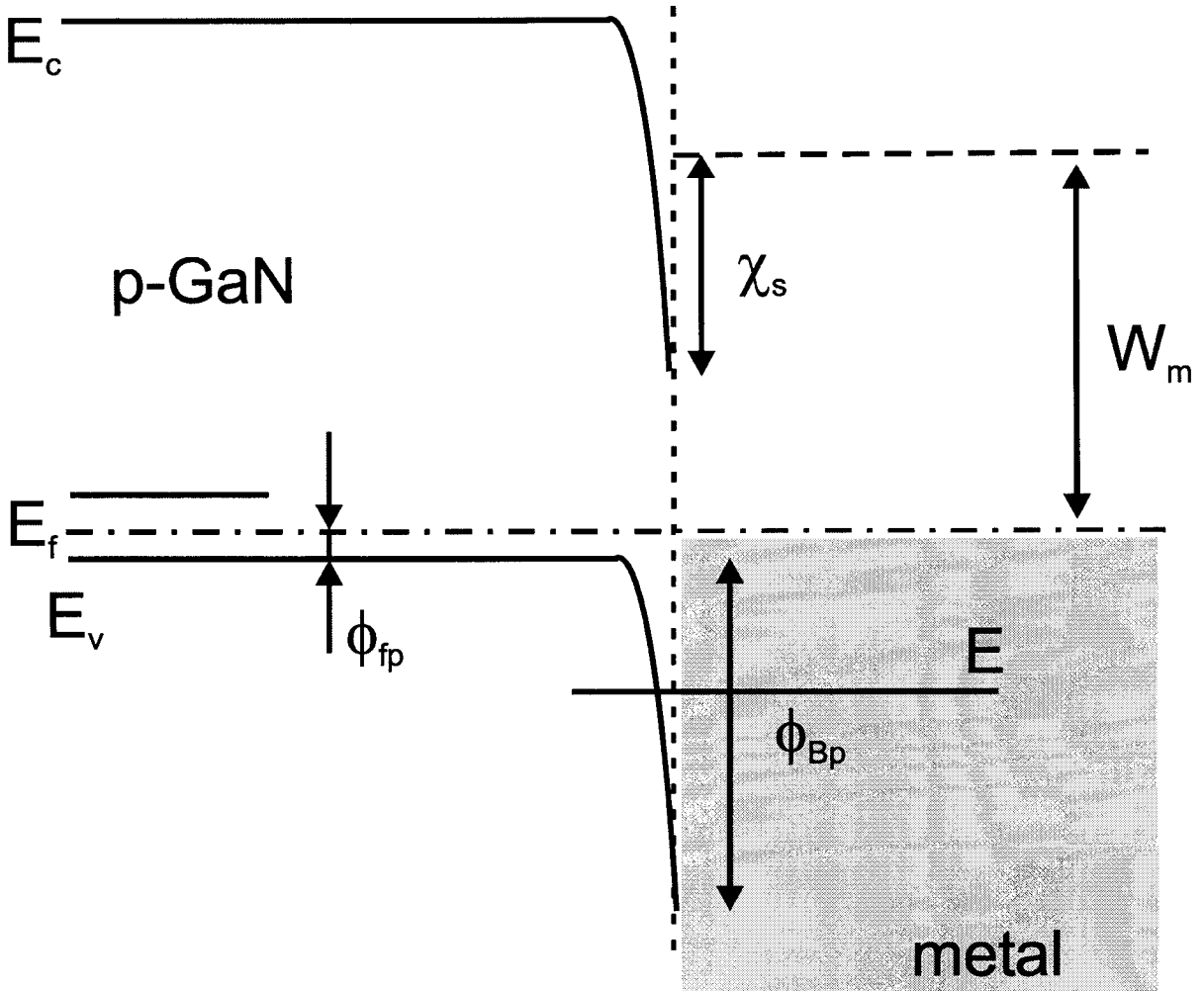


Figure 5.21: E_c and E_v are bottom of the conduction and top of the valence band in GaN, E_f is the position of the Fermi level, Φ_{fp} is Fermi level position in respect to the top of the valence band, Φ_{Bp} is the Schottky barrier height, W_m is the metal work function, and χ_s is electron affinity in GaN. The large concentration of the Mg acceptors required in GaN to produce p-type doping makes very thin barrier at the interface. The tunneling transport therefore dominates over thermoelectronic emission and effectively reduces barrier height.

The Schottky rectifiers were fabricated on 8 – 10 μm -thick HVPE-grown GaN which had a standoff voltage of 450 V, a minimum saturation current density of 10^{-5} A/cm² at reverse bias of 100 V, and 4.2 V ON-state voltage at a forward current density of 100 A/cm². Various contact geometries were investigated. It was found that mesa geometry improves ON-state voltage, but causes increase in reverse current density, while that metal field plate geometry significantly reduces reverse current density. The critical field for electric breakdown measured for GaN is $(2.0 \pm 0.5) \cdot 10^6$ V/cm which approaches the theoretical estimate. Additional set of Schottky rectifiers were fabricated on 3 μm -thick UID GaN layers grown on the 8 – 10 μm -thick HVPE layers. These diodes were fabricated using only circular Schottky contact geometry, which eliminates corner breakdown effects. The improvements in film uniformity and contact geometry resulted in improved reverse breakdown voltage of 750 V, and improved critical field of $(2.5 \pm 0.5) \cdot 10^6$ V/cm. However, the ON-state voltage also increased to 10 – 12 V, mainly due to the poor TiAl ohmic contacts to n-type GaN. The measured values of critical field are only a lower limit since the reverse breakdown voltage was limited by premature corner and edge breakdown.

The results on fabrication and characterization of Schottky diodes on p-type GaN are also presented. The Schottky barrier height of approximately 0.8 eV was found. The tunneling through thin barrier formed at the metal-semiconductor interface was identified as primary cause for reduction of barrier height and small reverse breakdown.

Bibliography

- [1] Taylor Moore, *Beyond silicon: Advanced Power Electronics*, Epri Journal, (Nov/Dec 1997).
- [2] N.R. Perkins, M.N. Horton, Z.Z. Bandić, T.C. McGill, and T.F. Kuech, *Mat. Res. Soc. Symp. Proc.* **395**, 243 (1996).
- [3] Dan Kinzer, International Rectifier, private communication.
- [4] S. Sze, *Semiconductor Devices* (John Wiley & Sons, New York, 1981).
- [5] B.J. Baliga, *Power Semiconductor Devices* (PWS, Boston, 1996.)
- [6] J. Kolnik, I.H. Ogusman, K.F. Brennan, R. Wang, and P.P. Ruden, *J. Appl. Phys.* **82**, 726 (1997).
- [7] Z. Z. Bandić, P. M. Bridger, E. C. Piquette, R.A. Beach, V. M. Phanse, R. P. Vaudo, J. Redwing, and T. C. McGill, *Mat. Res. Soc. Symp. Proc.* **512**, 27 (1998).
- [8] Z. Z. Bandić, P. M. Bridger, E. C. Piquette, T.C. McGill, R. P. Vaudo, V. M. Phanse, and J. Redwing, *Appl. Phys. Lett.* **74**, 1266 (1999).
- [9] N. Dyakonova, A. Dickens, M. Shur, R. Gaska, and J.W. Yang, *Appl. Phys. Lett.* **72**, 2562 (1998).
- [10] T.P. Chow and R. Tyagi, *IEEE Trans. Electron Devices* **41**, 1481 (1994).
- [11] M.S. Shur, A. Khan, B. Gelmont, R.J. Trew, M.W. Shin, *Inst. Phys. Conf. Ser.* **141**, 419 (1995).
- [12] Z.Z. Bandić, P.M. Bridger, E.C. Piquette, T.F. Kuech, and T.C. McGill, *Mat. Res. Soc. Symp. Proc.* **483**, 399 (1998).

- [13] Z.Z. Bandić, E.C. Piquette, P.M. Bridger, R.A. Beach, T.F. Kuech, and T.C. McGill, *Solid State Electron.* **42**, 2289 (1998).
- [14] Patent pending "High power devices based on Gallium Nitride and Aluminum Gallium Nitride semiconductor heterostructures," by Z.Z. Bandić, E.C. Piquette and T.C. McGill.
- [15] L.S. McCarthy, P. Kozodoy, S.P. DenBaars, M. Rodwell, and U.K. Mishra, 25th Int. Symp. Compound Semicond., Oct. 1998., Nara, Japan.
- [16] F. Ren *et al.*, *MRS Internet J. Nitride Semicond. Res.* **3**, 41 (1998).
- [17] L. Wang, M.I. Nathan, T.H. Lim, M.A. Khan, and Q. Chen, *Appl. Phys. Lett.* **68**, 1267 (1996).
- [18] S.N. Mohammad, Z. Fan, A.E. Botchkarev, W. Kim, O. Aktas, A. Salvador, and H. Morkoc, *Electron. Lett.* **32**, 598 (1996).
- [19] E.V. Kalinina, N.I. Kuznetsov, V.A. Dmitriev, K.G. Irvine, and C.H. Carter, Jr., *Journal of Electron. Mater.* **25**, 831 (1998).
- [20] P. Hacke, T. Detchprohm, K. Hiramatsu, and N. Sawaki, *Appl. Phys. Lett.* **63**, 2676 (1993).
- [21] E. C. Piquette, Z. Z. Bandić, and T. C. McGill, *Mat. Res. Soc. Symp. Proc.* **482**, 1089 (1998).
- [22] Q.Z. Liu and S.S. Lau, *Solid State Electron.* **42**, 677 (1998) and references cited therein.
- [23] R.P. Vaudo, V.M. Phanse, M.C. Cattrel, and J.M. Redwing, 2nd Intl. Conf. on Nitride Semiconductors, Tokushima, Japan (1997).
- [24] D.C. Look, *Electrical Characterization of GaAs Materials and Devices* (Wiley, New York, 1989).
- [25] D.C. Look and R.J. Molnar, *Appl. Phys. Lett.* **70**, 3377 (1997).

- [26] W. Götz, J. Walker, L.T. Romano, N.M. Johnson, and R.J. Molnar, *Mater. Res. Soc. Symp. Proc.* **449**, 525 (1997).
- [27] Y. Golan, X.H. Wu, J.S. Speck, R.P. Vaudo, and V.M. Phanse, *Appl. Phys. Lett.* **73**, 3090 (1998).
- [28] W.Götz, L.T. Romano, B.S. Krusor, N.M. Johnson, and R.J. Molnar, *Appl. Phys. Lett.* **69**, 242 (1996).
- [29] L.S. Yu, Q.Z. Liu, Q.J. Xing, D.J. Qiao, S.S. Lau, and J. Redwing, *J. Appl. Phys.* **84**, 2099 (1998).
- [30] J.D. Guo, C.I. Lin, M.S. Feng, F.M. Pan, G.C. Chi, and C.T. Lee, *Appl. Phys. Lett.* **68**, 235 (1996); see also S.C. Binari, H.B. Dietrich, G. Kelner, L.B. Rowland, K. Doverspike, and D.K. Gaskill, *Electr. Lett.* **30**, 909 (1994).

Appendix A Simple model for electron beam induced current near Schottky diode in planar geometry

The purpose of this appendix is to derive approximate expression for the electron beam induced current (EBIC) if the current is collected by the Schottky diode in the planar geometry. The case of infinite surface recombination is chosen due to analytic simplicity. [1] The case of finite surface recombination requires more detailed treatment, although the main conclusions about EBIC are similar.[2]

If electron beam is injected at the distance d from the edge of the Schottky contact in the planar geometry (see Fig. A.1), generation volume of electron-hole pairs of radius h will be generated inside the sample. In the further treatment, the generation volume is replaced by point source $g_0\delta(\vec{r}-\vec{r}_0)$, at the depth h below the surface, where $\vec{r}_0 = h\vec{e}_z = 0\vec{e}_z'$ for simplicity. The differential equation governing the distribution of minority carriers $p(\vec{r})$ is:

$$D_p\nabla^2 p(\vec{r}) - \frac{p(\vec{r})}{\tau(\vec{r})} + g(\vec{r}) = \frac{\partial p(\vec{r})}{\partial t} \quad (\text{A.1})$$

where $g(\vec{r}) = g_0\delta(\vec{r}-\vec{r}_0)$, D_p is diffusivity and $\tau(\vec{r}) = \tau_p$ is minority carrier lifetime. In the steady state $\frac{\partial p(\vec{r})}{\partial t} = 0$, so that Eq. A.1 reduces to:

$$D_p\nabla^2 p(\vec{r}) - \frac{p(\vec{r})}{\tau_p} + g_0\delta(\vec{r}-\vec{r}_0) = 0. \quad (\text{A.2})$$

If we change coordinate system from (x, y, z) to (x', y', z') , Eq. A.2 becomes:

$$D_p\nabla^2 p(\vec{r}') - \frac{p(\vec{r}')}{\tau_p} + g_0\delta(\vec{r}') = 0. \quad (\text{A.3})$$

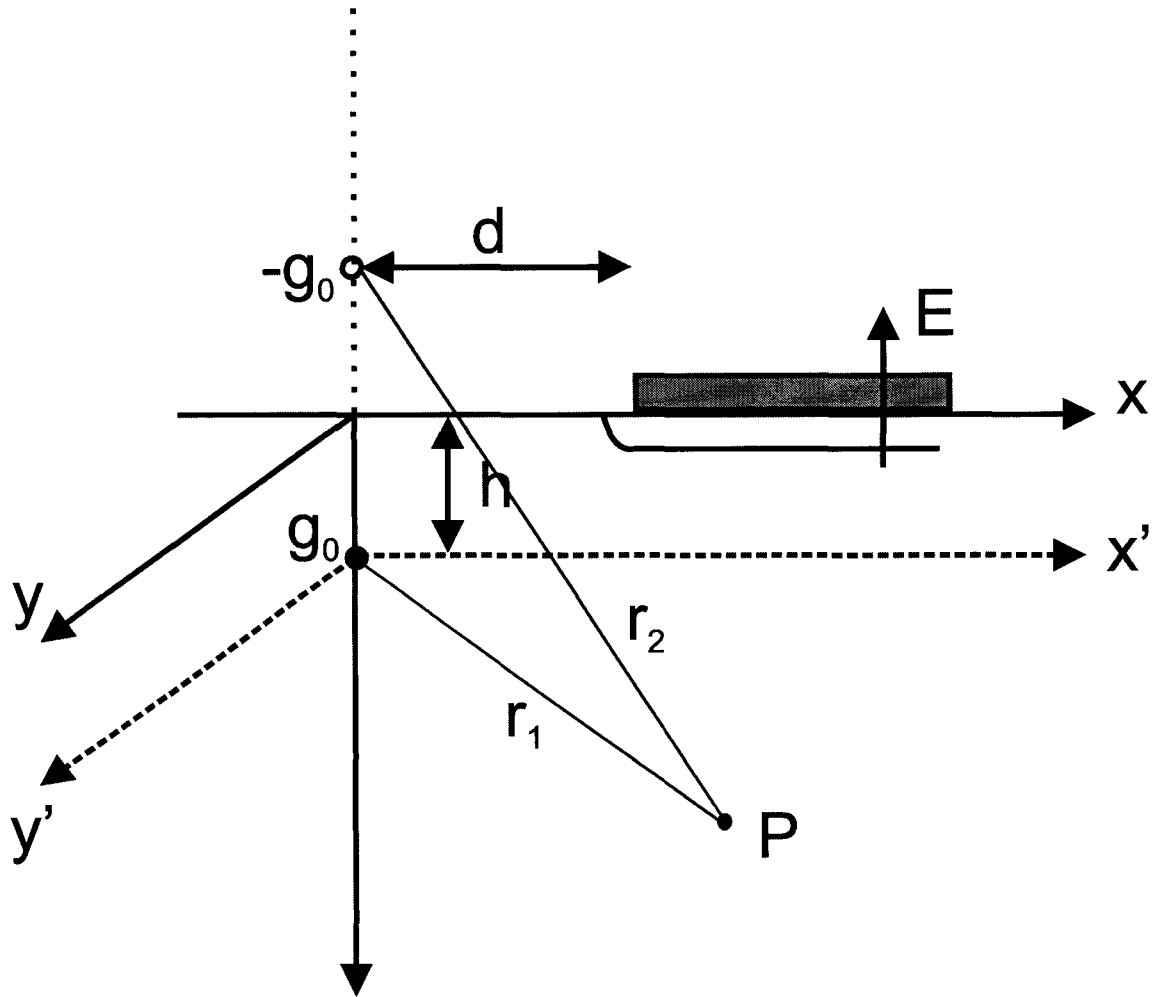


Figure A.1: Schematic of the Schottky diode in the planar geometry. The point source generation (g_0) at depth h below the surface is assumed. Depth h is determined by the electron energy. In the case of the infinite surface recombination, the effect of surface can be treated by mirror image of the opposite charge generation ($-g_0$) at height h above the surface.

One solution of the Eq. A.3 is:

$$p(\vec{r}') = \frac{g_0}{4\pi D_p} \frac{e^{-|\vec{r}'|/L_p}}{|\vec{r}'|} \quad (\text{A.4})$$

where $L_p = (D_p \tau_p)^{1/2}$ is the minority carrier diffusion length. However, the solution of Eq. A.3 has to satisfy boundary condition for infinite surface recombination:

$$s = \frac{\Delta p}{D_p} \frac{\partial(\Delta p)}{\partial z} \Big|_{z=0, z'=h} \rightarrow \infty. \quad (\text{A.5})$$

The condition A.5 is satisfied if $\Delta p = 0$ at surface ($z = 0$ or $z' = h$).

One possible solution of Eq. A.3 which will satisfy boundary condition A.5 is:

$$\Delta p = \frac{g_0}{4\pi D_p} \left[\frac{e^{-r_1/L_p}}{r_1} - \frac{e^{-r_2/L_p}}{r_2} \right] \quad (\text{A.6})$$

This solution is obtained as a linear combination of solutions given by Eq. A.4 for the original point source $g_0 \delta(\vec{r} - \vec{r}_0)$ (at the distance h below the surface) and the mirror image of opposite charge $-g_0 \delta(\vec{r} - \vec{r}_0)$ (at the distance h above the surface). Δp is minority carrier concentration at point P, which is at distance r_1 from the original point source, and distance r_2 from the mirror image point source. Distances r_1 and r_2 are given by:

$$r_{1,2} = \left[x^2 + y^2 + (z \mp h)^2 \right]^{1/2} \quad (\text{A.7})$$

Minority carriers are collected by the electric field at the Schottky contact and they form electric current:

$$J = q D_p \int_{x=d}^{+\infty} \int_{y=-\infty}^{+\infty} \frac{\partial(\Delta p)}{\partial z} \Big|_{z=0} dx dy. \quad (\text{A.8})$$

If we introduce dimensionless quantities:

$$X = x/L_p, Y = y/L_p, Z = z/L_p, D_s = d/L_p, H = h/L_p, R = r/L_p \quad (\text{A.9})$$

where $r = (x^2 + y^2 + z^2)^{1/2}$, then the Eq. A.8 becomes:

$$\frac{2\pi J}{qg_0} = \frac{\partial}{\partial Z} \Big|_{Z=-H} \int_{D_s}^{+\infty} \int_{-\infty}^{+\infty} \frac{e^{-R}}{R} dXdY, \quad (\text{A.10})$$

where $R = (X^2 + Y^2 + Z^2)^{1/2}$. The second integral becomes:[3]

$$\int_{-\infty}^{+\infty} \frac{e^{-\sqrt{X^2+Y^2+Z^2}}}{\sqrt{X^2+Y^2+Z^2}} dY = 2K_0(\sqrt{X^2+Z^2}) \quad (\text{A.11})$$

where K_0 is modified Bessel function of the second order. By using Eq. A.11 and $K'_0 = K_1$, [3] we can transform Eq. A.10 to:

$$\frac{\pi J}{qg_0 H} = \int_{D_s}^{+\infty} \frac{K_1(\sqrt{X^2+H^2})}{\sqrt{X^2+H^2}} dX \quad (\text{A.12})$$

By using asymptotic form $K_1(x) \sim \sqrt{\frac{\pi}{2x}} e^{-x}$ (which is approximately correct if $x > 1$), Eq. A.12 transforms to:

$$\frac{\pi I}{qg_0 H} = \sqrt{\frac{\pi}{2x}} \int_{D_s}^{+\infty} \frac{e^{-\sqrt{X^2+H^2}}}{\sqrt{X^2+H^2}} dX, \quad (\text{A.13})$$

which is approximately correct if $H > 1$ or $h > L_p$. If we apply Watson lemma [3] on Eq. A.13 we obtain:

$$\frac{\pi I}{qg_0 H} = \sqrt{\frac{\pi}{2}} e^{-D_s} D_s^{-3/2}, \quad (\text{A.14})$$

which is correct asymptotic behavior if $D_s > H$, or $d > h$. If we substitute back substitutions A.9, Eq. A.14 becomes:

$$I = \frac{qg_0 h \sqrt{L_p}}{\sqrt{2\pi}} d^{-3/2} e^{-\frac{d}{L_p}}. \quad (\text{A.15})$$

The conditions under which Eq. A.15 is approximately correct are $d > L_p$ and $d > h$.

Bibliography

- [1] D.E. Ioannou and C.A. Dimitriadis, IEEE Trans. Electron Devices **29**, 445 (1982).
- [2] H.K. Kuiken and C. Vanopdorp, J. Appl. Phys. **57**, 2077 (1985).
- [3] G.F.Carrier, M.Krook, and C.E. Pearson, *Functions of a complex variable*, (Hod Books, Ithaca, New York, 1983).

Appendix B Influence of infinite recombination on linear dislocations on minority carrier lifetime

B.1 Hexagonal array of linear dislocations

If we assume that linear dislocations are distributed in a hexagonal "honeycomb-type" array, then the dislocation density can be expressed as $N_{dd} = 1/(\pi r_s^2)$, where $2r_s$ is the distance between two first-neighbor dislocations (see Fig. 4.10a). Dislocations are assumed to have core diameter $2r_0$. The minority carrier concentration (holes, for example) is obtained by solving the two-dimensional diffusion equation for the minority carrier concentration p :

$$D_p \nabla^2 p = \partial p / \partial t. \quad (\text{B.1})$$

Boundary conditions are given by:

$$(i) \quad p|_{r=r_0} = 0 \quad (\text{B.2})$$

$$(ii) \quad \left. \frac{\partial p}{\partial r} \right|_{r=r_s} = 0. \quad (\text{B.3})$$

Boundary condition (i) reflects the fact that due to infinite recombination, the minority carrier concentration at dislocations must be zero. Condition (ii) is approximation to the periodic boundary condition.[1] If we use $p(\vec{r}, t) = p(\vec{r})T(t)$, differential equation B.1 can be separated:

$$\frac{1}{T} \frac{\partial T}{\partial t} = D_p \frac{1}{X} \nabla^2 p = \text{const} = -C, \quad (\text{B.4})$$

from which we obtain:

$$T(t) = T(0)e^{-Ct} \quad (\text{B.5})$$

$$p(\vec{r}) = A_1 J_0\left(\sqrt{\frac{C}{D_p}} r\right) + A_2 N_0\left(\sqrt{\frac{C}{D_p}} r\right), \quad (\text{B.6})$$

where J_0 and N_0 are Bessel and Neumann special functions. The minority carrier lifetime is given by $\tau_{scat} = 1/C$. If boundary conditions (i) and (ii) are applied, one obtains:

$$A_1 J_0\left(\sqrt{\frac{C}{D_p}} r_0\right) + A_2 N_0\left(\sqrt{\frac{C}{D_p}} r_0\right) = 0 \quad (\text{B.7})$$

$$A_1 J'_0\left(\sqrt{\frac{C}{D_p}} r_s\right) + A_2 N'_0\left(\sqrt{\frac{C}{D_p}} r_s\right) = 0 \quad (\text{B.8})$$

where J'_0 and N'_0 are first derivatives of Bessel and Neumann special functions. If we introduce $\omega = \sqrt{\frac{C}{D_p}}$, then the determinant of the set of Eqs. B.7 and B.8 becomes:

$$J_0(\omega r_0)N'_0(\omega r_s) - J'_0(\omega r_s)N_0(\omega r_0) = 0, \quad (\text{B.9})$$

from which follows:

$$\frac{J_0(\omega r_0)}{N_0(\omega r_0)} = \frac{J'_0(\omega r_s)}{N'_0(\omega r_s)} = \frac{J_1(\omega r_s)}{N_1(\omega r_s)}. \quad (\text{B.10})$$

If we assume that $\omega r_0 \sim 1$ and $\omega r_s \sim 1$, we can use asymptotic expansions for Bessel and Neumann's special functions, which reduce Eq. B.10 to:

$$\frac{1}{\frac{2}{\pi} \left[\ln \frac{\omega r_0}{2} + \gamma \right]} = \frac{\frac{\omega r_s}{2}}{-\frac{1}{\pi} \frac{2}{\omega r_s}} = - \left(\frac{\omega r_s}{2} \right)^2 \pi, \quad (\text{B.11})$$

where $\gamma \approx 0.57$ is Euler's constant. After simple algebraic transformation, Eq. B.11 reduces to:

$$\frac{2}{(\omega r_s)^2} = \ln \frac{2}{\omega r_0} - \gamma. \quad (\text{B.12})$$

Since Eq. B.12 is transcendent equation, exact solution is not possible. However, a good guess for iterative procedure is $\omega \approx \frac{1}{r_s}$. We can notice that since the order of

magnitude for r_s is $0.2 \mu\text{m}$ and order of magnitude for r_0 is $0.02 \mu\text{m}=20 \text{ nm}$, then the right side of the Eq. B.12 becomes $\ln 20 - \gamma \approx 2.4$, and the left side is at the same time $2/(1)^2 = 2$. If we use $\omega = \frac{1}{r_s}$ for the second iteration, we obtain:

$$\frac{2}{(\omega r_s)^2} = \ln \frac{2r_s}{r_0} - \gamma, \quad (\text{B.13})$$

or

$$\omega^2 = \frac{2}{r_s^2} \frac{1}{\ln \frac{2r_s}{r_0} - \gamma}. \quad (\text{B.14})$$

The minority carrier lifetime is given by:

$$\tau_{scat} = \frac{1}{C} = \frac{1}{\omega^2 D_p} = \frac{r_s^2}{2D_p} \left[\ln \frac{2r_s}{r_0} - \gamma \right], \quad (\text{B.15})$$

and if we replace $r_s = 1/\sqrt{\pi N_{dd}}$ in Eq. B.15, where N_{dd} is dislocation density, we finally obtain:

$$\tau_{scat} = \frac{1}{2\pi D_p N_{dd}} \left(\ln \frac{2}{r_0 \sqrt{\pi N_{dd}}} - 0.57 \right). \quad (\text{B.16})$$

B.2 Dislocations occupying grain boundaries

From the experimental observations of the linear dislocations patterns, it was observed that in the majority of samples, linear dislocations are distributed at the boundaries of otherwise defect-free grains (as opposed to random distribution). In that case, boundary conditions become:

$$(i) \quad p|_{r=r_s} = 0 \quad (\text{B.17})$$

$$(ii) \quad \frac{\partial p}{\partial r} \Big|_{r=0} = 0. \quad (\text{B.18})$$

This set of boundary conditions reduces to:

$$A_1 J_0'(0) + A_2 N_0'(0) = 0 \quad (\text{B.19})$$

$$A_1 J_0\left(\sqrt{\frac{C}{D_p}} r_s\right) + A_2 N_0\left(\sqrt{\frac{C}{D_p}} r_s\right) = 0. \quad (\text{B.20})$$

This set of boundary conditions will be satisfied if $A_2 = 0$. The solution is then given by zeros of Bessel's function J_0 :

$$\sqrt{\frac{C}{D_p}} r_s = \lambda_0 = 2.4. \quad (\text{B.21})$$

This gives minority carrier lifetime:

$$\tau_p = \frac{r_s^2}{D_p} \frac{1}{2.4^2}. \quad (\text{B.22})$$

Bibliography

- [1] W.R. Harding, I. D. Blenkinsop, and D.R. Wright, *Electron. Lett.* **12**, 502 (1976).

Appendix C Charged linear dislocations: potential and Debye screening length

If we have negatively charged dislocations (see Fig. 4.12) inside the n-type semiconductor, the electrons will feel repulsive Coulomb forces, and space charge region will be formed. This will result in screening of dislocations. The electron distribution will be governed by the potential, and the potential itself depends on charge through Poisson equation. Therefore, the self-consistent solution is required.

The Poisson equation for potential V in cylindrical geometry is given by:

$$\nabla^2 V = \frac{1}{r} \frac{\partial}{\partial r} \left(r \frac{\partial V}{\partial r} \right) = -\frac{\rho(r)}{\epsilon_0 \epsilon_r}, \quad (\text{C.1})$$

where charge ρ at the distance r from the linear dislocation is given by:

$$\rho(r) = gN_d - qn(r), \quad (\text{C.2})$$

where N_d is the concentration of positively charged donor ions, $n(r)$ is electron concentration, and q is unit electron charge. If we assume that (i) electron-electron interaction is negligible compared to thermal energy kT , then the electron concentration is function of the potential and is determined by Boltzmann's distribution:

$$n(r) = N_d e^{-\frac{(-q)V}{kT}} \quad (\text{C.3})$$

Equations C.1 and C.3 have to be solved self-consistently. If we replace Eq. C.3 in Eq. C.2, and then in Eq. C.1, we obtain:

$$\frac{1}{r} \frac{\partial}{\partial r} \left(r \frac{\partial V}{\partial r} \right) = -\frac{qN_d}{\epsilon_0 \epsilon_r} \left[1 - e^{\frac{qV}{kT}} \right] \quad (\text{C.4})$$

If we assume that (ii) potential V is small compared to kT , then we can expand $e^{\frac{qV}{kT}} \approx 1 + \frac{qV}{kT}$, and Eq. C.4 becomes:

$$\frac{1}{r} \frac{\partial}{\partial r} \left(r \frac{\partial V}{\partial r} \right) = \frac{q^2 N_d}{\epsilon_0 \epsilon_r kT} V. \quad (\text{C.5})$$

If we introduce $\kappa^2 = \frac{q^2 N_d}{\epsilon_0 \epsilon_r kT}$, the Eq. C.5 becomes:

$$\frac{1}{r} \frac{\partial}{\partial r} \left(r \frac{\partial V}{\partial r} \right) = \kappa^2 V. \quad (\text{C.6})$$

The Eq. C.6 can be written as:

$$\frac{\partial^2 V}{\partial r^2} + \frac{1}{r} \frac{\partial V}{\partial r} - \kappa^2 V = 0. \quad (\text{C.7})$$

The solution of Eq. C.7 is given as modified Bessel function:

$$V(r) = CK_0(\kappa r) \quad (\text{C.8})$$

Constant C in Eq. C.8 can be determined from boundary conditions around dislocation. If dislocation has linear charge density $-q'$, $q' > 0$, the electric field of the dislocation very close to dislocation is given by $E = -\frac{q'}{2\pi\epsilon_0\epsilon_r r}$. If we use boundary condition:

$$E|_{r \rightarrow 0} = -\frac{\partial V}{\partial r} \Big|_{r \rightarrow 0}, \quad (\text{C.9})$$

and if we use asymptotic expansion for modified Bessel function $K_0(x) \sim -[\ln(x/2) + \gamma]$, where $\gamma \approx 0.57$ is Euler's constant, we obtain:

$$-\frac{q'}{2\pi\epsilon_0\epsilon_r r} \Big|_{r \rightarrow 0} = -\frac{\partial}{\partial r} \left[\ln\left(\frac{\kappa r}{2} + \gamma\right) \right] \Big|_{r \rightarrow 0} = -(-C) \left[\frac{1}{r} \right] \Big|_{r \rightarrow 0}, \quad (\text{C.10})$$

which finally gives:

$$C = -\frac{q'}{2\pi\epsilon_0\epsilon_r}. \quad (\text{C.11})$$

Finally, the potential around dislocations is:

$$V(r) = -\frac{q'}{2\pi\epsilon_0\epsilon_r} K_0\left(\frac{r}{\lambda_D}\right), \quad (\text{C.12})$$

where $\lambda_D = 1/\kappa$ is Debye's screening length:

$$\lambda_D = \sqrt{\frac{\epsilon_0\epsilon_r kT}{q^2 N_d}}. \quad (\text{C.13})$$

It is important to discuss under what conditions is Eq. C.12 approximately correct. Condition (i) discussed above is equivalent to

$$\frac{1}{4\pi\epsilon_0\epsilon_r} \frac{q^2}{r_a} \ll kT \quad (\text{C.14})$$

where r_a is average distance between electrons and is given by $r_a \approx n^{-1/3}$. From Eq. C.14 we obtain:

$$n \ll \left(\frac{4\pi\epsilon_0\epsilon_r kT}{q^2}\right)^3 \approx 10^{18} \text{ cm}^{-3} \quad (\text{C.15})$$

The condition (ii) is approximately equivalent to:

$$q \frac{q'}{2\pi\epsilon_0\epsilon_r kT} \ll 1, \quad (\text{C.16})$$

which gives:

$$q' \ll 1.4 \cdot 10^{-11} \text{ C/m} \quad (\text{C.17})$$

which approximately corresponds to one unit electron charge per 10 nm.